The Role of Defects on the Optical, Electronic, and Magnetic Properties of Iron-Sulfur Solids

by

Alyssa Ruth Landin

B.A., Luther College, 2013

A thesis submitted to the

Faculty of the Graduate School of the

University of Colorado in partial fulfillment

of the requirements for the degree of

Doctor of Philosophy

Department of Chemistry

2018

ProQuest Number: 10928421

ProQuest 10928421

Published by ProQuest LLC (2018). Copyright of the Dissertation is held by the Author.

ProQuest LLC.
789 East Eisenhower Parkway
P.O. Box 1346
Ann Arbor, MI 48106 – 1346

This thesis entitled:
The Role of Defects on the Optical, Electronic, and Magnetic Properties of Iron-Sulfur Solids
written by Alyssa Ruth Landin
has been approved for the Department of Chemistry

_____

Joel D. Eaves

_____

Sandeep Sharma

Date _____

The final copy of this thesis has been examined by the signatories, and we find that both the
content and the form meet acceptable presentation standards of scholarly work in the above
mentioned discipline.

Landin, Alyssa Ruth (Ph.D., Chemical Physics)

The Role of Defects on the Optical, Electronic, and Magnetic Properties of Iron-Sulfur Solids

Thesis directed by Joel D. Eaves

Solids composed of iron and sulfur are earth abundant and nontoxic, and can exhibit interesting and technologically important optical, electronic, and magnetic phenomena. Troilite (hexagonal FeS) is predicted to exhibit large room temperature magnetoelectricity and may exhibit high temperature superconducting properties, and pyrite (cubic FeS_2) is a promising candidate for photovoltaic applications. However, defects naturally occur within both of these solids. Troilite contains Fe deficiencies with atomic formula $Fe_{1-x}S$, while pyrite contains sulfur deficiencies with the atomic formula FeS_{2-x}. The Fe-S phase diagram is congested in these regions of slight non-stoichiometries, and even when the atomic composition changes by just a few percent at standard temperature and pressure, there are a myriad of stable crystal phases that form with qualitatively different electronic properties. This dissertation describes the computational efforts to understand and characterize the nature of defects within these two materials.

The first part of this thesis looks at the effects of iron vacancies in Fe-S solids using the stoichiometric end-member, troilite, as a reference system. Density functional theory (DFT) calculations show that iron vacancies in troilite shift the structure from hexagonal FeS to a monoclinic structure, similar to crystal structures of pyrrhotites, and suggest that this iron deficient troilite may be a stable intermediate between these crystal structures. The calculations also predict that the defects close the band gap of the slightly insulating material.

The second part of this thesis focuses on sulfur defects in pyrite. DFT calculations predict a narrowing of the band gap of the semiconductor and reveal strong electron-nuclear coupling in the material due to the extreme sensitivity of the energies of the spatially localized defect states to the nuclear coordinates. The defect states of sulfur deficient pyrite are further characterized by transforming the delocalized Bloch states obtained with DFT into maximally localized Wannier

functions. In this now diabatic representation, the crystal field splitting of pyrite decreases by a factor of two in the presence of the defect. The degeneracies of the Fe d-orbitals orbitals lift with a sulfur defect, which may cause a spin crossover and an emergent magnetic state.

Acknowledgements

Contents

Tables

Table

Figures

Figure

Chapter 1

Introduction

1.1   Iron-Sulfur Solids

Iron sulfides constitute a diverse group of solids that are a significant part of many natural processes and exhibit a myriad of physical properties that enable novel technological applications. Fe-S solids play important roles in the biogeochemical sulfur and iron cycles on Earth and are key indicators of contemporary environmental changes, so are central to our understanding of the development of the Earth [1, 2]. Also found in many meteorites, iron sulfides may exist in the cores of other terrestrial planets, including Mars, and provide information about planetary systems [3]. Some Fe-S solids can reduce heavy metals and are used in the treatment of contaminated groundwater and soil [1, 4, 5]. These solids have also been shown to perform catalytic activity in prebiotic conditions. They can act as a catalyst for the synthesis of pyruvic acid and are hypothesized to be critical for the origin of life and prebiotic chemistry [6, 7]. The d-electrons on the iron atoms can endow these materials with strongly-correlated electronic properties, including large room temperature magnetoelectricity, unconventional high temperature superconductivity, and semiconducting behavior with possible applications in photovoltaics and electronics [8, 9, 10, 11, 12, 13].

At least seven different solids consisting of only iron and sulfur are known to occur naturally at ambient pressure and temperature [1]. These include mackinawite (tetragonal FeS), cubic FeS, troilite (hexagonal FeS), pyrrhotite ($Fe_{1-x}S$ with various unit cells), greigite (cubic Fe_3S_4), pyrite (cubic FeS_2), and marcasite (orthorhombic FeS_2). The facile nature of the oxidation states and

bonding patterns in both sulfur and iron makes these materials difficult to synthesize, characterize, and model computationally relative to other strongly correlated iron-based materials [14, 1, 15, 16, 17]. The phase diagram of these materials, where it has been measured, exhibits a large diversity of polymorphs and polytypes that are separated by only tens of Kelvin and single percentages of mole fraction [18, 19, 20, 21, 22]. The complexity of this phase diagram, shown in Figure 1.1, has similarities to other kinetically frustrated and disordered systems containing several stable configurations such as glasses, proteins, and colloids [23]. Slight changes to the Fe:S composition ratio lead to large variations in structural, chemical, optoelectronic, and other physical properties [10, 14, 22, 24]. Defects in these materials, even at concentrations of a single percent, have marked effects on their properties in poorly understood ways [25, 26, 27]. These complexities have plagued a comprehensive structural and chemical characterization of many iron-sulfur solids, mainly near stoichiometric FeS and FeS_2. The principal goal of this thesis is to explore, using microscopically detailed simulations and theory, how and why vacancy defects have such a strong influence on the physical properties of iron sulfur solids.
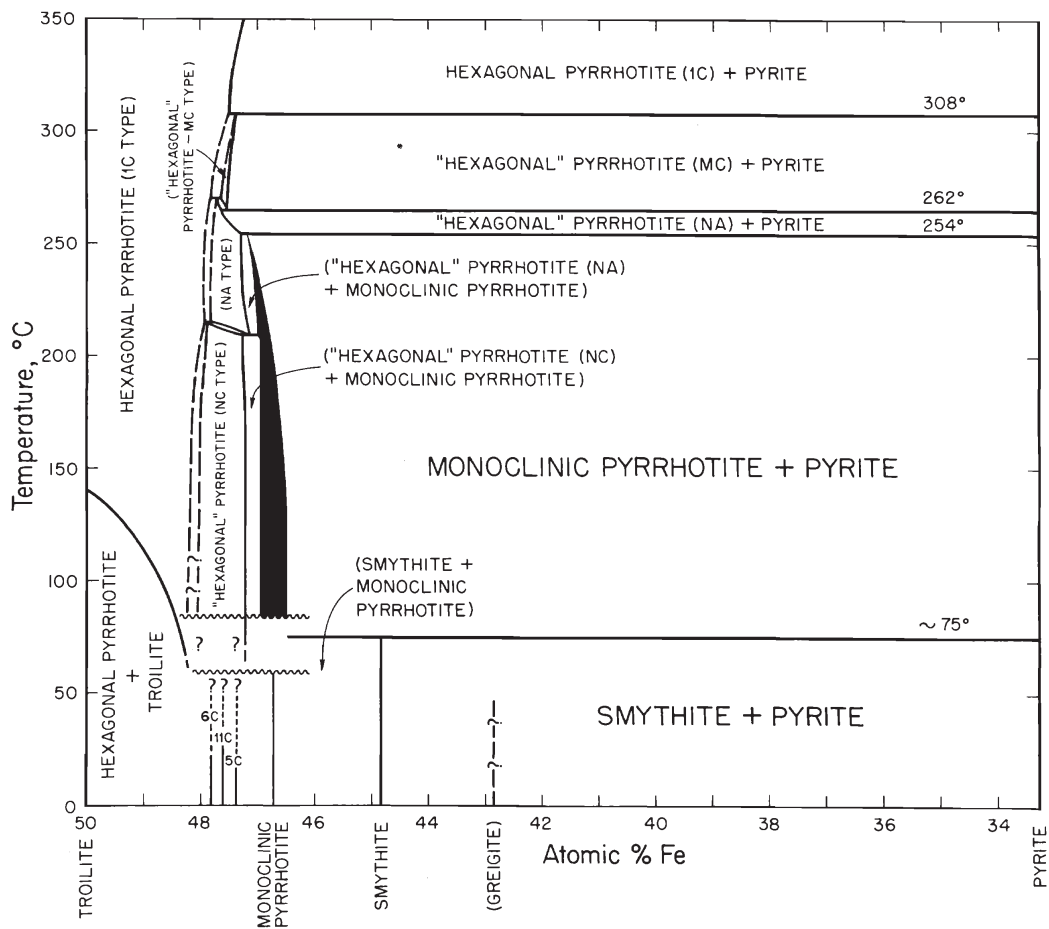
Do I put something in here about the experimental collaborators??

We will focus our studies on two systems: Fe vacancies in the pyrrhotite family ($Fe_{1-x}S$) and S vacancies in the pyrite structure (FeS_{2-x}).

1.1.1 Troilite (FeS) and the Pyrrhotites ($Fe_{1-x}S$)
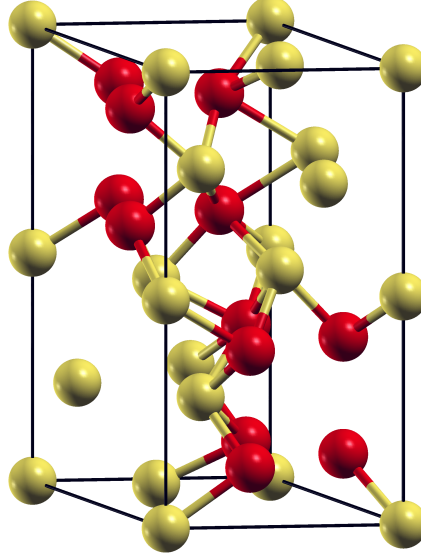
At ambient pressure and temperature and in an anhydrous environment, stoichiometric FeS takes the form of troilite, an octahedrally coordinated distorted NiAs-based crystal in the hexagonal *P-62c* space group. Shown in Figure 1.2, the troilite unit cell contains 12 formula units of FeS. Each Fe is octahedrally coordinated to six sulfurs and each S is tetrahedrally coordinated to four irons. Ricci and Bousquet predict that troilite should have a large room-temperature magnetoelectric effect, while Gunon *et al.* have explored troilite as a candidate for a non-tetragonal high temperature iron based superconductor [9, 28]. In situ, troilite samples are exclusively found in meteorites as a minority phase, and are thus seldom without impurities and defects. As a result,

Figure 1.1: The summary phase diagram for the FeS-FeS$_2$ segment of the Fe-S system below 350°C from Kissin et al. [18]. Dashed phase boundaries are inferred, and those with question marks are hypothetical. Much of the Fe-rich pyrrhotite region is inferred and many structures are stable at the same stoichiometries and temperatures.

experimental work with natural samples cannot guarantee that results are free of compositional artifacts. Additionally, both synthetic and natural samples of the composition of FeS, measured at sufficiently high resolution, report that troilite contains iron vacancies [29, 30, 31].
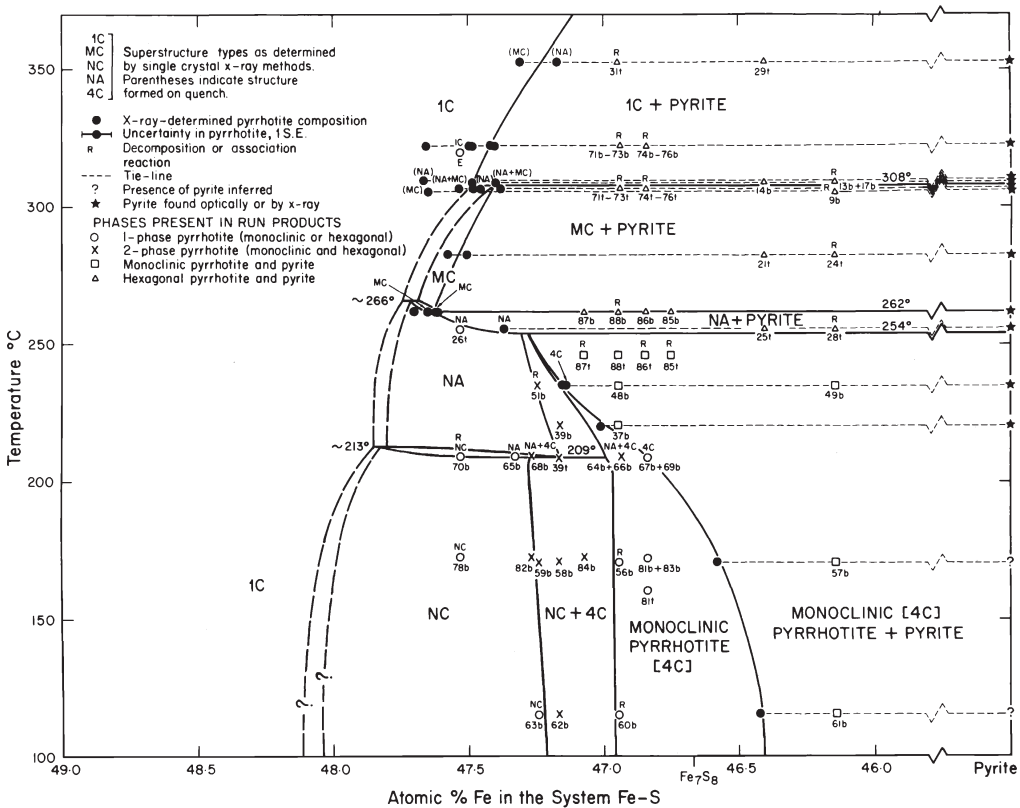
Figure 1.2: Hexagonal unit cell of troilite where Fe and S are labeled red and yellow, respectively.

Pyrrhotites are an entire class of Fe-S structures possessing a NiAs-based structure, normally with slightly iron deficient compositions ($Fe_{1-x}S$) that contain a host of variations in stoichiometry and unit cell geometry [32]. Reported instances of natural and synthetic $Fe_{1-x}S$ systems see iron deficiencies anywhere from $0.004 \leq x \leq 0.143$ [22, 33]. Those pyrrhotites that are stable in nature tend to have a stoichiometry of $Fe_{x-1}S_x$ where $x \geq 8$ [34]. Figure 1.3 shows the zoomed in version of the FeS-FeS$_2$phase diagram (Figure 1.1). This region of the phase diagram belonging to the pyrrhotites is ill defined, not only in the scope of the structures it encompasses, but also in the transformational pathways between the different crystal structures.

The naming convention for pyrrhotites is generally presented as a number correlating to repeated layers and a letter which represents the axis along which the repetition occurs. For example, "4C" and "5C" refer to the structures that have a c-axis of 4*c and 5*c of the base NiAs unit cell, respectively. This family of materials primarily takes on monoclinic, hexagonal, and

Figure 1.3: Phase diagram for the intermediate pyrrhotite compositional range of the Fe-S system from Kissin et al. [18]. Dashed lines and question marks correspond to inferred and hypothetical phase transitions, respectively.

orthorhombic structures, and can be distinguished further by using "M" or "H" instead of "C" to denote monoclinic or hexagonal structures, respectively. Magnetic and electronic properties also differ with these slight structural variations. The pyrrhotite family technically includes troilite as pyrrhotite-2C, and reported compositions of troilite are nonstoichiometric and comparable to other pyrrhotites even though troilite technically denotes a stoichiometric FeS structure [35]. Table 1.1 lists the unit cell parameters of common Fe-deficient pyrrhotites. Even with the same composition, we see a variety of crystal structures, illuminating the numerous polytypes of pyrrhotite and the complicated nature of the Fe-S phase diagram.

1.1.2   Pyrite (FeS_2)

Pyrite is the most abundant metal sulfide on the Earth's surface [41]. In addition to its essentially infinite abundance and nontoxic nature, pyrite is a promising semiconductor for use in photovoltaics and photochemical cells due to its suitable band gap of roughly 0.95 eV, high absorptivity in the solar emission spectrum, and low cost to produce [42]. However, pyrite exhibits a low conversion efficiency of $\sim$3%, primarily due to its unexpectedly low open circuit voltage (V_{OC}) of under 200 meV [43, 44]. Surface and bulk defects have been often identified as the ultimate source of the low V_{OC}, though because it is very difficult to entirely eliminate defects, it is not clear whether or not the relationship between vacancies and V_{OC} is a causal one [45, 46, 42].

Crystalline pyrite is part of the cubic *Pa3* space group where each Fe is coordinated octahedrally to six sulfurs. In terms of formal charges, each S exists as a S_2^{2-} dimer and sits in a distorted tetrahedral coordination surrounded by three irons and the sulfur that it exists with as a dimer. The conventional unit cell of pyrite, shown in Figure 1.4, is based on the rock-salt structure of NaCl and contains 4 formula units of FeS_2. The four iron atoms in the unit cell reside at the Na sites, forming a face centered cubic (fcc) sub-lattice, and the center of mass of each of the four S_2^{2-} dimers is located at the Cl sites and oriented in the <111> direction [25, 47, 48]. Even though the calculated defect formation energy for a sulfur vacancy in the S-poor/Fe-rich region is quite large (2.2-2.4 eV) [49, 27, 26, 50, 51], experimental measurements, including high resolution X-ray
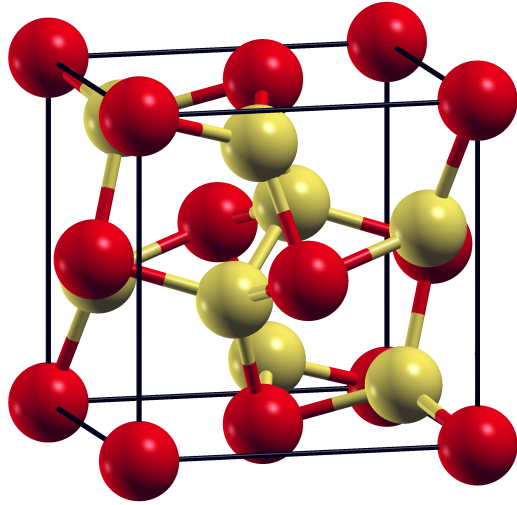
Table 1.1: Unit cell parameters of known pyrrhotites with stoichiometries ranging from Fe_7S_8 to $Fe_{10}S_{11}$. "M" , "H" , and "C" denote monoclinic, hexagonal, and orthorhomic unit cells, respectively.

Type	Composition	Space Group	Cell Dimensions				
			a (Å)	b (Å)	c (Å)	β (°)	Ref.
4M	Fe_7S_8	$F2/d$	6.860	11.903	22.788	90.5	[34]
4M	Fe_7S_8	$F2/d$	6.872	11.903	22.780	90.4	[36]
4M	Fe_7S_8	$F2/d$	6.859	11.902	22.787	90.26	[37]
4M	Fe_7S_8	$C2/c$	11.897	6.8586	12.891	118.036	[15]*
5H	Fe_9S_{10}	–	6.88	–	28.70	–	[34]
5H	Fe_9S_{10}	–	6.881	–	28.68	–	[36]
5M	Fe_9S_{10}	$P2_1$	6.8984	28.695	6.8915	119.956	[38]
5C	Fe_9S_{10}	$Cmca$	6.8933	11.9393	28.6351	–	[39]
6M	$Fe_{11}S_{12}$	Fd	6.8973	11.954	34.521	90.003	[40]
6H	$Fe_{11}S_{12}$	–	6.90	–	34.56	–	[34]
6H	$Fe_{11}S_{12}$	–	6.904	–	34.51	–	[36]
11C	$Fe_{10}S_{11}$	$Cmca$	6.892	11.952	63.184	–	[34]

*Matches the experimental structure obtained from our collaborators

diffraction (HRXRD), photoemission of adsorbed Xe (PAX), and atomic emission spectroscopy (AES), confirm that sulfur vacancies, up to 6% atomic deficiency, exist in both naturally occurring and synthetic pyrite samples [25, 52, 53, 54].

Figure 1.4: Pyrite unit cell where Fe and S are labeled red and yellow, respectively.

1.1.3   Computational Challenges for Fe-S Systems

For the Fe-S systems studied here, there are two major computational challenges. First, the unit cells, particularly for defective structures, contain many electrons and adopt a priori unknown crystal structures that have low symmetry space groups. Defect concentrations are on the order of or lower than 10%, so we are sometimes required to look at a supercell with many more atoms, which increases the computational cost. Second, FeS compounds exhibit strong electron correlation due to the presence of iron. These challenges require a computational method that can reasonably capture the effects of strong electron correlation, and is also computationally feasible for large periodic systems. Density Functional Theory (DFT) is the standard and most popular computational method used today for condensed matter systems since it can feasibly calculate the properties for systems with periodic boundary conditions and up to a couple hundred atoms.

Although DFT is by definition a ground state theory, it can predict band gaps and optical properties that do agree with experiment for Fe-S solids and is not computationally intractable like the more accurate GW and CI theories for these materials.

1.2   Organization of the Thesis

The outline of this dissertation is as follows: In Chapter 2, we cover the theoretical basis of the methods used in this dissertation. We present the fundamental theorems of DFT and include definitions and explanations of the exchange-correlation potential, pseudo-potentials, the projector augmented-wave method, and plane wave basis sets used within DFT. We also describe the theoretical background of Wannier90, a program that transforms the delocalized Bloch states obtained through DFT into localized Wannier functions to get the diabatic representation of a system. We use the localized Wannier orbitals, in concert with crystal field theory, as an interpretative tool.

Chapter 3 looks at the effects of an Fe vacancy in troilite and how it compares to the pyrrhotite family. By comparing the electronic structure of troilite with a Fe vacancy to defect-free troilite and pyrrhotite-4M, we find that the presence of a Fe vacancy distorts the troilite unit cell into the resemblance of a pyrrhotite and closes the band gap exhibited in defect-free troilite. We also calculate and assign the phonon modes of troilite, as these have not been computed before, and can be measured using Raman or terahertz spectroscopy.

In Chapter 4, we characterize bulk sulfur defects in pyrite in both the adiabatic and diabatic representations. In the adiabatic representation, the S vacancy creates four localized defect states that decrease the band gap of the material and strongly depend on the nuclear coordinates. To get a clear picture of the effect the S vacancy in pyrite has on the crystal field splitting, we transform our adiabatic states into diabatic atomic orbitals and observe that although the crystal field splitting decreases, only the localized orbitals surrounding the defect contribute to the decreased splitting. We then provide a hypothesis for the experimentally observed emergence of magnetism in the solid with a probable spin crossover and spin splitting due to the presence of the defect.

Chapter 2

Computational Methods

The majority of my dissertation work utilizes Density Functional Theory (DFT) within the Vienna Ab initio Simulation Package (VASP) [55, 56, 57, 58]. In order to provide a complete procedure for my work, I will briefly present the theoretical basis of DFT in this chapter, including any additional considerations used while running VASP. The last section of this chapter describes the theoretical background of Wannier90 [59], the other major software program used in my dissertation work that transforms the delocalized DFT Bloch states into maximally-localized Wannier functions (MLWFs).

2.1   Density Functional Theory

The Hamiltonian for a system of N interacting electrons under the Born Oppenheimer approximation in an external potential is given by (in atomic units where $\hbar = m_e = e = 4\pi\epsilon_0 = 1$):

$$H = \sum_{i=1}^{N} \left[\frac{-\nabla_i^2}{2} + V_{ext}(\mathbf{r}) \right] + \sum_{i>j} \frac{1}{|\mathbf{r}_i - \mathbf{r}_j|} \tag{2.1}$$

where the first term is the kinetic energy of the electron, the second term is the interaction with the external potential which can include an externally applied electric or magnetic field, and the third term is the Coulomb interaction of the electron with all other electrons. Since my work deals exclusively with periodic solids, the external potential is given by the interaction between the electrons and nuclei. For M nuclei in the system, the Hamiltonian becomes:

$$H = \sum_{i=1}^{N} \left[\frac{-\nabla_i^2}{2} + \sum_j^M \frac{Z_j}{|\mathbf{r}_i - \mathbf{R}_j|} \right] + \sum_{i>j} \frac{1}{|\mathbf{r}_i - \mathbf{r}_j|} \tag{2.2}$$

where Z_j is the atomic number and $\mathbf{R}_j$ is the position of the nucleus. We can solve the system with the time-independent Schrödinger equation $H|\Psi\rangle = E|\Psi\rangle$, where each state of the system $|\Psi\rangle$ is composed of N electronic wavefunctions $|\phi_i\rangle$. For the systems I'm interested in, this method becomes computationally intractable.

DFT is an alternative method to the electronic structure problem that does not rely on the solution to the time-independent Schrödinger equation. Indeed, DFT is not a wavefunction method, but is instead based on electron density $n(\mathbf{r})$, where $n(\mathbf{r}) = \sum_{i=1}^{N} \delta(\mathbf{r} - \mathbf{r}_i)$. This principal object of DFT has just three coordinates, whereas the wavefunction of the system contains $3N$ coordinates. Similar to Hartree Fock methods, it will also turn out that DFT can be made to scale as a low-order polynomial in the number of electrons, though DFT contains electron correlation that Hartree Fock does not. The foundation of DFT lies in the Kato and Hohemburg-Kohn (HK) theorems [60, 61], which prove that there exists a unique electron density for a particular system, which is sufficient to determine all the physical properties of the system. The Kato theorem states for generalized Coulomb potentials, the electron density has cusps at the positions of each nuclei which satisfies:

$$Z_k = -\frac{a_o}{2n(\mathbf{r})} \frac{dn(\mathbf{r})}{dr} |_{r \to \mathbf{R}_k} \tag{2.3}$$

where $\mathbf{R}_k$ denotes the positions of the nuclei with corresponding atomic numbers Z_k, and a_o is the Bohr radius. The nuclei are located at the cusps of the electron density with the charge obtained from equation 2.3. We can then integrate the electron density over all space, giving the total number of electrons in the system. Knowing the positions and charges of each nuclei along with the total number of electrons and electron density, we have all the information necessary for completely specifying the Hamiltonian. From this, we see that we only need the electron density to satisfactorily define an entire system.

The HK theorems are as follows:

(1) For non-degenerate ground states, two different Hamiltonians (systems) cannot have the

same ground state electron density. Therefore, it is possible to define the ground state energy as a functional of the electron density $n(\mathbf{r})$: $E = E[n(\mathbf{r})]$.

(2) $E[n(\mathbf{r})]$ is at a minimum when $n(\mathbf{r})$ is the actual ground state density, out of all possible electron densities.

The proof of the first HK theorem is a proof by contradiction, in which we use the relationship between the electron density and many-body wavefunction $n(\mathbf{r}) = \sum_{i=1}^{N} \int d\mathbf{r}_1...d\mathbf{r}_N \delta(\mathbf{r} - \mathbf{r}_i) |\Psi(\mathbf{r}_1, ..., \mathbf{r}_N)|^2$:

Assume that there exist two different external potentials $V_{ext}^{(1)}$ and $V_{ext}^{(2)}$ which both have the same electron density $n(\mathbf{r})$. The two external potentials, by definition, give rise to two different Hamiltonians $H^{(1)}$ and $H^{(2)}$, with different ground state wavefunctions $\Psi^{(1)}$ and $\Psi^{(2)}$, respectively. Based on the variational principle, any wavefunction that is not the ground state for a particular Hamiltonian will have an energy higher than the ground state energy for that system:

$$E_0^{(1)} < \langle \Psi^{(2)} \mid H^{(1)} \mid \Psi^{(2)} \rangle \tag{2.4}$$

$$E_0^{(2)} < \langle \Psi^{(1)} \mid H^{(2)} \mid \Psi^{(1)} \rangle \tag{2.5}$$

Since the different external potentials have the same electron density and the only difference in the Hamiltonians is the external potential, we have:

$$E_0^{(1)} < \langle \Psi^{(2)} \mid H^{(1)} \mid \Psi^{(2)} \rangle = \langle \Psi^{(2)} \mid H^{(2)} \mid \Psi^{(2)} \rangle + \langle \Psi^{(2)} \mid H^{(1)} - H^{(2)} \mid \Psi^{(2)} \rangle = E_0^{(2)} + \int d\mathbf{r}[V_{ext}^{(1)} - V_{ext}^{(2)}]n(\mathbf{r})$$

$$\tag{2.6}$$

$$E_0^{(2)} < \langle \Psi^{(1)} \mid H^{(2)} \mid \Psi^{(1)} \rangle = \langle \Psi^{(1)} \mid H^{(1)} \mid \Psi^{(1)} \rangle + \langle \Psi^{(1)} \mid H^{(2)} - H^{(1)} \mid \Psi^{(1)} \rangle = E_0^{(1)} + \int d\mathbf{r}[V_{ext}^{(2)} - V_{ext}^{(1)}]n(\mathbf{r})$$

$$\tag{2.7}$$

When we add the two previous equations, the integrals cancel because they have the same electron density and we get the following contradiction:

$$E_0^{(1)} + E_0^{(2)} < E_0^{(2)} + E_0^{(1)} \tag{2.8}$$

The proof of the second HK theorem is an extension of the variational theorem from wavefunctions to electron densities:

After fixing the potential that determines the ground state Ψ_0 of a system, we can choose any electron density that satisfies $\int d\mathbf{r} n(\mathbf{r}) = N$, where N is the total number of electrons in the system. For any particular density $\tilde{n}$, we have the corresponding many-electron wavefunction $\tilde{\Psi}$ since the first HK theorem states that two different wavefunctions cannot yield the same ground state density. Because $\tilde{\Psi} \neq \Psi_0$, $E[\tilde{n}] = \langle \tilde{\Psi} \mid H \mid \tilde{\Psi} \rangle > \langle \Psi_0 \mid H \mid \Psi_0 \rangle = E[n_0]$.

Based on the above theorems, once we minimize the energy, we obtain the unique ground state electron density, which provides us with many physical properties of the system in its ground state.

If we rewrite Equation 2.2 in terms of the electron density, we obtain the total energy functional for our system, which consists of the kinetic energy functional $T[n(\mathbf{r})]$, the external energy functional $E_{ext}[n(\mathbf{r})]$, and the Coulomb functional $U[n(\mathbf{r})]$:

$$E[n(\mathbf{r})] = T[n(\mathbf{r})] + E_{ext}[n(\mathbf{r})] + U[n(\mathbf{r})] \tag{2.9}$$

The usefulness of the total energy functional arises from the universality of the kinetic and Coulomb functionals. These functionals remain the same no matter what system we calculate. The only non-universal piece is $E_{ext}[n(\mathbf{r})]$ since it is system specific. If we change the identities of the nuclei, for example, the Z_j in Equation 2.2 will also change and result in a different $E_{ext}[n(\mathbf{r})]$. However, we know exactly how $E_{ext}[n(\mathbf{r})]$ depends on $n(\mathbf{r})$:

$$E_{ext}[n(\mathbf{r})] = \int d\mathbf{r} V_{ext}(\mathbf{r}) n(\mathbf{r}) \tag{2.10}$$

For the periodic solids studied in this thesis, the external energy functional becomes:

$$E_{ext}[n(\mathbf{r})] = \int d\mathbf{r} \sum_{i=1}^{M} \frac{Z_i}{|\mathbf{r} - \mathbf{R}_i|} n(\mathbf{r}) \tag{2.11}$$

We can parameterize $E[n(\mathbf{r})]$ into exactly solvable terms arising from the independent particle system and everything else we don't know. This has the form:

$$E[n(\mathbf{r})] = T_s[n(\mathbf{r})] + \frac{1}{2} \int d\mathbf{r} \int d\mathbf{r}' \frac{n(\mathbf{r})n(\mathbf{r}')}{|\mathbf{r} - \mathbf{r}'|} + \int d\mathbf{r} \sum_{i=1}^{M} \frac{Z_i}{|\mathbf{r} - \mathbf{R}_i|} n(\mathbf{r}) + E_{xc}[n(\mathbf{r})] \tag{2.12}$$

where the first term $T_s[n(\mathbf{r})]$ is the independent-particle kinetic energy functional (where s stands for "single particle" and refers to the noninteracting system) with the form:

$$T_s[n(\mathbf{r})] = -\frac{1}{2} \sum_{i=1}^{N} \int d\mathbf{r} \psi_i^*(\mathbf{r}) \nabla^2 \psi_i(\mathbf{r}) \tag{2.13}$$

The second term is the classic Coulomb electrostatic interaction between independent electrons and denoted the Hartree term $E_H[n(\mathbf{r})]$, the third term is the external energy functional defined in Equation 2.11, and $E_{xc}[n(\mathbf{r})]$ is the exchange-correlation functional that includes the interacting components of the kinetic and Coulombic functionals. $E_{XC}[n(\mathbf{r})]$ should account for all the quantum effects of the system including the Pauli repulsion of electron with the same spin, the correction of the the self-interaction term in $E_H[n(\mathbf{r})]$, and electron correlation effects. For simplicity, we will refer to the second term of Equation 2.12 as $E_H[n(\mathbf{r})]$ and the external energy potential as $V_{ext}(\mathbf{r})$ in the rest of this derivation. The energy functional now has the form:

$$E[n(\mathbf{r})] = T_s[n(\mathbf{r})] + E_H[n(\mathbf{r})] + \int d\mathbf{r} V_{ext}(\mathbf{r})n(\mathbf{r}) + E_{xc}[n(\mathbf{r})] \tag{2.14}$$

2.1.1 Kohn-Sham equations

The Kohn-Sham ansatz makes DFT practical and inexpensive to use because it maps the original fully interacting system with a real potential onto a virtual noninteracting system and assumes the two systems have the same ground state electron density [62]. With this mapping, we

only need single-particle wavefunctions instead of the fully interacting multi-electron wavefunctions for our calculations. The energy functional of the noninteracting system with the same ground state electron density as $E[n(\mathbf{r})]$ will contain the independent-particle kinetic energy $T_s[n(\mathbf{r})]$ defined previously and some effective external potential $V_s(\mathbf{r})$. Denoted $E_s[n(\mathbf{r})]$, the energy functional of the noninteracting system writes:

$$E_s[n(\mathbf{r})] = T_s[n(\mathbf{r})] + \int d\mathbf{r} V_s(\mathbf{r})n(\mathbf{r}) \tag{2.15}$$

The first HK theorem states that two different Hamiltonians cannot have the same ground state electron density, so the interacting system given by $E[n(\mathbf{r})]$ and the noninteracting system given by $E_s[n(\mathbf{r})]$ must be equal and have the same properties: $E[n(\mathbf{r})] = E_s[n(\mathbf{r})]$. The current form of the effective external potential $V_s(\mathbf{r})$ is unknown, but we can compare it with the interacting system to determine its form. In order to directly compare the effective potential, we need to use the variational form of the energy functionals since $V_s(\mathbf{r})$ is integrated in $E_s[n(\mathbf{r})]$. $E[n(\mathbf{r})] = E_s[n(\mathbf{r})]$ implies that the functional derivatives are also equal:

$$\frac{\delta E[n(\mathbf{r})]}{\delta n(\mathbf{r})} = \frac{\delta E_s[n(\mathbf{r})]}{\delta n(\mathbf{r})} \tag{2.16}$$

$$\frac{\delta T_s[n(\mathbf{r})]}{\delta n(\mathbf{r})} + V_{ext}(\mathbf{r}) + e^2 \int \frac{n(\mathbf{r}')}{|\mathbf{r}-\mathbf{r}'|}d\mathbf{r}' + \frac{\delta E_{xc}[n(\mathbf{r})]}{\delta n(\mathbf{r})} = \frac{\delta T_s[n(\mathbf{r})]}{\delta n(\mathbf{r})} + V_s(\mathbf{r}) \tag{2.17}$$

From the previous equation, we see that:

$$V_s(\mathbf{r}) = V_{ext}(\mathbf{r}) + e^2 \int \frac{n(\mathbf{r}')}{|\mathbf{r}-\mathbf{r}'|}d\mathbf{r}' + V_{xc}(\mathbf{r}; [n(\mathbf{r})]) \tag{2.18}$$

where $V_{xc}(\mathbf{r}; [n(\mathbf{r})]) = \delta E_{xc}[n(\mathbf{r})]/\delta n(\mathbf{r})$ is the functional derivative of the exchange-correlation energy, normally referred to as the exchange-correlation potential. This noninteracting system has an electron density given by:

$$n_s(\mathbf{r}) = \sum_j f_j |\psi_j(\mathbf{r})|^2 \tag{2.19}$$

where $\psi_j(\mathbf{r})$ are the one-particle non interacting orbitals with occupation factor f_j. Since this system has the same ground state electron density as the interacting system, $n_s(\mathbf{r}) = n(\mathbf{r})$. We can

solve this noninteracting system using the Schrödinger equation, which gives rise to the well-known Kohn-Sham (KS) equations:

$$\left[\frac{-\nabla^2}{2} + V_{ext}(\mathbf{r}) + \int \frac{n(\mathbf{r}')}{|\mathbf{r} - \mathbf{r}'|} d\mathbf{r} + V_{xc}(\mathbf{r}; [n(\mathbf{r})])\right] \psi_j(\mathbf{r}) = \epsilon_j \psi_j(\mathbf{r}) \tag{2.20}$$

$$n(\mathbf{r}) = \sum_j f_j |\psi_j(\mathbf{r})|^2 \tag{2.21}$$

Since both the kinetic energy integral and the exchange-correlation potential depend on $n(\mathbf{r})$, the KS equations are coupled nonlinear integrodifferential equations. They are normally solved self-consistently starting with a trial $n(\mathbf{r})$ and iterating to achieve convergence. It is important to note that $\psi_j(\mathbf{r})$ are the KS orbitals of a virtual non interacting system. The corresponding KS eigenvalues ϵ_j do not represent the eigen-energies of the physical interacting electron system except for the highest occupied ϵ_j, which represents the first ionization energy and is merely an extension of Koopman's Theorem [63].

2.1.2 Spin-Polarized Case

In systems with d-orbitals, like iron, one can have magnetic states that involve unpaired electrons. We therefore need to specify the number of spin-up and spin-down electrons. A set of Kohn-Sham equations are solved for both spin components, leading to two sets of KS orbitals depending on the z-component of the electron spin χ, where $\chi = \uparrow$ or $\chi = \downarrow$:

$$\left[\frac{-\nabla^2}{2} + V_{ext}(\mathbf{r}) + \int \frac{n(\mathbf{r}')}{|\mathbf{r} - \mathbf{r}'|} d\mathbf{r} + V_{xc}(\mathbf{r}; [n(\mathbf{r}), \sigma(\mathbf{r})])\right] \psi_{j,\chi}(\mathbf{r}) = \epsilon_{j,\chi} \psi_{j,\chi}(\mathbf{r}) \tag{2.22}$$

$$n_\chi(\mathbf{r}) = \sum_j f_{j,\chi} |\psi_{j,\chi}(\mathbf{r})|^2 \tag{2.23}$$

where the electron density $n(\mathbf{r})$ and spin density $\sigma(\mathbf{r})$ are given by:

$$n(\mathbf{r}) = n_\uparrow(\mathbf{r}) + n_\downarrow(\mathbf{r}) \tag{2.24}$$

$$\sigma(\mathbf{r}) = n_\uparrow(\mathbf{r}) - n_\downarrow(\mathbf{r}) \tag{2.25}$$

In the spin polarized case, the exchange-correlation functionals depend on both $n(\mathbf{r})$ and $\sigma(\mathbf{r})$ and we iteratively minimize the total energy functional $E[n(\mathbf{r}), \sigma(\mathbf{r})]$. All my calculations use spin-polarized DFT since Fe can have magnetic ordering. From now on, all discussions will focus on the spin-polarized case, where energy functionals depend on both $n(\mathbf{r})$ and $\sigma(\mathbf{r})$.

2.2   Exchange-Correlation Energy Functional

The exchange-correlation functional $E_{xc}[n(\mathbf{r})]$, as defined in the previous section, accounts for the remainder between the unknown exact energy functional and the sum of the kinetic energy of the independent-particle non interacting system, the external potential, and the Hartree term of electron interaction. This functional is independent of the external potential and solely a functional of electron density, so should work for any system. The exact exchange-correlation is unknown, so a central of part of DFT is determining effective approximations to $E_{xc}[n(\mathbf{r})]$, that perform well for the system of interest. The simplest approximation to $E_{xc}[n(\mathbf{r})]$, known as the Local Density Approximation (LDA), is an extension of the Thomas-Fermi energy for a homogeneous electron gas made spatially dependent [60]. In this approximation which requires $n(\mathbf{r})$ to vary sufficiently slowly, the functional only depends on the local value of the electron density. For the spin-polarized case, this approximation is given by:

$$E_{xc}^{LDA}[n(\mathbf{r}), \sigma(\mathbf{r})] = \int n(\mathbf{r})\epsilon_{xc}^{HEG}(n(\mathbf{r}), \sigma(\mathbf{r}))d\mathbf{r} \tag{2.26}$$

where $\epsilon_{xc}^{HEG}(n(\mathbf{r}), \sigma(\mathbf{r}))$ is the exchange-correlation energy per electron of a homogeneous uniform electron gas of density $n(\mathbf{r})$. This is an entirely local functional because it only depends on $\mathbf{r}$ and no points around it, which does not allow electrons to feel short-ranged correlation and exchange, and therefore it often predicts overly delocalized states. The simplest approximation to short-ranged exchange and correlation is to let the electrons at $\mathbf{r}$ interact with electrons at $\mathbf{r} + d\mathbf{r}$,

resulting in an energy that should go as $E \sim n(\mathbf{r}) + \nabla n(\mathbf{r})^2$. This inclusion of both the density and its gradient in a functional is called the Generalized Gradient Approximation (GGA). Because we have short-ranged correlation and exchange in our systems, we employ GGA-based functionals. These functionals have the spin-polarized form:

$$E_{xc}^{GGA}[n(\mathbf{r}), \sigma(\mathbf{r})] = E_{xc}^{LDA}[n(\mathbf{r}), \sigma(\mathbf{r})] + \int \epsilon_{xc}^{GGA}(n(\mathbf{r}), \nabla n(\mathbf{r})) d\mathbf{r} \qquad (2.27)$$

There are many different ways to choose $\epsilon_{xc}^{GGA}(n(\mathbf{r}), \nabla n(\mathbf{r}))$, each leading to distinct GGA functionals. In our calculations, we use the Perdew-Burke-Ernzerhof (PBE) form of the GGA for our exchange-correlation functional [64]. This is a completely non-empirical functional that is the most commonly used in solid-states calculations. It was constructed to retain the correct features of the LDA functional and provides good agreement to experiment for the systems that we study [65, 9, 66, 67].

2.2.1 DFT+U Method

Empirically, DFT, even with the GGA, tends to overly delocalize states [68, 69, 70]. For strongly correlated systems like the Fe-S solids we study, this causes errors in calculated properties such as lattice parameters, band gaps, and bulk moduli. To add additional correlation to DFT, a simple solution is to include an "on-site" Coulomb repulsion for electrons in the same orbital. The motivation for this choice comes from the Hubbard model in condensed matter physics, which assigns a value U to this energy [71]. This Hubbard U-term is just an extension to the normal LDA and GGA exchange-correlation functionals by adding an energy penalty for electrons occupying the same orbital. In our work, we only add the U-term correction to the Fe 3d orbitals since no other electrons in the systems we study show as strong of correlation. We use the simplified, rotationally invariant approach to DFT+U introduced by Dudarev et al. [72], which has the form:

$$E_{DFT+U} = E_{DFT} + \frac{U - J}{2} \sum_\sigma \left[\sum_j \rho_{jj}^\sigma - \sum_{j,l} \rho_{jl}^\sigma \rho_{lj}^\sigma \right] \qquad (2.28)$$

where ρ_{ij}^{σ} is the on-site density matrix of d-electrons with spin σ, and U and J are the effective on-site Coulomb repulsion and exchange energy interactions, respectively. This method is invariant with respect to the unitary transformation of the orbitals, simplifying the the calculation and requiring the input of only one parameter: $U - J$. For the rest of this dissertation, our value of U is really $U - J$ since we are using this DFT+U method. Adding the Hubbard U-term has been shown to improve the properties of transition metal sulfides and we determine the value of U for our systems by comparison to experimental parameters [16, 27].

2.3 Plane Wave Basis Sets

When we iteratively solve the KS equations, we must first define the wavefunctions of the KS orbitals, $\psi_j(\mathbf{r})$. As these are generally unknown, it is usual to expand $\psi_j(\mathbf{r})$ in a basis set composed of known functions $\phi_i(\mathbf{r})$:

$$\psi_j(\mathbf{r}) = \sum_i c_i \phi_i(\mathbf{r}) \tag{2.29}$$

where $\phi_i(\mathbf{r})$ are members of a complete set of functions with coefficient expansions c_i. In a crystal where the structure has periodic symmetry, the nuclear potential maintains the crystal periodicity:

$$V_{ext}(\mathbf{r}) = V_{ext}(\mathbf{r} + n\mathbf{a}) \tag{2.30}$$

where $\mathbf{a}$ is a lattice vector and n is an integer. In a periodic potential, Bloch's theorem [73] states that the wavefunction can be written as a product of a phase factor and periodic function:

$$\psi_{j,\mathbf{k}}(\mathbf{r}) = \frac{1}{\sqrt{N\Omega_0}} e^{i\mathbf{k}\cdot\mathbf{r}} u_{j,\mathbf{k}}(\mathbf{r}) \tag{2.31}$$

where N is the total number of unit cells, Ω_0 is the volume of a single unit cell, $\mathbf{k}$ is a wavevector confined to the first Brillouin Zone, and $u_{j,\mathbf{k}}(\mathbf{r})$ is a periodic function with the property

$u_{j,\mathbf{k}}(\mathbf{r}+n\mathbf{a}) = u_{j,\mathbf{k}}(\mathbf{r})$. Because $u_{j,\mathbf{k}}(\mathbf{r})$ is periodic, we can expand it as a sum over reciprocal lattice vectors:

$$u_{j,\mathbf{k}}(\mathbf{r}) = \sum_{\mathbf{G}} e^{i\mathbf{G}\cdot\mathbf{r}} \tilde{u}_j(\mathbf{k}+\mathbf{G}) \tag{2.32}$$

where $\mathbf{G}$ is a reciprocal lattice vector and $\tilde{u}_j(\mathbf{k}+\mathbf{G})$ are the Fourier coefficients in wavevector space. Now we can express the whole wavefunction as a sum of plane wave states $\mathbf{k}$ which differ by reciprocal lattice vectors $\mathbf{G}$:

$$\psi_{j,\mathbf{k}}(\mathbf{r}) = \sum_{\mathbf{G}} e^{i(\mathbf{G}+\mathbf{k})\cdot\mathbf{r}} \tilde{u}_j(\mathbf{k}+\mathbf{G}) \tag{2.33}$$

This plane wave expansion technically contains an infinite number of terms, so we must truncate the sum in order to handle the calculations computationally. The coefficients for the plane waves have a kinetic energy $\frac{\hbar^2}{2m} \mid \mathbf{k}+\mathbf{G} \mid^2$, so we can truncate the sum at a designated kinetic energy, E_{cut} :

$$\frac{\hbar^2}{2m} \mid \mathbf{k}+\mathbf{G} \mid^2 \le E_{cut} \tag{2.34}$$

Our wavefunction in this truncated sum is now:

$$\psi_{j,\mathbf{k}}(\mathbf{r}) = \sum_{|\mathbf{G}|\le|\mathbf{k}_{cut}|} e^{i(\mathbf{G}+\mathbf{k})\cdot\mathbf{r}} \tilde{u}_j(\mathbf{k}+\mathbf{G}) \tag{2.35}$$

This energy cutoff is an important parameter in DFT calculations; a higher E_{cut} leads to better convergence, but a greater computational cost since more plane waves are used in the basis. E_{cut} is normally determined by practice and chosen to give a certain amount of convergence.

2.4   Pseudo-Potentials

Solving the all-electron calculation in DFT is computationally expensive and requires a prohibitively large plane wave basis set to account for every electron, especially the rapidly oscillating wavefunctions of electrons in the core region. In order to reduce computational cost, we can make

a distinction between outer (valence) and inner (core) electrons. The inner electrons lie well below the energy of the outer electrons and are atomic-like, spatially localized, tightly bound core states which can be considered as inert for most chemical processes. The pseudo-potential method replaces the strong Coulomb potential and core electrons by an effective potential and replaces the valence electron wavefunctions which oscillate rapidly in the core region with pseudo-wave-functions that vary smoothly in the core region, but match the electronic wavefunction in the valence region, away from the atomic centers. A potential is called "smooth" if it does not contain any abrupt variations. Smooth potentials require less terms in its Fourier expansion and a smaller energy cutoff, leading to faster calculations. In this section, we present a basic formulation of a pseudo-potential, its required properties, and the projector augmented-wave method we use for our calculations.

We can represent the all-electron valence wavefunction $\mid \psi_v \rangle$ as a linear combination of a smooth wavefunction $\mid \phi_v \rangle$ and core electron wavefunctions $\mid \psi_c \rangle$:

$$\mid \psi_v \rangle = \mid \phi_c \rangle + \sum_c \alpha_{cv} \mid \psi_c \rangle \tag{2.36}$$

where the coefficients α_{cv} ensure orthogonality among the core and valence wavefunctions. Because of the orthogonality between the core and valence wavefunctions, Equation 2.36 becomes:

$$\mid \psi_v \rangle = \mid \phi_v \rangle + \sum_c \langle \psi_c \mid \phi_v \rangle \mid \psi_c \rangle \tag{2.37}$$

Applying Hamiltonian operator and assuming that $\mid \psi_v \rangle$ and $\mid \psi_c \rangle$ are solutions to the Schrödinger equation with eigenvalues ϵ_v and ϵ_c, respectively, we get:

$$\left[\hat{H} + \sum_c (\epsilon_v - \epsilon_c) \mid \psi_c \rangle \langle \psi_c \mid \right] \mid \phi_v \rangle = \epsilon_v \mid \phi_v \rangle \tag{2.38}$$

The smooth wavefunction $\mid \phi_v \rangle$ is the solution of this new Hamiltonian with the same eigenvalue as the all-electron valence wavefunction. The new Hamiltonian contains the projector $\hat{\mathcal{P}} = \sum_c (\epsilon_v - \epsilon_c) \mid \psi_c \rangle \langle \psi_c \mid$, which is completely repulsive and short-ranged, like a core orbital. We have replaced the all-electron problem with an effective Hamiltonian, $\hat{H} + \hat{\mathcal{P}}$, acting on smooth

wavefunctions that accurately describe the energy of the valence electrons.

Pseudo-potentials are not unique and there are different ways of generating them, though they all must produce the same core charge and eigenvalues as the atomic wavefunctions. Beyond a given cut-off radius r, $| \phi_v \rangle$ must equal $| \psi_v \rangle$ at all points. The only difference is within the cut-off radius. Also, the first and second derivatives of the pseudo-wavefunction must equal $| \psi_v \rangle$ at the cut-off radius. Finally, there cannot be any radial nodes of the pseudo-orbitals inside the cut-off radius. With these requirements, we choose to use the projector augmented-wave (PAW) method to generate our pseudo-potentials for our calculations because they compare well to the all-electron methods for our systems of interest [74, 75].

2.4.1   Projector Augmented-Wave Method

The PAW method starts with defining the transformation from our all-electron wavefunctions $| \psi_n \rangle$ to a smooth auxiliary wavefunction $| \tilde{\psi}_n \rangle$ that can be represented in a plane wave expansion. All smooth functions and properties will be designated with a tilde in this section. These auxiliary wavefunctions are linear transformations of the all-electron wavefunctions, lie in a new Hilbert space, and are computationally less expensive than $| \psi_n \rangle$. The linear transformation operator $\mathcal{T}$ takes the smooth pseudo wavefunction to the all-electron wavefunction:

$$| \psi_n \rangle = \mathcal{T} | \tilde{\psi}_n \rangle \tag{2.39}$$

where any expectation value A has the form:

$$\langle A \rangle = \langle \tilde{\psi}_n \left| \mathcal{T}^\dagger A \mathcal{T} \right| \tilde{\psi}_n \rangle \tag{2.40}$$

We can construct augmentation spheres $| \mathbf{r} - \mathbf{R}^a | < r_c^a$ around each atom, where a is the atom index, r_c^a is a cut-off radius, and $\mathbf{R}^a$ is the nuclear position. The cut-off radii r_c^a should be chosen that there is no overlap of augmentation spheres between atoms. We now write $\mathcal{T}$ as:

$$\mathcal{T} = \mathbf{1} + \sum_a \mathcal{T}^a \tag{2.41}$$

where $\mathcal{T}^a$ only acts inside the augmentation sphere. Within the augmentation spheres, we expand the true wavefunction in a complete basis of partial waves $|\phi_i^a\rangle$, where we obtain the smooth partial waves by using the $\mathcal{T}$ operator:

$$|\phi_i^a\rangle = \mathcal{T}|\tilde{\phi}_i^a\rangle = (\mathbf{1} + \mathcal{T}^a)|\tilde{\phi}_i^a\rangle \tag{2.42}$$

Because $\mathcal{T}^a$ only acts within the augmentation sphere, the partial waves must align outside the sphere: $|\phi_i^a\rangle = |\tilde{\phi}_i^a\rangle$ for $r > r_c^a$. Since the partial waves form a complete basis, we can expand the smooth all-electron wavefunction as:

$$|\tilde{\psi}_n\rangle = \sum_i P_{ni}^a|\tilde{\phi}_i^a\rangle \tag{2.43}$$

where P_{ni}^a are undetermined expansion coefficients. Since $|\phi_i^a\rangle = \mathcal{T}|\tilde{\phi}_i^a\rangle$, we see that the expansion of $|\psi_n\rangle$ has the same coefficients P_{ni}^a:

$$|\psi_n\rangle = \sum_i P_{ni}^a|\phi_i^a\rangle \tag{2.44}$$

We require the transformation $\mathcal{T}$ to be linear, so the coefficients must be linear functions of the smooth wavefunctions. Hence, the coefficients are scalar products of the smooth wavefunction with a set of fixed functions $|\tilde{p}_i^a\rangle$, called projector functions:

$$P_{ni}^a = \langle \tilde{p}_i^a|\tilde{\psi}_n\rangle \tag{2.45}$$

The orthogonality and completeness relations inside the augmentation spheres place the following restrictions on the projector functions:

$$\langle \tilde{p}_i^a|\tilde{\phi}_j^a\rangle = \delta_{ij} \tag{2.46}$$

$$\sum_i \mid \tilde{\phi}_i^a \rangle \langle \tilde{p}_i^a \mid = \mathbf{1} \tag{2.47}$$

The projector functions are localized in the augmentation sphere, and the most general form of these functions is:

$$\langle \tilde{p}_i^a \mid = \sum_j \left\{ \langle f_k^a \mid \tilde{\phi}_l^a \rangle \right\}_{ij}^{-1} \langle f_j^a \mid \tag{2.48}$$

where $\mid f_k^a \rangle$ is any set of linearly independent functions. Now we can rewrite both wavefunctions in terms of the projector functions and partial waves:

$$\mid \tilde{\psi}_n \rangle = \sum_i \langle \tilde{p}_i^a \mid \tilde{\psi}_n \rangle \mid \tilde{\phi}_i^a \rangle \tag{2.49}$$

$$\mid \psi_n \rangle = \sum_i \langle \tilde{p}_i^a \mid \tilde{\psi}_n \rangle \mid \phi_i^a \rangle \tag{2.50}$$

We can also express $\mathcal{T}$ in terms of the projector operators:

$$\mathcal{T} = \mathbf{1} + \sum_a \sum_i \left(\mid \phi_i^a \rangle - \mid \tilde{\phi}_i^a \rangle \right) \langle \tilde{p}_i^a \mid \tag{2.51}$$

Now the all-electron wavefunction can be obtained from the all-electron partial waves $\mid \phi_i^a \rangle$, the smooth partial waves, $\mid \tilde{\phi}_i^a \rangle$, that coincide with the corresponding all-electron partial wave outside the augmentation sphere, and the smooth projector functions $\mid \tilde{p}_i^a \rangle$:

$$\mid \psi_n \rangle = \mid \tilde{\psi}_n \rangle + \sum_a \sum_i \left(\mid \phi_i^a \rangle - \mid \tilde{\phi}_i^a \rangle \right) \langle \tilde{p}_i^a \mid \tilde{\psi}_n \rangle \tag{2.52}$$

2.5   Wannier90

The results from DFT represent the adiabatic solution to the Schrödinger equation: the system is represented in terms of extended Bloch orbitals $\psi_{n\mathbf{k}}(\mathbf{r})$, characterized by the good quantum numbers n and $\mathbf{k}$, which refer to the band number and crystal momentum, respectively. In this

representation, the states are delocalized and composed of linear combinations of the atomic orbitals. Another representation of the system uses the diabatic solution to the Schrödinger equation to create localized orbitals. Called maximally-localized Wannier functions (MLWFs) $w_{n\mathbf{R}}(\mathbf{r})$, these orbitals originate from a unitary transformation of the Block orbitals, where n is the orbital number and $\mathbf{R}$ is the lattice site of the unit cell the function belongs to. This representation, calculated through the Wannier90 program [59], presents a real-space picture of the electronic structure of the system and can provide insight into chemical processes that are difficult to understand under the Bloch representation. For an isolated set of energy bands, we can write the MLWFs in terms of a set of Bloch states:

$$w_{n\mathbf{R}}(\mathbf{r}) = \frac{V}{(2\pi)^3} \int_{BZ} \left[\sum_m U_{mn}^{(\mathbf{k})} \psi_{m\mathbf{k}}(\mathbf{r}) \right] e^{-i\mathbf{k}\cdot\mathbf{R}} d\mathbf{k} \tag{2.53}$$

where V is the volume of the unit cell, $U^{(\mathbf{k})}$ is a unitary matrix that mixes Bloch states at each wave-vector $\mathbf{k}$, and the integral is over the first Brillouin Zone (BZ). $U^{(\mathbf{k})}$ is not uniquely defined, therefore different choices of $U^{(\mathbf{k})}$ will lead to different MLWFs of varying spatial spreads. The choice of unitary matrix is called the gauge choice, where gauge is another term for the unitary matrix. To choose the best gauge, we minimize the sum of the quadratic spreads around the center of each MLWFs. Given by Ω, the sum of the quadratic spreads has the form:

$$\Omega = \sum_n \left[\langle w_{n\mathbf{0}} \left| r^2 \right| w_{n\mathbf{0}} \rangle - |\langle w_{n\mathbf{0}} \left| \mathbf{r} \right| w_{n\mathbf{0}} \rangle|^2 \right] \tag{2.54}$$

We can split the total spread into a gauge invariant term Ω_I and a gauge dependent term $\tilde{\Omega}$ that both take on positive values:

$$\Omega = \Omega_I + \tilde{\Omega} \tag{2.55}$$

$$\Omega_I = \sum_n \left[\langle w_{n\mathbf{0}} \left| r^2 \right| w_{n\mathbf{0}} \rangle - \sum_{m\mathbf{R}} |\langle w_{m\mathbf{R}} \left| \mathbf{r} \right| w_{n\mathbf{0}} \rangle|^2 \right] \tag{2.56}$$

$$\tilde{\Omega} = \sum_n \sum_{\mathbf{R} \neq 0} |\langle w_{n\mathbf{R}} |\mathbf{r}| w_{n\mathbf{0}} \rangle|^2 + \sum_{m \neq n} \sum_{\mathbf{R}} |\langle w_{m\mathbf{R}} |\mathbf{r}| w_{n\mathbf{0}} \rangle|^2 \tag{2.57}$$

where the diagonal and off-diagonal elements make up the first and second terms of $\tilde{\Omega}$, respectively. Since only $\tilde{\Omega}$ changes with gauge choice, we iteratively minimize $\tilde{\Omega}$ with respect to the set of $U^{(\mathbf{k})}$ to obtain the MLWFs. The procedure above, called the wannierization procedure, only works for an isolated set of bands where the selected bands do not intersect with any bands outside the set, e.g., the valence bands of an insulator. For entangled energy bands, where we cannot easily separate the set of bands from the surrounding bands like in metallic systems or conduction bands of an insulator, we must use the "disentanglement" procedure to obtain the MLWFs. Because the bands are not isolated, we define an energy window in which to calculate an orthonormal set of Bloch states at each k-point to use in the generation of the MLWFs. At a given k-point $\mathbf{k}$, $N_{win}^{(\mathbf{k})}$ states lie within the defined energy window. We can obtain a set of N Bloch states, defining an N-dimensional subspace $\mathcal{S}(\mathbf{k})$, where $N \leq N_{win}^{(\mathbf{k})}$ by performing a unitary transformation amongst the Bloch states which fall within the energy window at $\mathbf{k}$:

$$u_{n\mathbf{k}}^{opt}(\mathbf{r}) = \sum_{m \in N_{win}^{(\mathbf{k})}} U_{mn}^{dis(\mathbf{k})} u_{m\mathbf{k}}(\mathbf{r}) \tag{2.58}$$

where $u_{n\mathbf{k}}(\mathbf{r}) = e^{-i\mathbf{k}\cdot\mathbf{r}} \psi_{n\mathbf{k}}(\mathbf{r})$ is the periodic part of the Bloch function and $U_{mn}^{dis(\mathbf{k})}$ is a unitary rectangular $N_{win}^{(\mathbf{k})} \times N$ matrix. Now Ω_I is invariant under gauge transformations within a given subspace, but depends on $\mathcal{S}(\mathbf{k})$. The disentanglement procedure minimizes $\tilde{\Omega}$ with respect to the set of $U^{dis(\mathbf{k})}$ to obtain the optimized Bloch functions from the given energy window, since Ω_I is a measure of the degree of mismatch between the subspaces $\mathcal{S}(\mathbf{k})$ and $\mathcal{S}(\mathbf{k} + \mathbf{b})$.

When dealing with entangled energy bands, two minimizations occur:

(1) Disentanglement: minimize Ω_I with respect to $U^{dis(\mathbf{k})}$ to obtain a set of $u_{n\mathbf{k}}^{opt}(\mathbf{r})$ within a defined energy window.

(2) Wannierization: minimize $\tilde{\Omega}$ with respect to $U^{(\mathbf{k})}$ using $u_{n\mathbf{k}}^{opt}(\mathbf{r})$ to obtain the MLWFs

$w_{n\mathbf{R}}(\mathbf{r})$.

The Bloch states of the optimal subspace obtained from the disentanglement procedure may not correspond to any of the original states due to mixing between states. In order to preserve the exact properties of a system in a given energy range, e.g., around the Fermi level, we introduce a second smaller energy window. States within this second energy window, $N_{froz}^{(\mathbf{k})}$, remain unchanged in the optimal subspace, $u_{n\mathbf{k}}^{opt}(\mathbf{r}) = u_{n\mathbf{k}}(\mathbf{r})$ for $n \in N_{froz}^{(\mathbf{k})}$. We define this second window as the inner or frozen window. The outer and inner windows are important parameters in the Wannier90 calculation since they control the MLWF representation of the system. The windows are normally determined by their ability to converge and minimization of the total spread.

The disentanglement procedure begins with an initial guess of the subspace $\mathcal{S}(\mathbf{k})$ by defining a set of N trial functions $g_n(\mathbf{r})$, $n \in [1, N]$, as an initial approximation to the N MLWFs. These trial functions are constructed out of the atomic orbitals of the hydrogen atom, given by the good quantum numbers n, l, and m. Localized in space at each atom, the angular part of the trial function is given by the real states Θ_{lm_r}, which is simply a unitary transformation of the spherical harmonics Y_{lm} of the hydrogenic Schrödinger equation. Once defined, the $g_n(\mathbf{r})$ are projected onto the cell-periodic parts of the $N_{win}^{(\mathbf{k})}$ Bloch states $u_{n\mathbf{k}}(\mathbf{r})$ inside the defined energy window:

$$\phi_{n\mathbf{k}}(\mathbf{r}) = \sum_{m=1}^{N_{win}^{(\mathbf{k})}} A_{mn}^{(\mathbf{k})} u_{m\mathbf{k}}(\mathbf{r}) \tag{2.59}$$

where $A_{mn}^{(\mathbf{k})} = \langle u_{m\mathbf{k}} \mid g_n \rangle$ is an $N_{win}^{(\mathbf{k})} \times N$ matrix of the projection of the Block states onto the trial functions. These Bloch states can be generated by any ab inito program. In our work, we use DFT to generate the Block states used for Wannier90.

After finding the projection of our trial functions onto the DFT determined Bloch states, we must orthonormalize the resulting states $\phi_{n\mathbf{k}}(\mathbf{r})$ which serves as the initial step in the disentanglement minimization:

$$u_{n\mathbf{k}}^{opt}(\mathbf{r}) = \sum_{m=1}^{N} \left(S^{-1/2} \right)_{mn} \phi_{m\mathbf{k}}(\mathbf{r}) \tag{2.60}$$

where $S = \langle \phi_{m\mathbf{k}} \mid \phi_{n\mathbf{k}} \rangle = (A^\dagger A)_{mn}$. Plugging in equation 2.59 for $\phi_{m\mathbf{k}}(\mathbf{r})$, we get:

$$u_{n\mathbf{k}}^{opt}(\mathbf{r}) = \sum_{m=1}^{N_{win}^{(\mathbf{k})}} \left(AS^{-1/2} \right)_{mn} u_{m\mathbf{k}}(\mathbf{r}) \tag{2.61}$$

where $AS^{-1/2}$ is used as the initial guess for $U^{dis(\mathbf{k})}$.

In summary, the Wannier90 program constructs MLWFs through multiple unitary transformations of Bloch orbitals generated from an ab initio program. The unitary transformations are not unique, so the MLWFs are iteratively calculated to minimize the sum of the quadratic spread around the center of each function.

Chapter 3

Iron Deficient Troilite and the Pyrrhotites

3.1   Introduction

Because of the complicated nature of the phase-diagram for Fe-S solids, little is known computationally about the electronic structure of the pyrrhotite family. The DFT results reported for the electronic properties of troilite, the most studied member of the pyrrhotite family, remain inconsistent. This suggests that the properties of FeS materials are sensitive to choices in DFT methodology and difficult to elucidate. Some reports using the GGA class of functionals, but different pseudo-potentials, calculate a slightly insulating state in troilite [9, 24], while others see no band gap [76, 27, 77, 16]. The Fe d-electrons in these materials also exhibit strong correlation, so we must include U in our DFT calculations, which may only be weakly or non-transferrable between Fe-S crystal structures. Because of these computational challenges, the properties of pyrrhotites remain poorly understood, especially the role that Fe defects have on these materials.

In this chapter, we thoroughly investigate the role of iron vacancy defects on the structural and electronic properties of the near stoichiometric Fe-S solid with DFT, and compare it with defect-free troilite and pyrrhotite-4M, our collaborator's experimentally synthesized nanoparticles. Because troilite is the end-group compound in this study, we use it as a computational reference system. These calculations only scratch the surface of the host of different pyrrhotite geometries and properties. Our use of Fe defective troilite as a comparison to the pyrrhotites is a first approximation that may provide insight into some of the complicated nature of these materials. We also calculate and characterize, for the first time, the phonon modes of troilite.

Parts of this chapter have been adapted from the paper titled "Nanocrystalline Iron Mono-sulfides Near Stoichiometry", which was published in 2018 in *Scientific Reports*.

3.2   Determination of U for Troilite

Since troilite contains Fe atoms that have strongly correlated d-electrons, we must use U to more accurately model the repulsive electron-electron interactions. U is an added energy term to the Hamiltonian that acts as a repulsive force against two electrons of different spins occupying the same site. The Fe 3d-orbital electrons exhibit the strongest on-site correlation, so we only add U to the Fe 3d electrons. In this DFT+U scheme, we must optimize U before performing Fe vacancy calculations for troilite. U is normally determined by comparison of the calculated structure to experimentally determined values such as lattice constants, molar volume, band gap, bulk modulus, and magnetic moments [16, 27]. The value of U that yields a structure best matching experiments is considered to be optimized and used in subsequent calculations. For iron pyrite, U is widely accepted as 2 eV [67, 78, 66, 26], but this value may only be weakly transferable between systems since at least one study finds different values for the optimal U between pyrite, MnP-type FeS, and troilite [27]. The optimal value of U for troilite is not agreed upon in the literature, so we must optimize it for our calculations.

We determined the optimal value of U, defined to be U^*, by comparison to the known experimental structural parameters of troilite. Since the band gap of troilite is not well known experimentally, we chose to use only the experimental lattice parameters for comparison [79]. Starting with the synthetic troilite unit cell of Andresen [79] listed in Table 3.1, we relaxed both the atoms and unit cell dimensions at values of U ranging from 0 eV to 2 eV. All structures were fully relaxed with forces on each atom less than 0.001 eV/Å and an external pressure of 0 ± 0.05 kB for the unit cell.

Figures 3.1 and 3.2 show the monotonic increase of the band gap and all structural parameters as the value of U increases. The increase of parameters occurs due to the increase in correlation of the Fe d-electrons; the increasingly repulsive nature of the Fe d-electrons causes the structure to

Table 3.1: Literature values of synthetic troilite from the Andresen paper [79]. Wyckoff positions are labeled in direct lattice units.

Volume = 362.366 Å^3	a = 5.97 Å	c = 11.74 Å	c/a = 1.9665
Atom: Wyckoff Position	x	y	z
S: 2a	0	0	0
S: 4f	–	–	0.016
S: 6h	2/3	0	–
Fe: 12i	0.3833	0.05	1/8

expand and the band gap to increase. Using the unit cell volume, which incorporates both lattice constants, we find $U^* = 1.4$ eV best matches the experimental structure (see Figure 3.2). $U = 1.4$ eV gives a hexagonal unit cell for troilite with lattice parameters a = b = 5.960 Å, c = 11.773 Å, a unit cell volume of 362.22 Å^3, and matches the experimental values for these parameters to within 0.5%. We also note that compared to the other relaxed structures given in Table 3.2, $U = 1.4$ eV gives the lowest average and total error of all structural parameters compared to experiment. Compared to previous calculations, our U^* is slightly larger than some reports, but comparable to others [16, 27, 9].

3.3   Other Computational Considerations

Our choice of pseudo-potentials, based on the projector augmented-wave (PAW) method [74, 75], are harder than those used in previous studies and incorporate more valence electrons. These potentials are therefore minimally approximate with respect to both the earlier studies and the all-atom orbitals. Our pseudo-potentials contain 6 valence electrons per sulfur atom and 16 electrons for each iron. Hard pseudo-potentials require a larger basis set than soft pseudo-potentials, and thus come with an increase in computational cost. For these pseudo-potentials, we determined an optimal plane wave energy cutoff that ensures sufficient energy convergence without great computational expense. Figure 3.3 shows the total energy of a troilite unit cell as a function

Table 3.2: Calculated unit cell parameters as a function of the value of U. All calculations converged with forces on each atom less than 0.001 eV/Å and an external pressure within 0.05kB of zero. The values in bold represent the optimal parameters that best match the experimental unit cell listed in Table 3.1.

U (eV)	Volume ($Å^3$)	Total Energy (eV)	a (Å)	c (Å)	c/a	Band gap (eV)
0	341.39	-157.65624	5.89761	11.33363	1.921732	0.1737
0.25	347.03	-155.08750	5.91019	11.47171	1.941006	0.2951
0.5	351.33	-152.63731	5.92179	11.56848	1.953547	0.3890
0.75	354.87	-150.28017	5.93284	11.64174	1.962254	0.4770
1	357.94	-147.99797	5.94366	11.69954	1.968407	0.5662
1.25	360.69	-145.78108	5.95418	11.74776	1.973026	0.6582
1.4	**362.22**	**-144.47839**	**5.96036**	**11.77324**	**1.975255**	**0.7103**
1.5	363.20	-143.62047	5.96442	11.78905	1.976563	0.7437
1.75	365.54	-141.51058	5.97433	11.82576	1.979430	0.8237
2	367.76	-139.44677	5.98406	11.85884	1.981739	0.9082

Figure 3.1: Relationship of U with a) lattice constant a, b) lattice constant c, and c) band gap. All values monotonically increase with increasing U, due to the increasingly repulsive nature of the electrons on the same Fe 3d-orbitals.
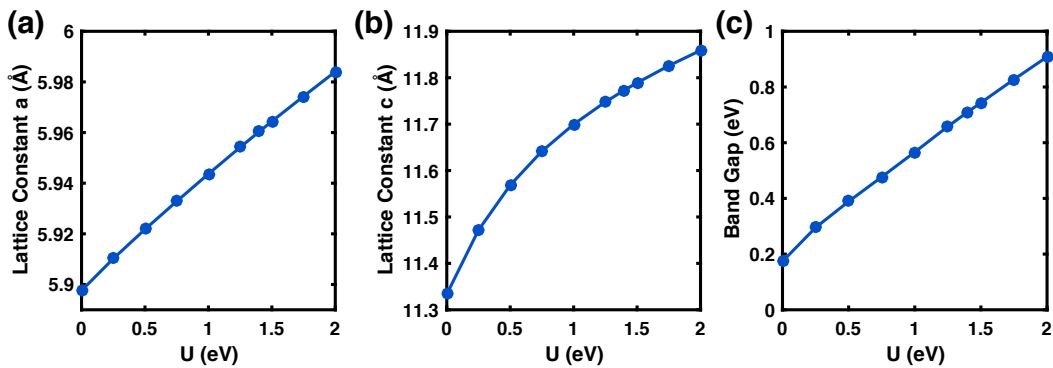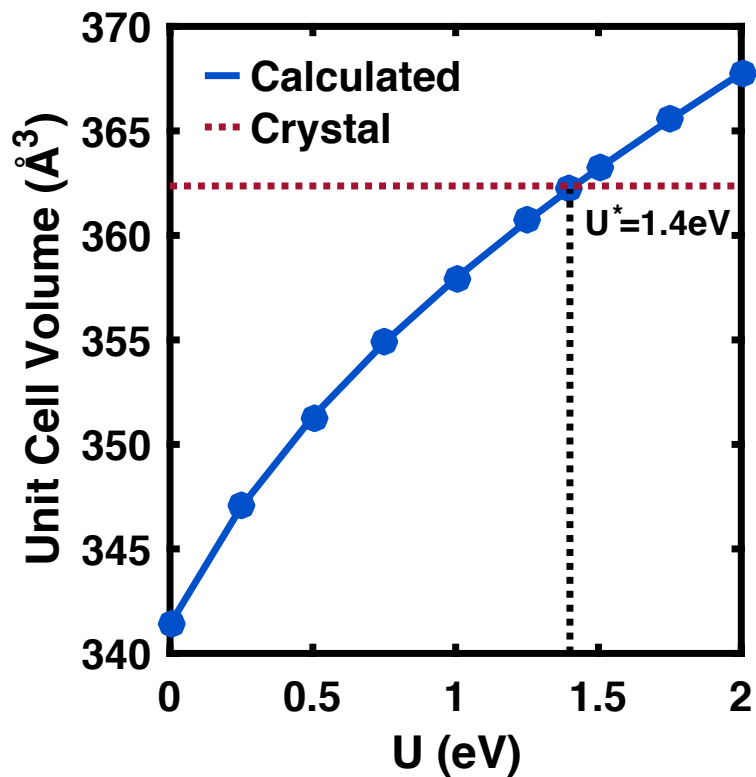
Figure 3.2: Relationship of U and unit cell volume. U^*=1.4 eV represents the value of U that most closely matches the experimental unit cell volume, and we use this value for U in subsequent calculations.
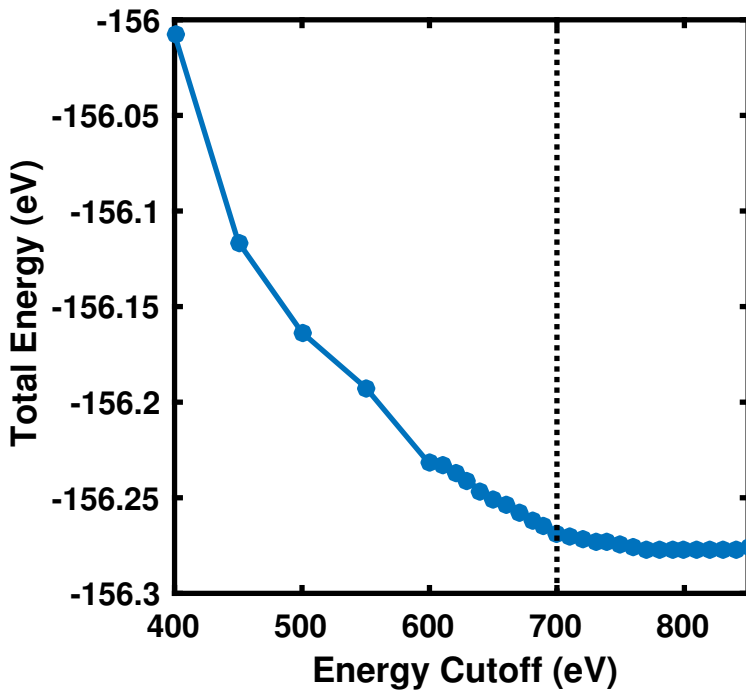
of energy cutoff. From this study, we choose 700 eV as the optimal energy cutoff since the energy is converged to within 10 meV per unit cell without adding undue computational cost. Our cutoff energy of 700 eV is much larger (1.3-2X larger) than all earlier studies done on troilite, making our calculations the most accurate yet within the realm of DFT since we use the largest basis set [9, 24, 76, 27, 77, 16].

We relaxed all troilite structures, defective and non-defective, starting from the non-defective experimental troilite crystal structure of Andresen [79]. From this experimental structure, we generated defective structures by removing one iron atom, which corresponds to a defect concentration of 1/12, or about 8.3 atomic percentage iron deficient. We checked that the reported structural and electronic results are insensitive to which atom gets removed by removing all 12 different iron atoms in the unit cell and repeating the structural minimization and density of states calculations. Using the conjugate gradient method, we moved the atomic positions and unit cell dimensions at constant pressure until the forces in each self-consistent cycle were less than 1 meV/Å. The wave vector spacing was based on an 8x8x4 Γ-centered Monkhorst-pack grid. For the electronic density of states (DOS) calculations in troilite, we used a 19x19x10 grid. Both grid choices sample the Wigner-Seitz cell evenly in all directions. For the pyrrhotite-4M DOS calculations, we used an 8x15x8 k-point grid and fixed the nuclear coordinates at the experimentally determined values [15]. All energies were converged to within 1×10^{-8} eV in each self-consistency cycle using Gaussian smearing with a width of 0.01 eV. We generated and visualized all crystal structures using the XCrySDen visualization package [80].

3.3.1   Magnetism

Both troilite and pyrrhotite exhibit magnetic ordering due to the presence of Fe in the material. The spin states on the iron atoms in the troilite phase exhibit an interesting magnetic structure shown in Figure 3.4a, where the irons are aligned ferromagnetically in the a-b plane (x-y plane) and these ferromagnetic planes alter antiferromagnetically along the c axis (z axis) with magnetic moments close to $\pm 4\mu_B$ [76, 17, 9, 14]. This rich magnetic structure is often referred to

Figure 3.3: Total calculated energy per unit cell versus energy cutoff for troilite. At an energy cutoff of 700 eV, denoted by the vertical dashed line, the total energy of the system is within 10 meV of the lowest calculated energy with a much higher energy cutoff. We use the energy cutoff of 700 eV for all subsequent calculations since it achieves energy convergence while maintaining computational feasibility and is larger than any previous calculations performed on troilite.

as antiferromagnetic since the spins cancel each other out on the macroscopic scale, but to just say that troilite is antiferromagnetic does not capture the full magnetic structure of the material. The magnetic structure of pyrrhotite-4M is not as well-known, though we would expect to see a similar ordering to troilite since the two crystal structures are both based on the same NiAs structure. Table 3.3 shows the results of different magnetic initializations on the fixed experimental unit cell. The lowest energy magnetic ordering, visualized in Figure 3.4b, is antiferromagnetic, like troilite, with planes of ferromagnetically aligned Fe atoms in the x-y plane that are antiferromagnetically aligned along the z axis. The magnetic moment on each iron is roughly $\pm 3\mu_B$, less than troilite's magnetic moments of $\pm 4\mu_B$. Our calculated magnetic structure of pyrrhotite-4M is consistent with Powell et al., the one known study of the magnetic structure of pyrrhotite-4M [15]. They also see antiferromagnetic alignment along the z-axis with ferromagnetically aligned planes, though the magnetic moments on each iron point slightly off the c-axis. Do to the nature of our collinear calculations, we will not see this phenomena since the magnetic moments are confined to the $\pm$z direction. It is interesting to note that the layers of Fe atoms in pyrrhotite-4M are not equal in number, so the entire structure exhibits a nonzero magnetic moment in its ground state. This material could be said to be ferrimagnetic since the amplitude of the magnetic moments on each of the Fe atoms are not identical. In all subsequent calculations, we initialized the Fe-S structures in their respective magnetic ground states.
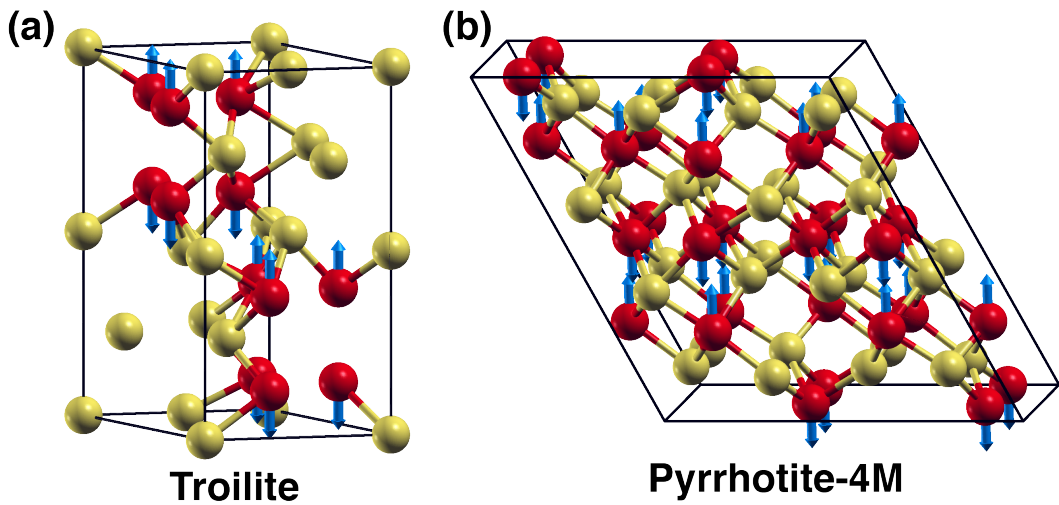
3.4   Defect-Free Band Structure

After determining $U^* = 1.4$ eV for troilite, we calculated the band structure and electronic density of states (DOS) of the defect-free material, shown in Figure 3.5. The band structure of a material provides insight into the effective masses of the band edge carriers: holes at the valence band maximum and electrons at the conduction band minimum. We can determine the effective carrier masses of the material by expanding the energy at the band edge extremum, E^*, located at $\mathbf{k}^*$, into quadratic plus higher order terms [71]. Ignoring the higher order terms, this has the form:

Table 3.3: Results of Pyrrhotite-4M magnetic ground state study with $U = 1.4$ eV, where the magnetic moments are given in the order of the Fe atom number in the input file. The antiferromagnetic (AFM) state with planes of alternating ferromagnetic iron atoms is the ground state for pyrrhotite-4M since it has the lowest energy. Since the number of spin up and spin down Fe atoms is unequal there exists an overall magnetism in the structure.

Magnetic Initialization (μ_B)	Final Magnetic Moments (μ_B)	Total Energy (eV)
Nonmagnetic ($0\mu_B$ on each Fe)	~ 0 on each Fe	-330.63177
Ferromagnetic ($+3\mu_B$ on each Fe)	~ 2.8 on each Fe	-346.98743
AFM 1 (8*-3 8*3 8*-3 4*3)	-2.96($\times$8) 3.2($\times$8) -2.97($\times$8) 3.1($\times$4)	-352.85823
AFM 2 (8*3 8*-3 8*3 4*-3)	2.96($\times$8) -3.2($\times$8) 2.97($\times$8) -3.1($\times$4)	-352.85823
AFM 3 (8*-2 8*2 8*-2 4*2)	-2.94($\times$8) 3.2($\times$8) -2.95($\times$8) 3.1($\times$4)	-352.85823
AFM 4 ($\pm$ 3)	$\pm$3	-350.40380

Figure 3.4: Unit cell structures and magnetic ordering of a) troilite and b) pyrrhotite-4M, where Fe and S are labeled red and yellow, respectively. The blue arrows correspond to the magnitude and direction of the magnetic moment on each Fe atom. All magnetic moments are aligned in the $\pm$z-axis for these calculations.

(a)

Troilite

(b)

Pyrrhotite-4M

$$E = E^* + \alpha \mid \mathbf{k} - \mathbf{k}^* \mid^2 \tag{3.1}$$

where α is some constant that determines the curvature of the function. The effective mass m^* is given by:

$$m^* = \frac{\hbar^2}{\left(\frac{\partial^2 E}{\partial k^2}\right)} = \frac{\hbar^2}{2\alpha} \tag{3.2}$$
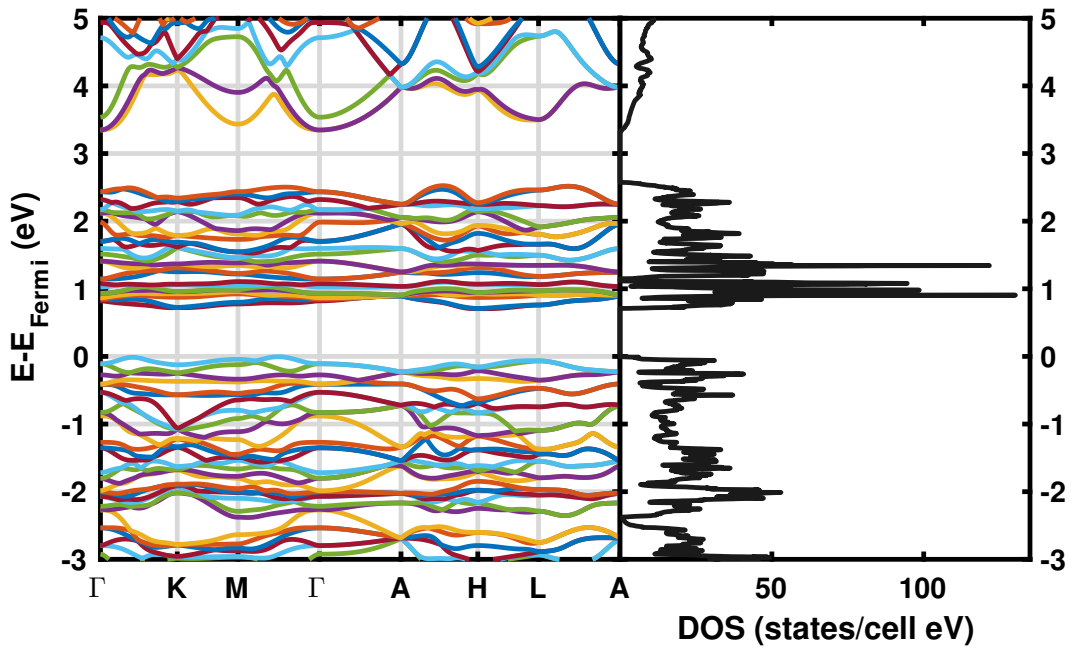
Note that m^* is inversely proportional to α, so a band edge with a large curvature contains relatively "light" or "massless" carriers with a small effective mass. This also means that flat band edges contain carriers very "heavy" carriers with a large effective mass.

Defect-free troilite has an indirect band gap of 0.71 eV. The band gap is indirect because the valence band maximum and conduction band minimum occur at different wavevectors. Consistent with the study done by Ricci et al. [9], both the conduction and valence band carriers are fairly heavy with the indirect transition originating halfway between the M and Γ points and ending very close to the H point.

3.5   Fe-Vacancy Results

In our defect studies of FeS, we started with troilite, the stoichiometric end group of the pyrrhotite family. This is a reasonable approach because both troilite and the pyrrhotites are based on the NiAs crystal structure, and there may be a near continuum of stable structures between defective troilite and stable pyrrhotites. Figure 3.6(b) shows the electronic density of states (DOS) for the stoichiometric and Fe-vacant structures. With no defects, the troilite unit cell maintains its *P-62c* symmetry and is insulating with a band gap of 0.71 eV. This band gap is larger than that reported in recent DMFT calculations [81, 82], but similar to that reported in another DFT+U paper [9]. Once we introduce a single neutral iron vacancy, the structure distorts from hexagonal into a monoclinic cell resembling a pyrrhotite phase with a = 5.937 Å, b = 5.991 Å, c = 11.655 Å, and unit cell volume = 359.52 Å^3, shown in Fig. 3.6(a). We define this fully relaxed, monoclinic

Figure 3.5: Band structure and DOS of troilite with $U = 1.4$ eV. Both the conduction and valence bands are quite massive with a nearly wavevector invariant energy. The indirect band gap of 0.71 eV originates between the M and Γ points of the valence band maximum and ends near the H point of the conduction band minimum.

structure as iron deficient troilite. Table 3.4 lists the structural parameters of both defect-free troilite and iron deficient troilite for each Fe vacancy possible in the unit cell. We see that the structural parameters and total energy remain within 0.8% irregardless of which Fe was removed from the unit cell. The electronic structure also remains insensitive to vacancy placement as seen in Figure 3.7. All defective structures have effectively the same DOS with band gap of 0 eV, where the DOS goes to zero at the Fermi energy.

The structural and electronic changes to iron deficient troilite are insensitive to which iron atom gets removed, suggesting that our computational realizations of iron deficient troilite is similar to what one might call a type of pyrrhotite with the atomic formula $Fe_{11}S_{12}$. Although iron deficient troilite resembles a pyrrhotite structure more closely than troilite, we cannot classify it as such since it does not have the same stoichiometry as pyrrhotite-4M (Fe_7S_8) and does not share crystal symmetries with the $Fe_{11}S_{12}$ polytype pyrrhotite-6C. Since iron deficient troilite is a fully relaxed structure, it supports the presence of stable intermediates existing between troilite and pyrrhotite. Our results suggest that iron defects cause a local structural distortion in troilite, but these distortions have a correlation length that is short on the scale of an individual unit cell. If the results for the crystal structure or density of states depended strongly on which Fe atom was removed, then our computational model for an iron-deficient structure would represent a periodically defective structure that would not be a faithful model for experimental crystal structures whose vacancies appear more randomly.

The band gap of the defective structure completely closes and remains ungapped as U goes from 0 to 1.4 eV, which shows robustness with respect to the parameterization of U. One may think of the gap closing due to the appearance of midgap states composed of Fe d-orbitals clustering into an already narrow band. These midgap states are likely Fe d-orbitals since the projected DOS, displayed in Figure 3.8, shows that the states on both sides of the Fermi energy are composed almost entirely of Fe d-orbitals. In solids with wider gaps, disorder-induced states lead to so-called Urbach tails in the absorption spectrum [83, 84].

To further investigate the relationship between troilite and pyrrhotite, we calculated the DOS

Figure 3.6: Structural and electronic deviations in FeS with and without a Fe vacancy. Panel a) shows a shift from hexagonal (blue) to monoclinic (black) geometry with the removal of an iron atom, where iron and sulfur are labeled red and yellow, respectively. The semi-transparent Fe atom denotes the vacancy in the defective structure. Spatial movements of the atoms between the defect-free and defective structure are not shown here; the atoms in the figure are included to provide context for the troilite unit cell viewed along the c-axis. The density of states for FeS with and without an iron vacancy is illustrated in b) by black and blue curves, respectively, and shows a decrease in band gap from 0.71 eV to 0 eV with the introduction of a Fe vacancy.
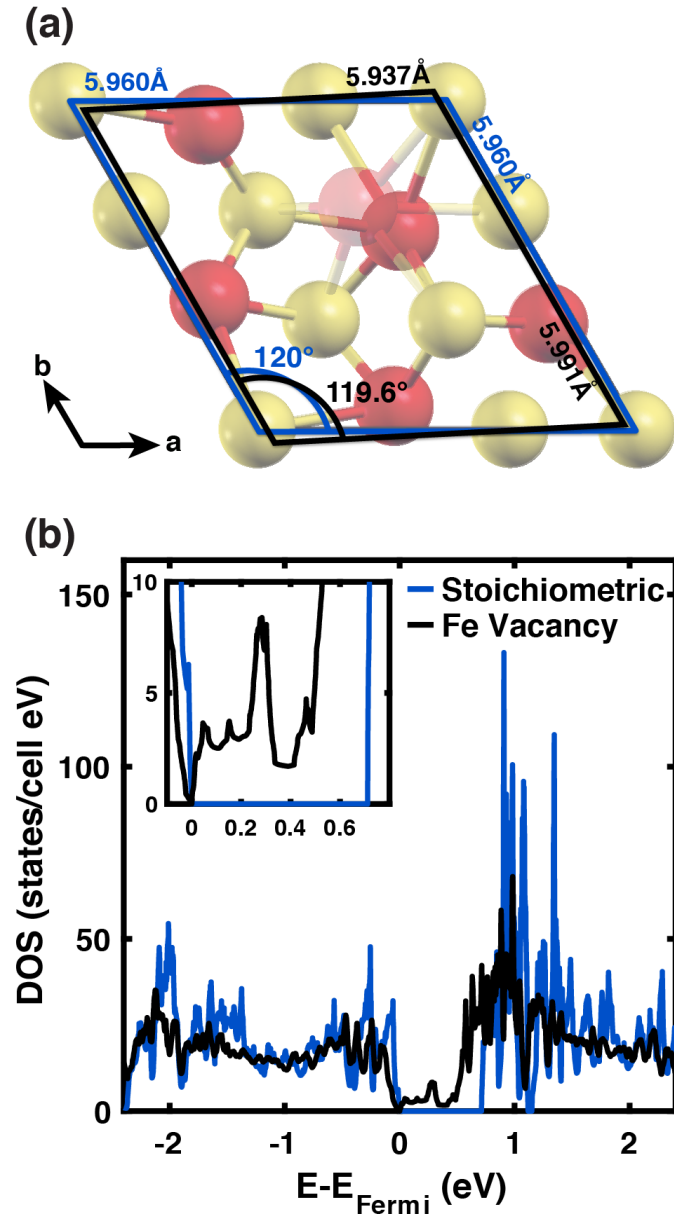
Table 3.4: Lattice parameters for every possible iron deficient troilite unit cell. Each unit cell is labeled with the atom number of the vacant iron, and each structure was fully relaxed with forces on each atom less than 0.001 eV/Å and an external pressure within 0.04kB of zero. The lattice parameters of all the iron deficient unit cells remain within 0.8% of each other, irregardless of the position of the vacant Fe atom.

Type	a (Å)	b (Å)	c (Å)	Volume (Å^3)	Total Energy (eV)
No vac	5.960364	5.960364	11.77324	362.22	-144.47851
Fe1vac	5.976705	5.991489	11.65497	359.53	-136.63565
Fe2vac	5.937278	5.976771	11.65480	359.52	-136.63564
Fe3vac	5.937203	5.991446	11.65488	359.52	-136.63562
Fe4vac	5.976642	5.991433	11.65486	359.52	-136.63561
Fe5vac	5.937128	5.976849	11.65449	359.51	-136.63560
Fe6vac	5.937195	5.991264	11.65483	359.51	-136.63563
Fe7vac	5.976657	5.991451	11.65487	359.52	-136.63562
Fe8vac	5.937209	5.976653	11.65489	359.52	-136.63563
Fe9vac	5.937197	5.991443	11.65475	359.52	-136.63563
Fe10vac	5.976646	5.991447	11.65487	359.52	-136.63563
Fe11vac	5.937200	5.976651	11.65487	359.52	-136.63562
Fe12vac	5.937181	5.991481	11.65475	359.52	-136.63562

Figure 3.7: DOS of all possible Fe vacancies in an iron deficient troilite unit cell. Irregardless of the position of the Fe vacancy, the DOS all line up on the same curve. The insert in the figure shows that the band gap of the material is zero even though the DOS goes to zero at the Fermi energy.
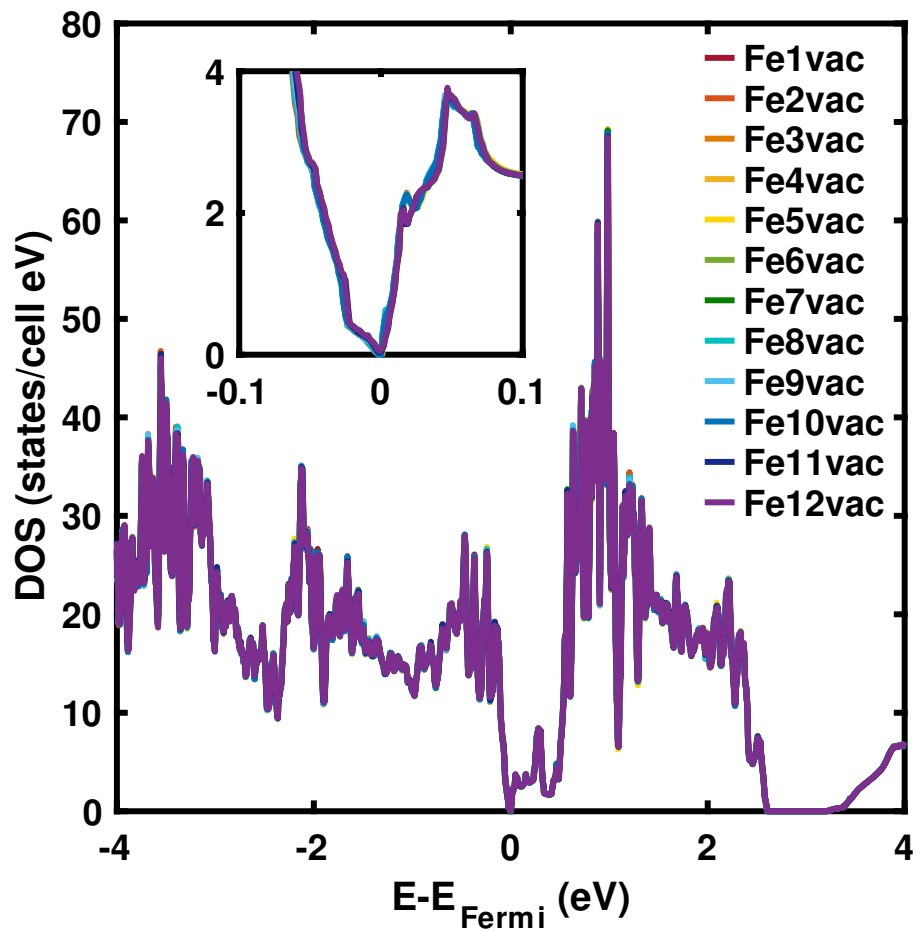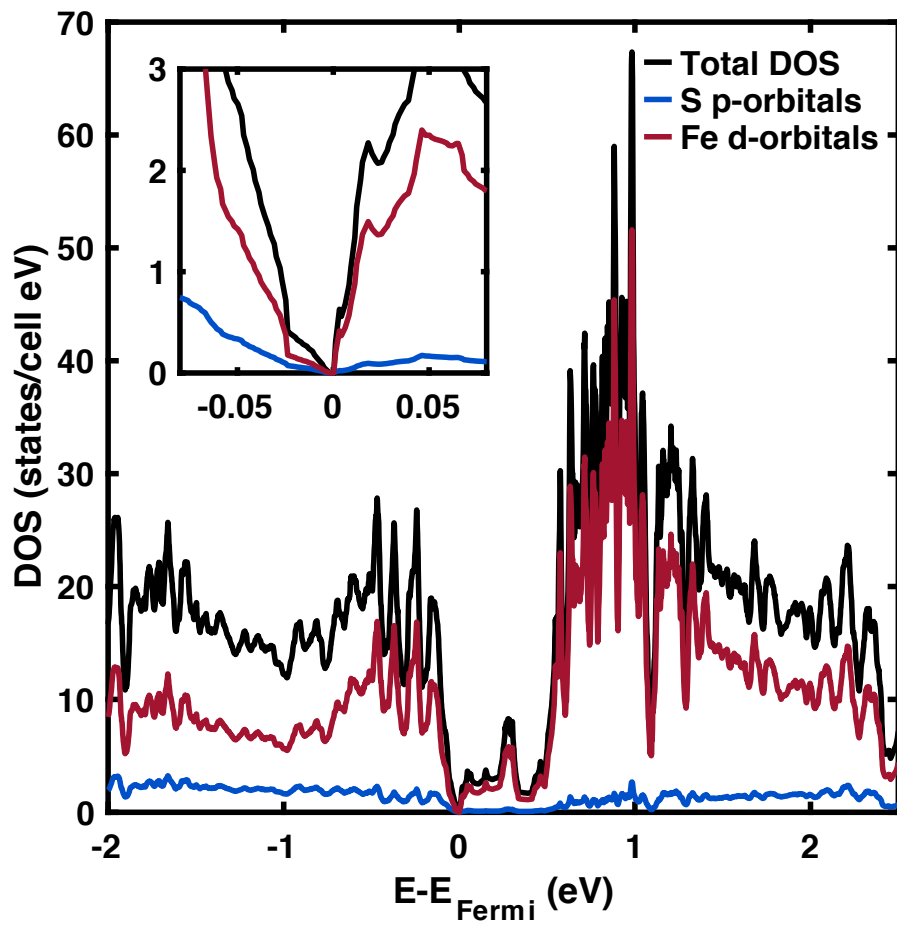
Figure 3.8: Projected density of states of iron deficient troilite. The Fe d-orbitals make up the majority of both valence and conduction bands with the S p-orbitals only contributing a small amount. All other orbitals not shown in the figure contribute insignificantly to the total DOS.

of pyrrhotite-4M. As shown in Fig. 3.4(b), the pyrrhotite-4M unit cell is part of the monoclinic space group $C2/c$ with four formula units of Fe_7S_8 in the unit cell. Using the experimental structure from Powell et al. [15] with $U^* = 1.4$ eV, fixing the atomic positions, and initializing in its AFM ground state, the DOS of pyrrhotite-4M is gapless, just like iron deficient troilite. Figure 3.9 shows the DOS of pyrrhotite-4M with $U = 1.4$ eV. Since the band gap increases with increasing U due to the repulsive nature of on-site electrons, we affirm that pyrrhotite-4M remains gapless for any value of $U \leq 1.4$ eV. The DOS of pyrrhotite-4M and iron deficient troilite are both gapless with comparable features, supporting the similarity between the two structures.

3.5.1   Spin-Polarization in Iron Deficient Troilite
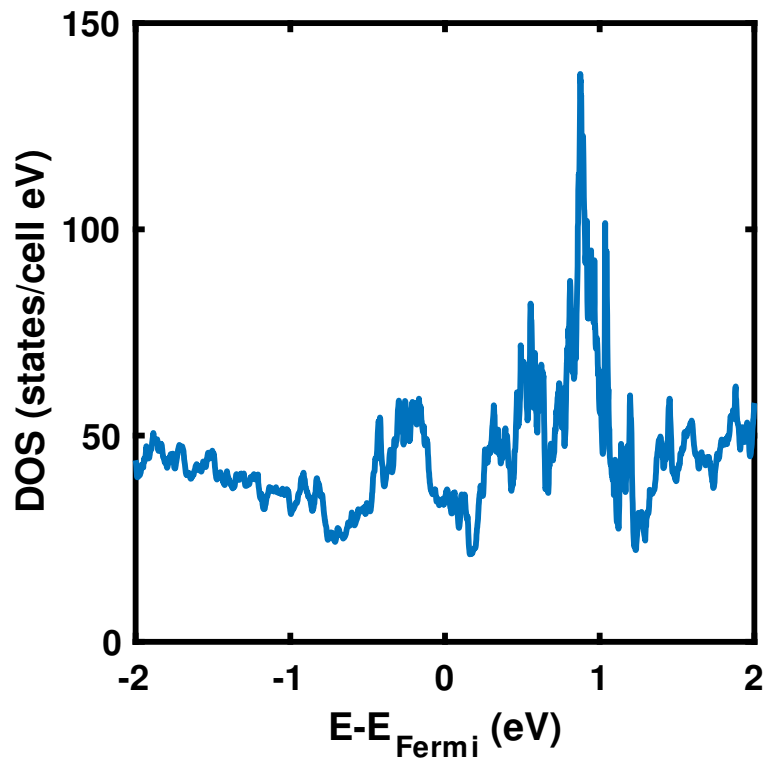
We can describe the magnetic interactions of electrons in condensed matter systems quite simply with the Hubbard model:

$$H = \sum_{i,j,\sigma} t_{ij} c_{i\sigma}^{\dagger} c_{j\sigma} + \sum_{i} U n_{i\uparrow} n_{i\downarrow} \tag{3.3}$$

where t_{ij} is the tight-binding hopping amplitude between sites i and j, $c_{i\sigma}^{\dagger}$ and $c_{i\sigma}$ are the creation and annihilation operators, $n_{i\sigma} = c_{i\sigma}^{\dagger} c_{i\sigma}$ is the local density of electrons with spin σ, where $\sigma = \uparrow$ or $\downarrow$, and U is the value of the on-site Coulomb repulsion. U adds an energetic penalty whenever two electrons with opposite spins occupy the same site, which acts the same as the U that we use for our DFT+U calculations, adding strong correlation and localizing electrons onto sites. Systems with large U are called strongly correlated. In the second term of the Hubbard model, we exclude the case of electrons with the same spin since it is not permitted by the Pauli exclusion principle. For a positive nonzero value of U, the states split from their initial degenerate form.

In the defect-free troilite unit cell, the number of spin up and spin down magnetic moments are equal, resulting in a total magnetic moment of zero. But the introduction of a vacancy defect introduces a magnetically frustrated state that cannot assume the fully ordered structure displayed

Figure 3.9: DOS of Pyrrhotite-4M with $U = 1.4$ eV. Since the band gap increases as U increases, we know that pyrrhotite-4M remains gapless across a wide range of U values.
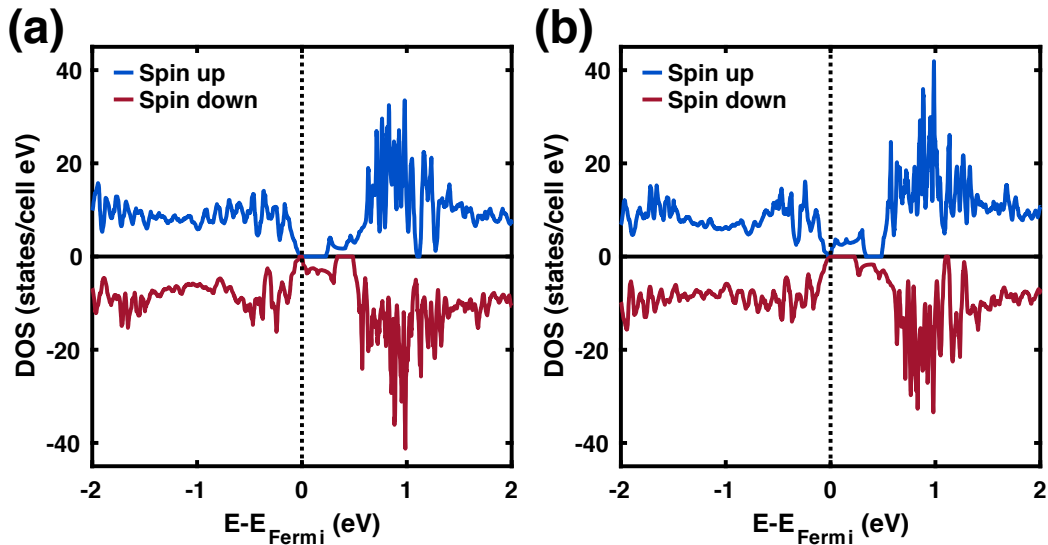
in Figure 3.4. This results in a potential energy splitting between spin up and spin down bands that were degenerate in defect-free cases. Figure 3.10 shows the spin-polarized DOS for Fe vacant troilite where the Fe removed either has a positive or negative magnetic moment. In both cases, electrons of one spin remain ungapped while the other obtains a band gap of 0.23 eV. The spin up electrons become insulating with the removal of a Fe atom with a negative magnetic moment while the spin down electrons become insulating with the removal of a Fe atom with a positive magnetic moment. This unusual electronic structure where one electron spin is gapless while the opposite spin exhibits a band gap is called a half metal [85]. Half metals are fairly uncommon and exhibit interesting magnetic and electronic properties. Examples of half metals include CrO_2, NiMnSb, and PtMnSb [85, 86, 87]. In our system, the gapless spin channel actually goes to zero at the Fermi energy, so it is better classified as a spin gapless semiconductor. These materials, for example $PbPdO_2$, have easily tunable excited charged carriers that can be 100% spin polarized, which present new applications for spintronics, electronics, and optics [88]. Although our version of iron-deficient troilite shows spin gapless semiconductor properties, we cannot guarantee that the experimental structure shares this magnetic structure since our iron deficient troilite does not share the crystal structure of any known pyrrhotite. This however is an interesting prediction with potential applications in spintronics that could be tested experimentally on pyrrhotites in the future.

3.6   Troilite's Phonon Modes

Using both Density Functional Perturbation Theory (DFPT) from VASP and the finite difference method (using the harmonic approximation) from the phonopy code, we can identify and assign the frequency and symmetry to all the phonon modes in troilite. Both methods calculate the Hessian matrix, the matrix of the interatomic force constants, which in turn is used to calculate the phonon modes. Due to the non-symmetric nature of iron deficient troilite, we cannot assign the symmetries to its phonon modes, so we only perform the calculation with defect-free troilite. This is the first study, to our knowledge, that the phonon modes of troilite have ever been characterized.

Figure 3.10: Spin-polarized DOS of a) Fe2vac and b) Fe6vac unit cells. Both structures show spin gapless semiconducting behavior, where the insulating spin channels depend on the sign of the magnetic moment of the Fe removed. For $\mu_B < 0$ on the removed Fe atom, the spin electrons become insulating with a band gap of 0.23 eV as shown in panel a), while the removal of a Fe atom with $\mu_B > 0$ causes the spin down electrons to develop a band gap of 0.23 eV as shown in panel b). All Fe vacancies in troilite produce a spin-polarized DOS matching panel a) or b) depending on whether the vacant Fe had a positive or negative magnetic moment.

The Raman-active phonon modes of troilite tell us about the long-range crystallinity of the material and can be used to characterize the material in an experimental spectrum.

DFPT calculates the Hessian matrix by using the electron density linear response to a perturbation within density functional theory. We will briefly describe the procedure here, following the formalism of Baroni et al. [89]. We assume the that the external potential acting on the electrons is a differentiable function of a set of parameters, $\lambda \equiv \{\lambda_i\}$, where $\lambda_i = \mathbf{R}_I$ for lattice dynamics. The first and second derivatives of the ground state energy are:

$$\frac{\partial E}{\partial \lambda_i} = \int d\mathbf{r} \frac{\partial V_\lambda(\mathbf{r})}{\partial \lambda_i} n_\lambda(\mathbf{r}) \tag{3.4}$$

$$\frac{\partial^2 E}{\partial \lambda_i \partial \lambda_j} = \int d\mathbf{r} \frac{\partial^2 V_\lambda(\mathbf{r})}{\partial \lambda_i \partial \lambda_j} n_\lambda(\mathbf{r}) + \int d\mathbf{r} \frac{\partial n_\lambda(\mathbf{r})}{\partial \lambda_i} \frac{\partial V_\lambda(\mathbf{r})}{\partial \lambda_j} \tag{3.5}$$

In Equation 3.5, electron linear response term is $\frac{\partial n_\lambda(\mathbf{r})}{\partial \lambda_i}$ and can be evaluated by linearizing the Kohn-Sham Equations listed in Chapter 2 of this thesis. First we linearize the electron density:

$$\Delta^\lambda n(\mathbf{r}) = 4Re \sum_j \psi_j^*(\mathbf{r}) \Delta^\lambda \psi_j(\mathbf{r}) \tag{3.6}$$

where the finite-difference operator Δ^λ is defined as:

$$\Delta^\lambda F = \sum_i \frac{\partial F_\lambda}{\partial \lambda_i} \Delta \lambda_i \tag{3.7}$$

Now we obtain the variational Kohn-Sham orbitals, $\Delta^\lambda \psi_j(\mathbf{r})$, by first-order perturbation theory of the Kohn-Sham orbitals:

$$(H_{SCF} - \epsilon_j) \Delta^\lambda \psi_j(\mathbf{r}) = - \left(\Delta^\lambda V_{SCF} - \Delta^\lambda \epsilon_j \right) \psi_j(\mathbf{r}) \tag{3.8}$$

where H_{SCF} is the unperturbed Kohn-Sham Hamiltonian and V_{SCF} is the potential energy encompassing the external potential and exchange-correlation potential:

$$H_{SCF} = -\frac{\hbar^2\nabla^2}{2m} + V_{SCF}(\mathbf{r}) = -\frac{\hbar^2\nabla^2}{2m} + V_{ext}(\mathbf{r}) + e^2 \int \frac{n(\mathbf{r}')}{|\mathbf{r}-\mathbf{r}'|}d\mathbf{r} + V_{xc}(\mathbf{r};[n(\mathbf{r})]) \qquad (3.9)$$

The variation of $V_{SCF}(\mathbf{r})$ in Equation 3.8 is given by:

$$\Delta^\lambda V_{SCF}(\mathbf{r}) = \Delta^\lambda V_{ext}(\mathbf{r}) + e^2 \int d\mathbf{r}\frac{\Delta^\lambda n(\mathbf{r}')}{|\mathbf{r}-\mathbf{r}'|} + \frac{dV_{xc}(n)}{dn}\big|_{n=n(\mathbf{r})} \Delta^\lambda n(\mathbf{r}) \qquad (3.10)$$

Equations 3.6-3.10 form a set of self-consistent equations for the perturbed system analogous to the Kohn-Sham equations listed in Chapter 2. We can solve these self consistently in the normal DFT manner to obtain the Hessian matrix which is used in calculation of the phonon modes.

The phonopy code uses the finite difference method under the harmonic approximation to calculate the Hessian [90]. The program generates a set of supercells containing small atom displacements given a unit cell as input. Using DFT, we determine the forces on the atoms of each supercell with a fixed ion calculation. The overall force constants are given by Φ:

$$\Phi_{ij}(M_\mu, N_\nu) = \frac{\partial V^2}{\partial u_i(M_\mu)\partial u_j(N_\nu)} \simeq -\frac{F_i(M_\mu)}{u_j(N_\nu)} \qquad (3.11)$$

Where M, N are lattice point indices, μ, ν point to the index of the atom within the unit cell, ∂u_i is the displacement of the atom, and F_i is the force on the atom. Once the forces on the set of displacement supercells are calculated, the program collects them to create the Hessian matrix to calculate the phonon modes.

Troilite is part of the *P-62c* space group, which is in the D_{3h} point group. The character table for the D_{3h} point group, shown in Table 3.5, lists the possible symmetries of any phonon mode depending on how it acts under the listed transformations based on group theory. The phonon modes that transform as products of x, y, or z are Raman-active since they result in a change in the polarizability of the solid. For the D_{3h} point group, modes with symmetries A'$_1$, E', and E" are Raman-active.

For any crystal, the number of phonon modes corresponds equals the vibrational degrees of freedom of the crystal. Each atom has 3 vibrational degrees in freedom, so a unit cell will produce

Table 3.5: Character table for the D_{3h} point group. The phonon modes with A'$_1$, E', or E"
symmetries are Raman-active since they transform as products of x, y, or z. These transformations
result in a change in polarizability of the solid, which is required for the mode to be Raman-active.
The phonon modes with A"$_2$ or E' symmetries are IR-active since they transform as x, y, or z,
which indicates a change in dipole moment.

Symmetry	E	$2C_3$	$3C'_2$	σ_h	$2S_3$	$3\sigma_v$	linear	quadratic
A'$_1$	1	1	1	1	1	1	$-$	x^2+y^2,z^2
A'$_2$	1	1	-1	1	1	-1	R_z	$-$
E'	2	-1	0	2	-1	0	(x,y)	$(x^2\text{-}y^2,xy)$
A"$_1$	1	1	1	-1	-1	-1	$-$	$-$
A"$_2$	1	1	1	-1	-1	-1	z	$-$
E"	2	-1	0	-2	1	0	(R_x,R_y)	(xz,yz)

$3N$ phonon modes, where N is the number of atoms in the unit cell. Our troilite unit cell contains 24 atoms, so it will have 72 vibrational degrees of freedom, and hence 72 total calculated phonon modes. Only some of these modes will be Raman-active, and considering that some phonon modes will be degenerate, we will likely see fewer peaks in the experimental Raman spectra of troilite. Using the Bilbao Crystallographic Server [91], we calculated the Raman-active symmetry adapted modes at the Γ point ($\mathbf{k} = (0,0,0)$) based on troilite's crystal structure, shown in Table 3.6. These results show that there are 30 expected Raman-active modes in troilite.

Table 3.6: Allowed Raman-active modes for troilite based for the Γ point based on its crystal symmetry. We expect to see 30 Raman-active modes in defect-free troilite.

Atom: WP	A'$_1$	A'$_2$	A"$_1$	A"$_2$	E'	E"
Fe: 12i	3	–	–	–	6	6
S: 2a	–	–	–	–	1	1
S: 4f	1	–	–	–	2	2
S: 6h	2	–	–	–	4	2

Both methods of calculating phonon modes (DFPT and finite difference) should yield the same results, so for consistency I compared the DFPT calculated phonon modes to the phonon modes calculated with the finite difference method. Both calculations produced phonon modes that agree to within 0.1 cm^{-1} (0.1%) of each other, which provides good agreement between the methods. Table 3.7 lists all the phonon modes of troilite and their degeneracies for $U = 1.4$ eV, with the Raman-active modes listed in bold. There are 30 Raman-active frequencies, which matches the allowed Raman-active modes in Table 3.6. Figure 3.11 shows the density of states of all phonon modes, while Figures 3.12–3.15 show the motion of each phonon mode with arrows pointing in the direction of each atom's movement. As noted in Table 3.7, the first three modes correspond to translations of the material, and hence have frequencies around 0 cm^{-1}.

Table 3.7: All Phonon modes and degeneracies for troilite where $U = 1.4$ eV. The Raman-active modes are listed in bold. The first three modes correspond to translations of the unit cell, which is why they are so close to 0 cm^{-1}. Our system is well converged since there are no other negative frequencies.

Mode	Symmetry	Frequency (cm^{-1})	Degeneracy	Mode	Symmetry	Frequency (cm^{-1})	Degeneracy
1, 2	**E'**	**-0.13342**	**2**	37	A'$_2$	184.02731	1
3	A"$_2$	0.03335	1	38	A"$_2$	188.83063	1
4, 5	**E"**	**38.52665**	**2**	39, 40	**E'**	**205.37541**	**2**
6, 7	**E'**	**68.14714**	**2**	41, 42	**E"**	**207.04323**	**2**
8, 9	**E"**	**80.28887**	**2**	43, 44	**E'**	**248.33847**	**2**
10	A'$_2$	108.94203	1	45, 46	**E'**	**251.07369**	**2**
11, 12	**E"**	**111.04348**	**2**	47, 48	**E"**	**268.25224**	**2**
13, 14	**E'**	**127.68833**	**2**	49, 50	**E"**	**273.65598**	**2**
15	**A'$_1$**	**132.29152**	**1**	51	**A'$_1$**	**275.79079**	**1**
16, 17	**E"**	**135.12681**	**2**	52, 53	**E'**	**279.69349**	**2**
18	A'$_2$	136.19422	1	54	A'$_2$	286.99855	1
19	A"$_2$	138.46245	1	55	A'$_2$	289.83384	1
20	**A'$_1$**	**139.89678**	**1**	56	A"$_1$	293.2362	1
21	A"$_1$	140.93083	1	57, 58	**E'**	**297.33903**	**2**
22, 23	**E'**	**142.46522**	**2**	59, 60	**E"**	**304.04367**	**2**
24	A"$_1$	145.63408	1	61	A"$_2$	306.0117	1
25, 26	**E'**	**148.20252**	**2**	62, 63	**E'**	**306.97904**	**2**
27	A'$_2$	156.34149	1	64	**A'$_1$**	**308.6135**	**1**
28, 29	**E'**	**156.97526**	**2**	65, 66	**E'**	**312.21599**	**2**
30, 31	**E"**	**159.71049**	**2**	67, 68	**E"**	**316.6524**	**2**
32	A"$_2$	169.85083	1	69	**A'$_1$**	**325.92548**	**1**
33, 34	**E"**	**172.41928**	**2**	70	A"$_1$	337.43344	1
35	A"$_1$	174.28724	1	71	A"$_2$	338.16728	1
36	**A'$_1$**	**181.49222**	**1**	72	A'$_2$	353.91151	1

Figure 3.11: Phonon density of states of defect-free troilite with $U = 1.4$ eV.
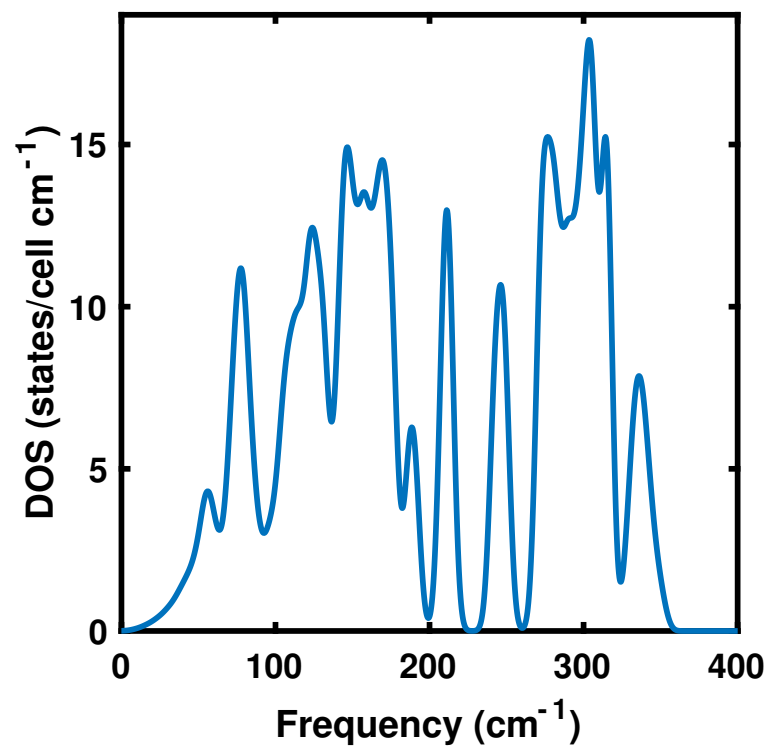
Figure 3.12: Phonon modes 1-20 of troilite. Fe and S atoms are labeled red and yellow, respectively, and the blue arrows indicate the relative amplitude and direction of the atom's movement.
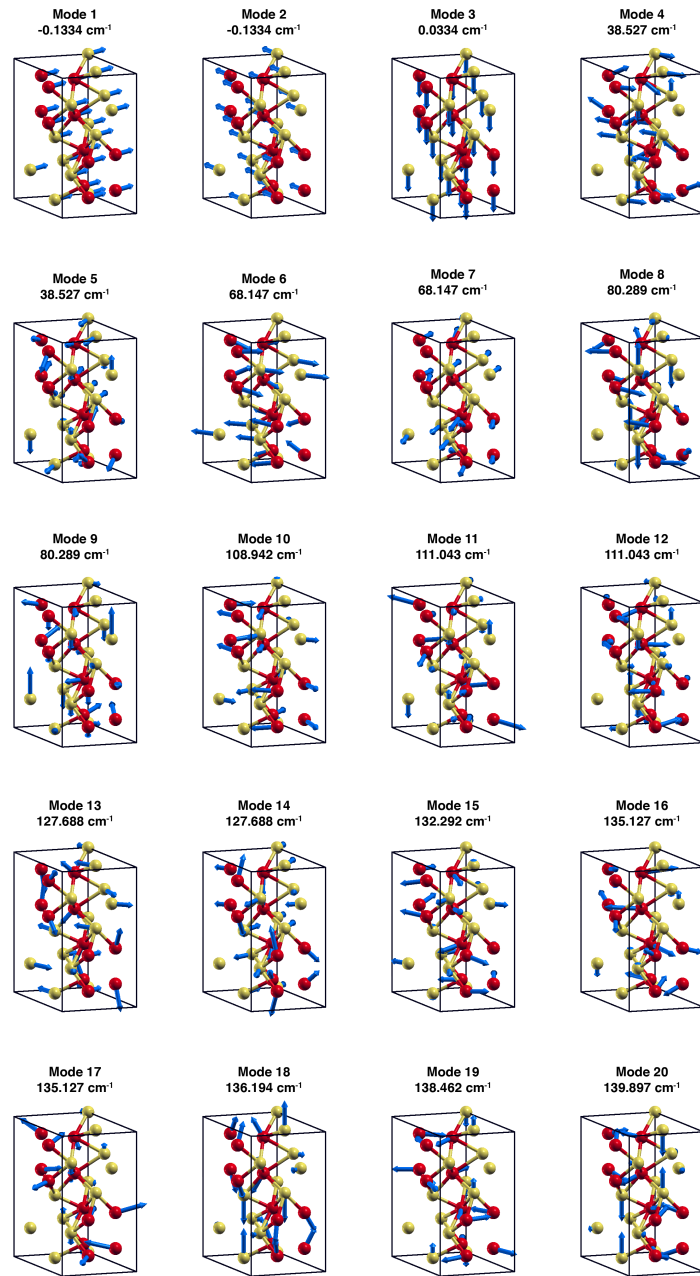
Figure 3.13: Phonon modes 21-40 of troilite. Fe and S atoms are labeled red and yellow, respectively, and the blue arrows indicate the relative amplitude and direction of the atom's movement.


Mode 21
140.931 cm⁻¹

Mode 22
142.465 cm⁻¹

Mode 23
142.465 cm⁻¹

Mode 24
145.634 cm⁻¹

Mode 25
148.203 cm⁻¹

Mode 26
148.203 cm⁻¹

Mode 27
156.341 cm⁻¹

Mode 28
156.975 cm⁻¹

Mode 29
156.975 cm⁻¹

Mode 30
159.710 cm⁻¹

Mode 31
159.710 cm⁻¹

Mode 32
169.851 cm⁻¹

Mode 33
172.419 cm⁻¹

Mode 34
172.419 cm⁻¹

Mode 35
174.287 cm⁻¹

Mode 36
181.492 cm⁻¹

Mode 37
184.027 cm⁻¹

Mode 38
188.831 cm⁻¹

Mode 39
205.375 cm⁻¹

Mode 40
205.375 cm⁻¹
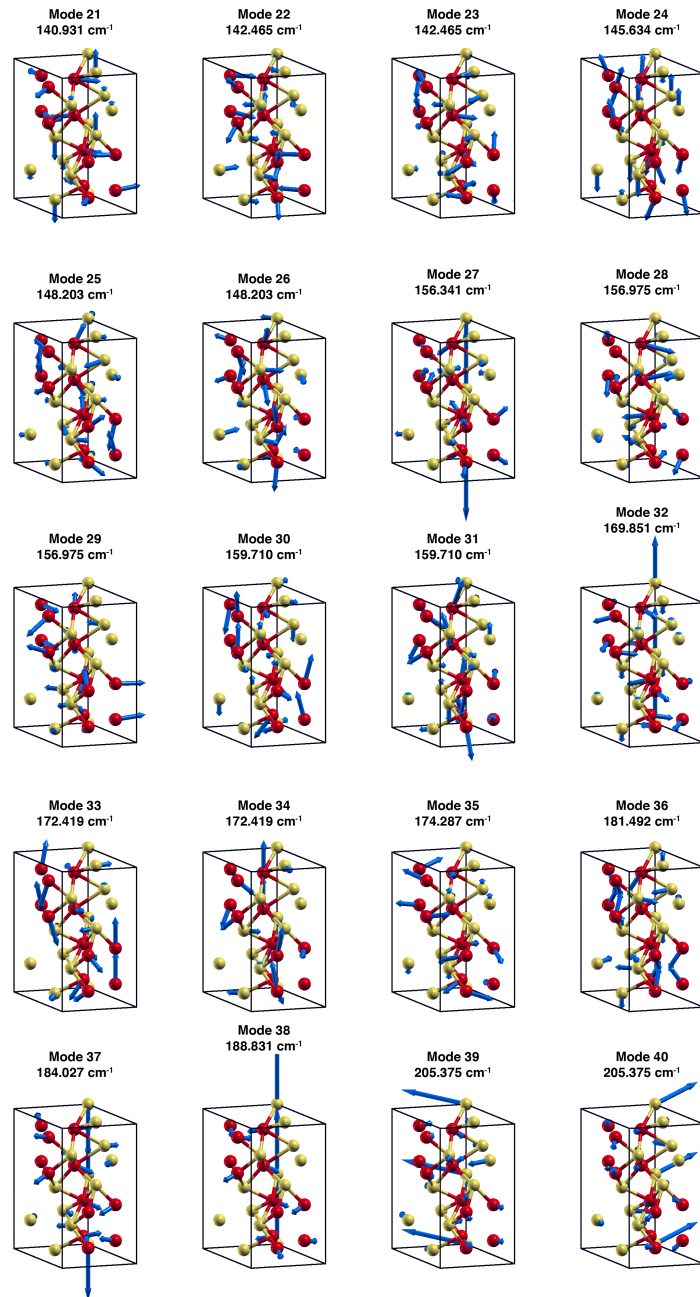
Figure 3.14: Phonon modes 41-60 of troilite. Fe and S atoms are labeled red and yellow, respectively, and the blue arrows indicate the relative amplitude and direction of the atom's movement.
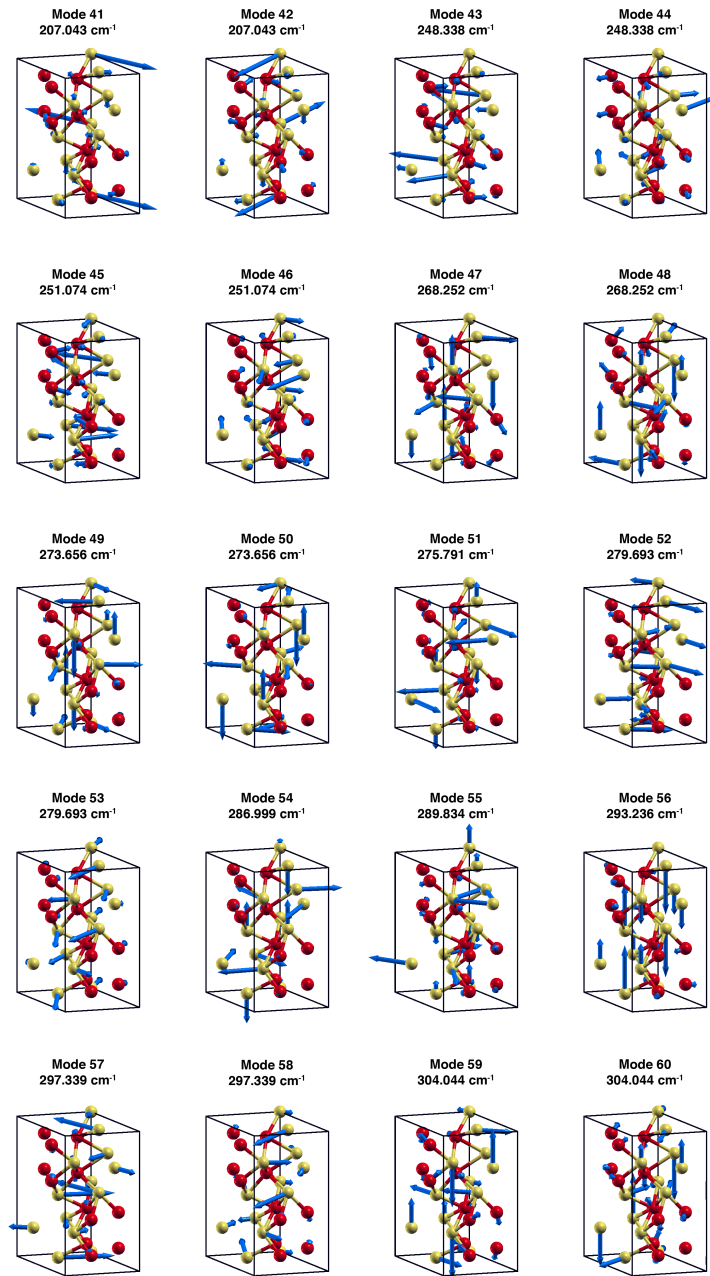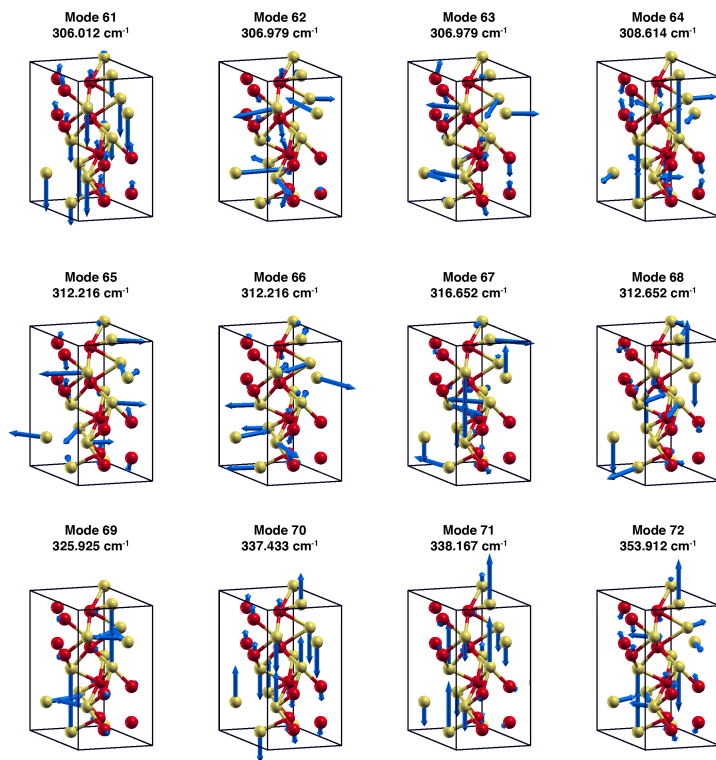
Figure 3.15: Phonon modes 61-72 of troilite. Fe and S atoms are labeled red and yellow, respectively, and the blue arrows indicate the relative amplitude and direction of the atom's movement.

3.7   Conclusion

In this chapter, we showed the role that Fe defects have on troilite and predict that any Fe vacancy introduced into the stoichiometric end member changes the unit cell, transforming the hexagonal crystal structure of troilite into a monoclinic structure that is present in a number of pyrrhotite structures. Our calculations also predict that small concentrations of iron defects erase the band gap in troilite by introducing midgap defect states in an already narrow gap. It is possible, or even likely, that the crystal structures reported for experimental troilite samples in fact more closely resemble these defective structures. The novel spin gapless semiconductor property that iron deficient exhibits may create new applications for the material and poses an area for future research.

Chapter 4

Sulfur Deficient Pyrite

4.1   Introduction

Even though decades of experimental results support the sulfur-deficient stoichiometry of pyrite and its oversized impacts on the optical, electronic, and magnetic properties of the material, the computational characterization of these defects remains largely undiscovered [67, 92, 93, 27, 26, 41, 78]. Most computational studies examine the vacancies on pyrite's surface and only two papers that we know of address the electronic properties of bulk sulfur vacancies [26, 27]. Bulk vacancies are important in determining the properties of iron sulfides [94], and we seek to gain a more complete understanding of their effects on pyrite's electronic structure.

In this chapter, we calculate and characterize the defect states created by a neutral S vacancy, which more closely models experimentally relevant pyrite. Using DFT, we see the emergence of four defect states and a narrowing of the band gap. These spatially localized defect states are composed of both iron d-orbitals and sulfur sp^3 orbitals and surround the sulfur vacancy. In order to obtain a clearer picture of the magnetic structure of sulfur deficient pyrite, we use crystal field theory to look at the splitting of the Fe d-orbitals, the sole contributors to pyrite's magnetism. By transforming the delocalized Bloch states generated through DFT into maximally localized Wannier functions (MLWFs), we can directly calculate the crystal field splitting. This is the first time the crystal field splitting has ever been directly calculated for pyrite. In this new diabatic picture, the crystal field splitting decreases by a factor of two the the presence of a sulfur defect. The degeneracies of the Fe d-orbitals lift, creating the possibility of spin splitting and a spin crossover and resulting in

magnetic ordering.

4.2   DFT Methods

We performed all pyrite DFT calculations on a 2x2x2 pyrite supercell comprised of 32 formula units. The cubic unit cell of pyrite resides in the $Pa3$ space group where Fe and S occupy the 4a and 8c Wyckoff positions, respectively. The 4a Wyckoff position contains the four crystal coordinates (0,0,0), (1/2,0,1/2), (0,1/2,1/2), and (1/2,1/2,0), while the 8c position refers to the eight crystal coordinates (x,x,x), (-x+1/2,-x,x+1/2), (-x,x+1/2,-x+1/2), (x+1/2,-x+1/2,-x), (-x,-x,-x), (x+1/2,x,-x+1/2), (x,-x+1/2,x+1/2), and (-x+1/2,x+1/2,x), where x is a positional parameter. Starting with the experimental FeS_2 crystal structure of Bayliss [95], where the unit cell lattice parameter and sulfurs positional parameter are given by a = 5.4166 and x = 0.3851, respectively, we used the conjugate gradient method to move atomic positions and unit cell dimensions at constant pressure until the forces in each self-consistent cycle were less than 1 meV/Å.

Since pyrite contains strongly correlated Fe d-electrons, we use the DFT+U scheme described in the methods section. We set $U = 2$ eV because this value is widely accepted in the literature for giving accurate results for pyrite [67, 78, 66, 26]. For the DFT exchange-correlation functional, we used the Perdew Burke-Ernzerhof (PBE) form of the generalized gradient approximation (GGA) since it calculates parameters matching well with experimental pyrite [96, 97, 98, 74]. We also used projector augmented-wave (PAW) pseudo-potentials containing 6 valence electrons and 16 valence electrons for each sulfur and iron atom, respectively [74, 75]. Our choice of harder pseudo-potentials improves the accuracy of the calculation since these pseudo-potentials contain more electrons and require larger basis sets. For our system, we determined the optimal plane wave energy cutoff to be 660 eV, which converges the total energy to within 10 meV per unit cell, shown in Figure 4.1. All structures were initialized as nonmagnetic, in accordance with the ground state of defect-free pyrite [47, 99, 45, 100]. The wave vector spacing was based on a 3x3x3 Γ-centered Monkhorst-pack grid for relaxation and a 9x9x9 grid for electronic density of states (DOS) calculations [101]. These k-point grids ensured energy convergence and equal sampling in all directions of the Brillouin zone.

All energies were converged to within $1\text{x}10^{-8}$ eV in each self-consistency cycle. We additionally used Gaussian smearing with a width of 0.01 eV for geometry relaxations and the tetrahedron method with Blöchl corrections for DOS and total energy calculations [102]. For sulfur deficient calculations, we started with the fully relaxed non-defective supercell and removed a single neutral S atom, resulting in a 1/64 or 1.56% S vacancy. All other DFT parameters were kept the same as the defect-free case, and we looked at the results of both fixing the nuclear coordinates and letting the ions relax in the presence of the sulfur vacancy.

4.3   Defect-Free Pyrite

After relaxing defect-free pyrite, we obtained a super cell with lattice parameter a = 10.8543 Å, which is within 0.2% of our collaborator's experimental pyrite particles and matches previously calculated defect-free pyrite structures [103, 27, 97, 67]. Figure 4.2 shows the band structure and total electronic density of states (DOS) of defect-free pyrite. We calculated a 0.92 eV band gap for defect-free pyrite,00000 with a massive valence band and a relatively massless conduction band edge that dips down at the Γ point. The band gap is indirect, involving a transition from near the X point to the Γ point in k-space. The projected density of states, shown in Figure 4.3, reveals that Fe d-orbitals constitute the vast majority of the valence band, while S p-orbitals make up the majority of the valence band edge, but only right at the conduction band minimum. Our calculated band gap and electronic structure is consistent with other pyrite DFT and GW calculations and agrees well with our collaborator's synthesized pyrite nanoparticle band gap of 0.996 eV [104, 103, 105, 106]. In agreement with the known diamagnetic behavior of pyrite [99], we calculate a nonmagnetic ground state for defect-free pyrite.

Figure 4.4 shows the projected density of states of the Fe d-orbitals in defect-free pyrite. Because the Fe atoms in pyrite are coordinated octahedrally, we expect to see an energy splitting between the e_g (d_{xy}, d_{xz}, d_{yz}) and t_{2g} (d_{z^2}, $d_{x^2-y^2}$) orbitals, which we will discuss in more detail later in this chapter. We see no energy splitting between the t_{2g} and e_g orbitals in Figure 4.4, even though pyrite is experimentally known to have a $t_{2g} - e_g$ gap of approximately 2.0 eV [47, 45, 107,

Figure 4.1: Total energy versus energy cutoff for defect-free Pyrite. We chose to use an energy cutoff of 660 eV for our pyrite calculations, which provides convergence to within 0.001 eV per unit cell.
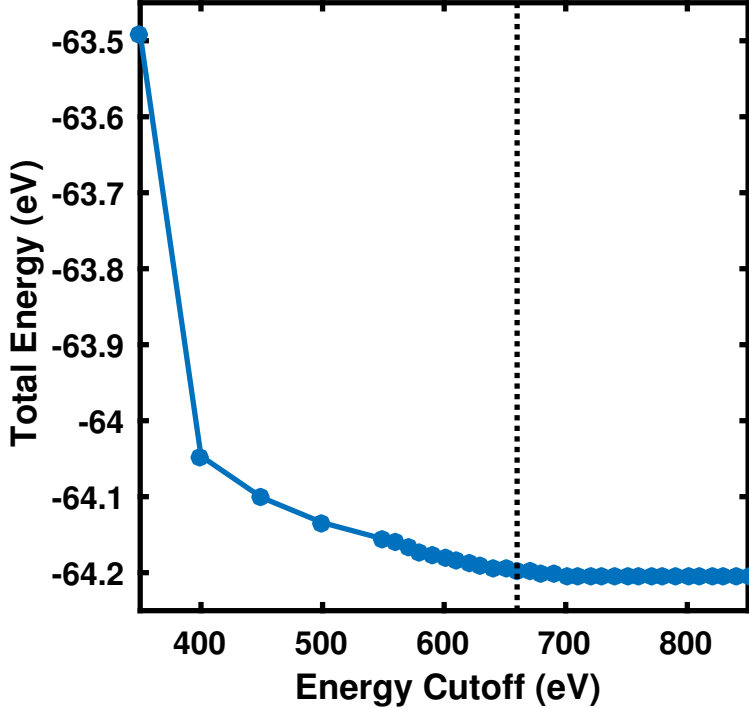

Figure 4.2: Band structure and DOS for defect-free pyrite. The valence band is very massive while the conduction band is quite light. Pyrite has an indirect band gap of 0.92 eV, denoted by the dashed arrow, that involves a transition from near the X point to the Γ point in k-space.
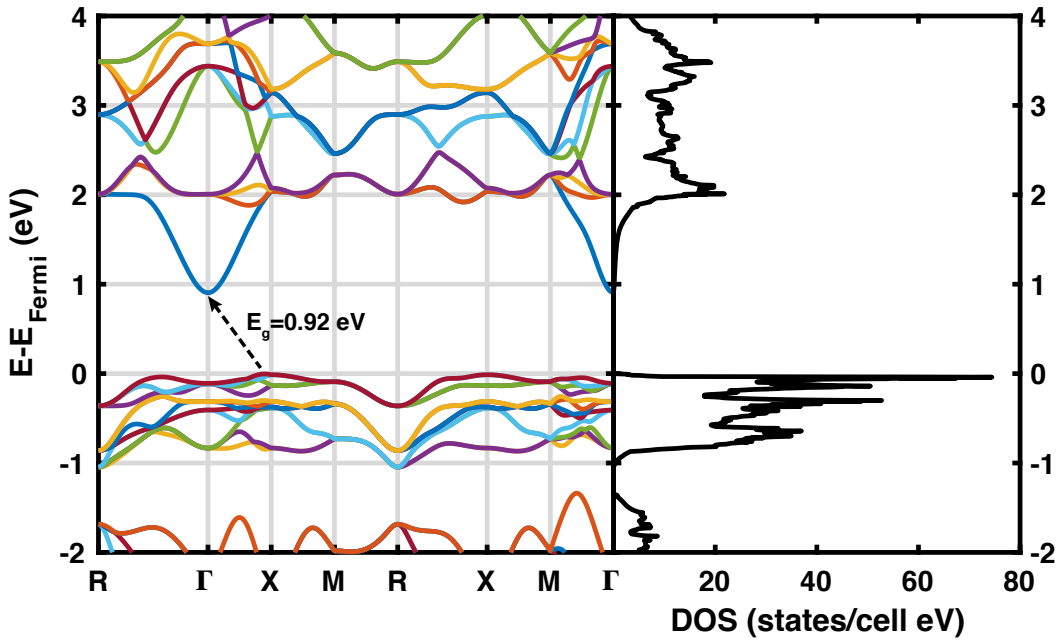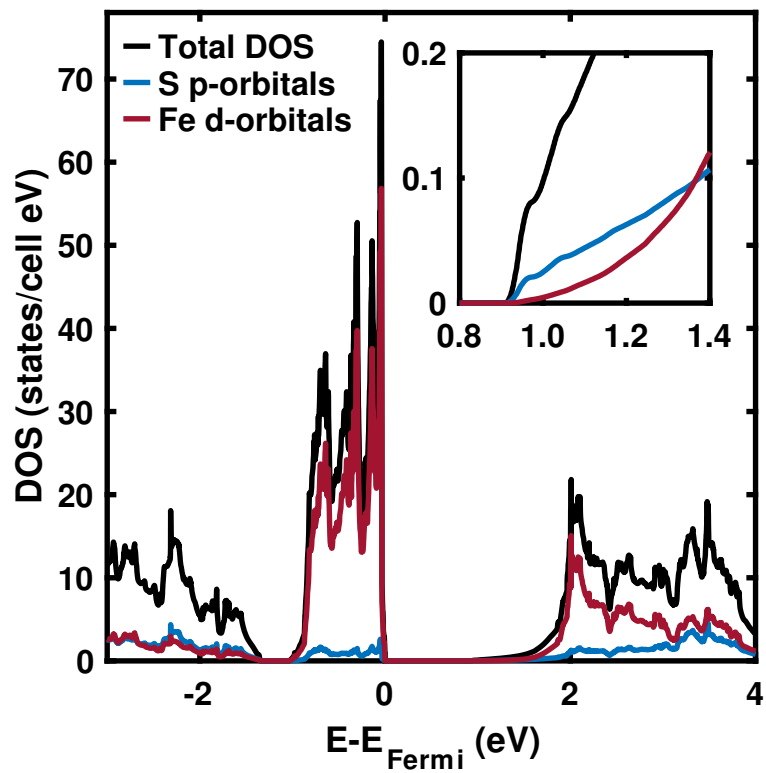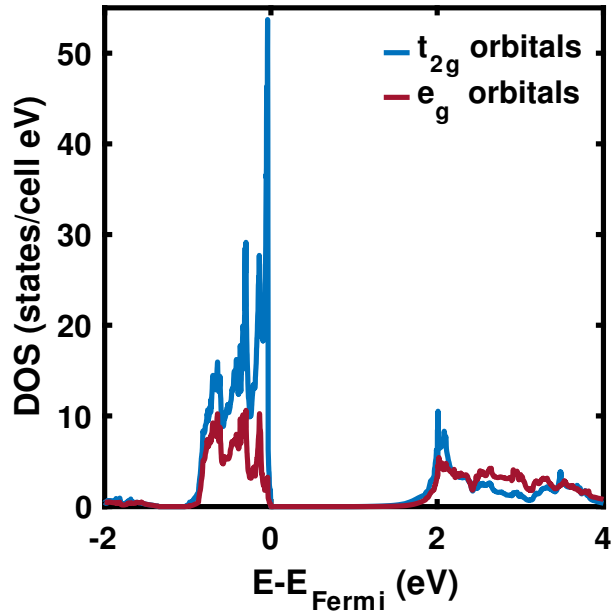
Figure 4.3: Projected density of states for defect-free pyrite. Fe d-orbitals make up the majority of the valence band, while the valence band edge is comprised primarily of S p-orbitals, as shown in the inset.

98, 108, 109, 110]. This discrepancy is rooted in the adiabatic nature of the DFT electronic states; if any nonzero mixing exists between the atomic orbitals, the adiabatic solution to the Schrödinger equation will become delocalized and consist of linear combinations of these atomic orbitals. In order to see any energy splitting between the t_{2g} and e_g orbitals, we must represent the system in a more localized way. We do this by transforming the DFT electronic states into MLWFs, which we describe in detail in Section 4.5.2.

Figure 4.4: Projected density of states of Fe d-orbitals in defect-free pyrite. In this adiabatic solution obtained through DFT, there is no energy splitting between the t_{2g} and e_g orbitals because both have nonzero electron densities at the valence band maximum and conduction band minimum.

4.4 Sulfur-Deficient Pyrite

After removing a neutral sulfur atom from the pyrite supercell, the band gap narrows and we see the emergence of four defect states: an occupied valence band defect, an occupied low midgap state, an unoccupied high midgap state, and an unoccupied conduction band defect state. The energies of these four defect states, and consequently the band gap, are very sensitive to the nuclear coordinates of the solid, revealing strong electron-nuclear coupling in the material. In this section, we look at the effects of both fixing the nuclear positions and allowing them to relax in the

presence of a sulfur vacancy.

4.4.1 Fixed Nuclear Coordinates

We first calculated the electronic structure of a neutral sulfur vacancy where the nuclear coordinates were kept fixed at their defect-free positions, so the unit cell symmetry remained intact. Figure 4.5 shows the comparison of the fixed S deficient DOS with defect-free pyrite. We see a significant decrease in the band gap from 0.92 eV to 0.45 eV and the emergence of the four defect states. Aside from the defect states and shifting of the Fermi energy, the main features of the S-vacant DOS remain the same as the defect-free supercell. Both exhibit a massive valence band that drops off rapidly at the valence band maximum and a slowly rising electron density at the conduction band edge. The band gap also shifts from indirect to direct, now involving a transition to and from the Γ point.

Figure 4.5: DOS comparison of defect-free pyrite with a fixed 1.56% neutral S vacancy. The emergence of four defect states in the electronic structure causes the band gap to decrease from 0.92 eV to 0.45 eV.
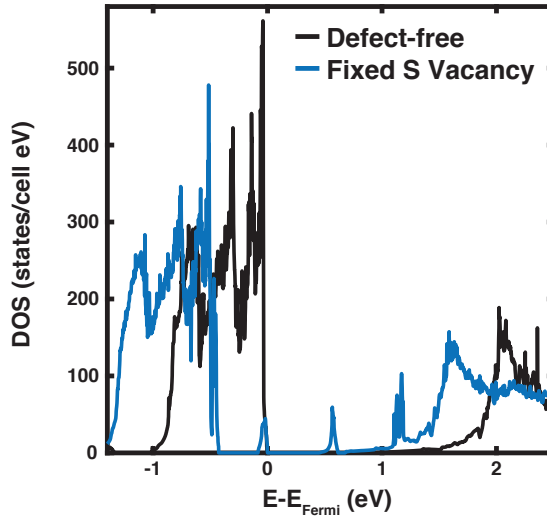

Figure 4.6 shows the band structure of the fixed vacancy supercell along with its DOS. Each defect state is color-coded and remains the same color throughout all figures in this chapter for clarity. The occupied valence band defect, labeled blue, contains contributions from three different

energy bands at what used to be the edge of the valence band before a shifting of the Fermi energy. The occupied low midgap state and unoccupied mid gap state, labeled red and purple, respectively, are each composed of only one energy band and determine the value of the band gap in the solid. Labeled green, the conduction band defect state resides within the conduction band and takes contributions from several energy bands around 1.1 eV above the Fermi energy.

To test if the structural and electronic properties of S-vacant pyrite are insensitive to the position of the S atom vacancy, one would compare the results of removing every S atom individually. Because there are 64 S atoms in our supercell, this becomes computationally expensive. However, we can use symmetry to reduce the number of S atoms we need to sample since our calculations are performed on a supercell. Each pyrite unit cell contains eight unique sulfur positions, so we only need to sample those eight positions because all other sulfur atoms are in equivalent positions in a different subspace of the supercell. Table 4.1 lists the eight unique sulfur positions in a single unit cell with the corresponding equivalent atom numbers in our supercell. We performed calculations for the following sulfur vacancies given by their atom number in the supercell: 1, 3, 10, 15, 21, 27, 28, 39, 44, 52, 56, and 61. Figure 4.7 shows that the electronic structure does remain insensitive to the position of the S vacancy since the DOS of each calculation lies on the same curve.

4.4.2   Relaxed Nuclear Coordinates

Upon relaxing the nuclear coordinates in the presence of a S vacancy, we still see the emergence of four defect states, but with shifted energies. Figure 4.8 compares the calculated DOS of the relaxed S deficient supercell with defect-free pyrite and Figure 4.9 directly compares the energies of these defect states with those of the fixed vacancy. From these two figures, we see that the band gap of the relaxed defective structure is 0.82 eV and its DOS maintains the same overall features as defect-free pyrite, but this band gap is almost twice as large as the band gap of the fixed vacancy structure. Despite the dramatic shift in defect state energies, the nuclear coordinates of the relaxed structure remain largely the same except for the newly under-coordinated S anion that used to exist as a dimer with the now vacant sulfur. All other nuclei move less than 0.07 Å,

Figure 4.6: Band structure and DOS of a fixed sulfur vacancy. The conduction band defect state, labeled blue, is occupied contains contributions from three energy bands. The low midgap state, labeled red, is composed of only one massive energy band and sets the Fermi energy since it is the highest occupied state. Labeled purple, the high midgap state is also composed of one energy band that has a smaller effective mass than the low midgap state. It is unoccupied and determines the the material's band gap. The conduction band defect, labeled green, is composed of multiple energy bands around 1.1 eV above the Fermi energy.
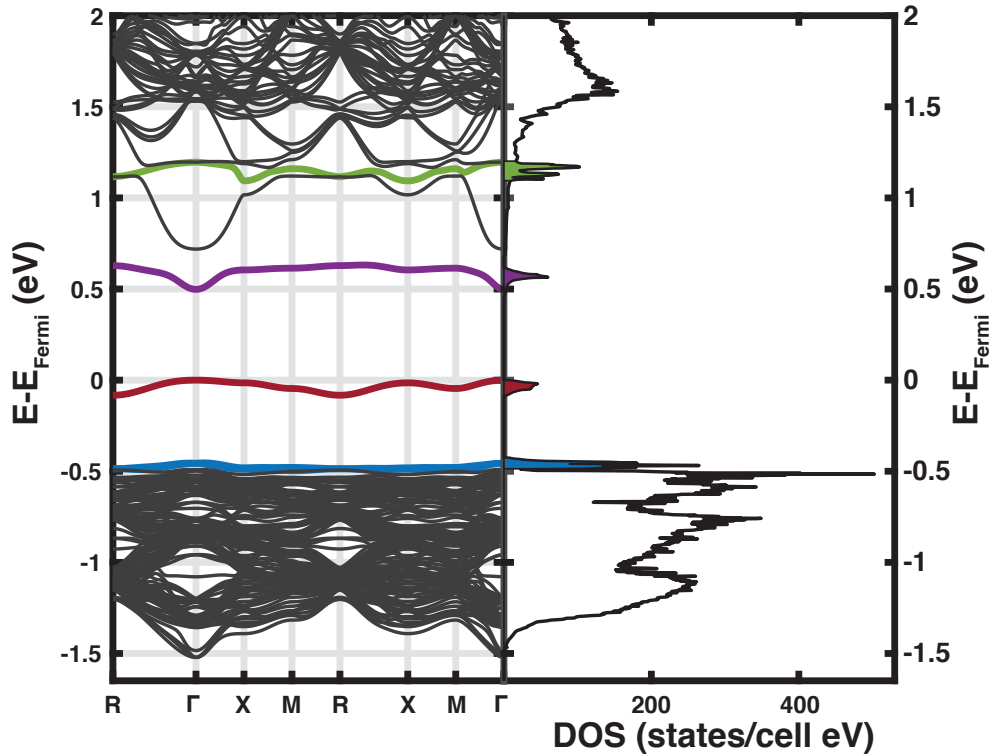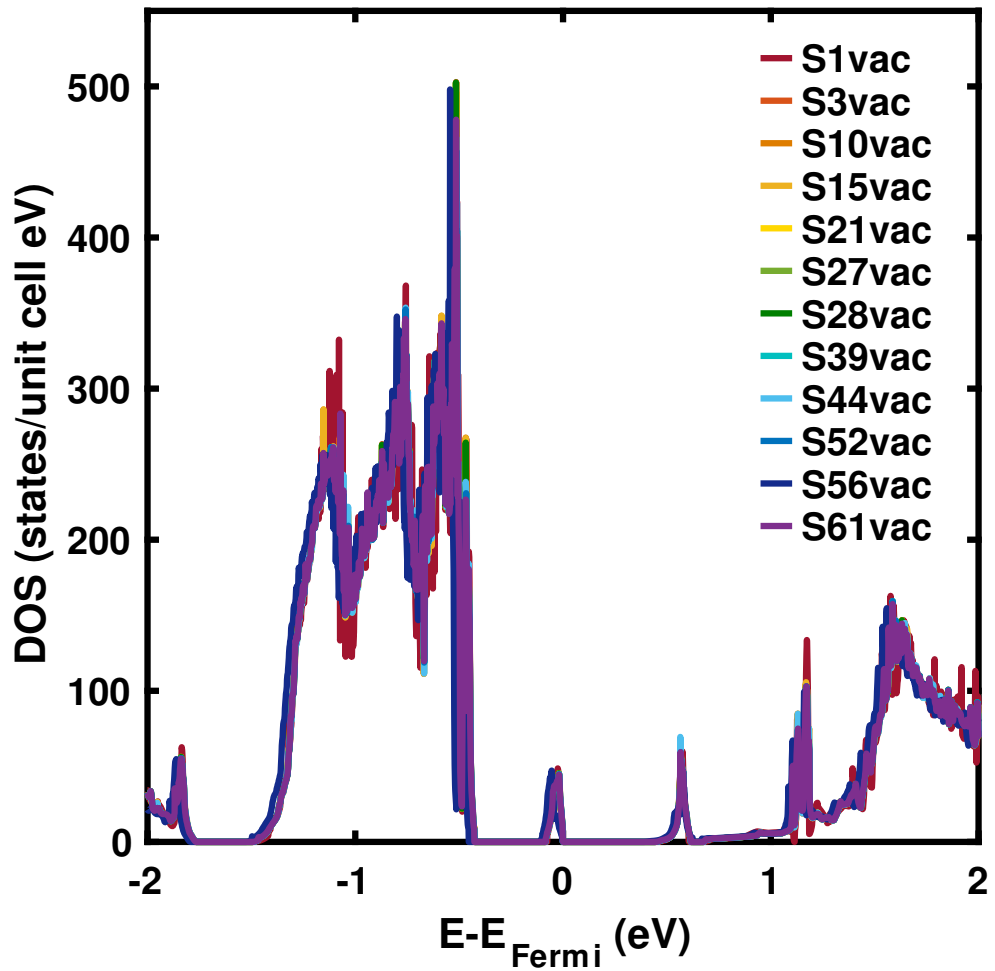
Table 4.1: Unique sulfur positions in the single pyrite unit cell relating to a 2x2x2 supercell. Each S position in the unit cell corresponds to eight equivalent positions in the supercell due its symmetry.
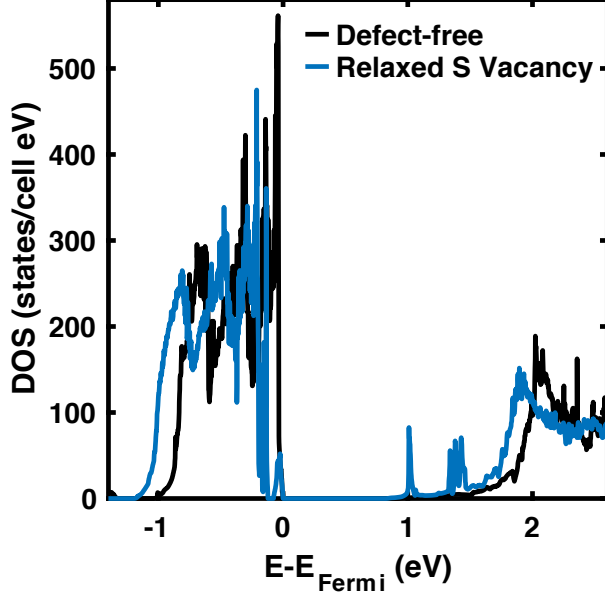
	Unit cell position (crystal coords)			
Label	x	y	z	Atom #'s in Supercell
S1	0.3851	0.3851	0.3851	1-8
S2	0.1149	0.6149	0.8851	9-16
S3	0.6149	0.8851	0.1149	17-24
S4	0.8851	0.1149	0.6149	25-32
S5	0.6149	0.6149	0.6149	33-40
S6	0.8851	0.3851	0.1149	41-48
S7	0.3851	0.1149	0.8851	49-56
S8	0.1149	0.8851	0.3851	57-64

Figure 4.7: DOS comparison of 12 different fixed S vacancy positions, labeled by the vacant S atom number. The DOS of all listed vacancy positions lie on the same curve.

while this under-coordinated S moves more than 0.3 Åinto an interstitial site to partially fill the

hole caused by the S vacancy.
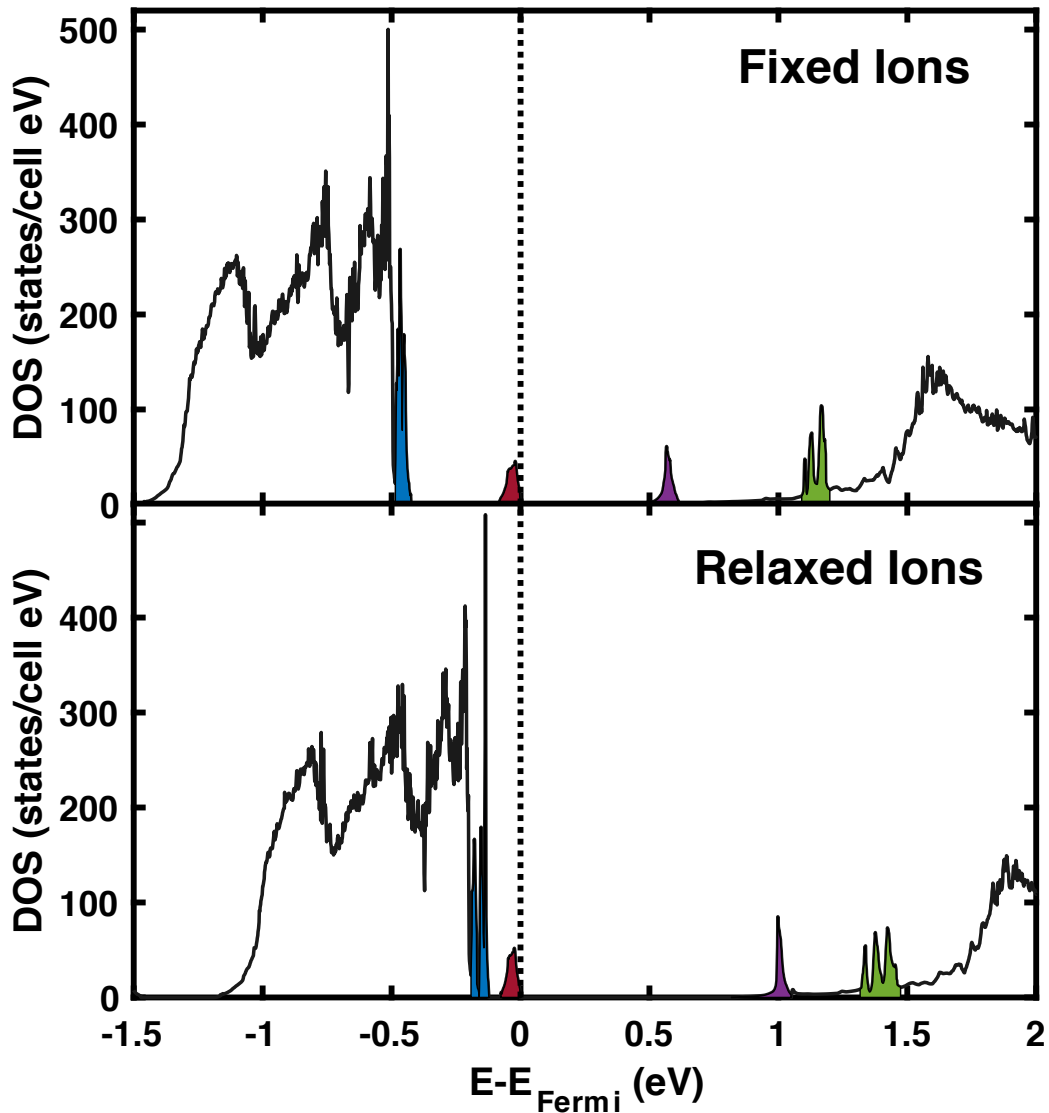
Figure 4.8: DOS comparison of defect-free pyrite with a relaxed 1.56% neutral S vacancy. The two DOS share main features, but the S vacancy causes four defect states to emerge with a slight shifting of the Fermi energy. The band gap also shifts from 0.92 eV to 0.82 eV with the introduction of a sulfur vacancy.

The local relaxation due to the S vacancy only affects the coordination of the three surrounding Fe cations; the rest of the supercell remains largely as bulk pyrite. Since we will see that the defect states are composed almost entirely of these Fe cations and under-coordinated S anion, it is not surprising that the midgap states shift so dramatically. Our calculated defect states are consistent with Krishnamoorthy et al. and Hu et al., who both calculated the electronic structure of S-vacant pyrite and also saw the emergence of defect states and a narrowing of the band gap [27, 26]. We do not present the relaxed defective band structure here because the k-point path may not sample all extrema of each band due to the broken unit cell symmetry. Therefore it is not guaranteed to match the DOS of the relaxed defect. However, we do notice that the band gap shifts to a direct transition at the Γ point, just like the fixed defect structure.

For both fixed and relaxed defect structures, we calculate a nonmagnetic ground state. Our

Figure 4.9: Density of states of S deficient pyrite with fixed and relaxed nuclear coordinates. The occupied defect states consist of the conduction band edge shaded blue and low midgap state shaded red. The unoccupied states, consisting of a high midgap and conduction band defects, are shaded purple and green, respectively. The four defect states appear in both structures, but the two midgap states shift farther apart when the ions are allowed to relax and increase the band gap from 0.45 eV to 0.82 eV.

experimental collaborators, however, see the emergence of magnetic ordering in pyrite particles that contain a larger number of grain boundaries: planar defects that separate regions of different crystalline orientation within a polycrystalline solid. Grain boundaries are likely a source for atomic defects since the crystalline orientations are often cleaved in non-stoichiometric ways, so the amount of localized atomic vacancies should increase with the increasing amount of grain boundaries. Because of this, we would expect our defective structure to contain some sort of magnetic ordering, but even with constraining the magnetism in our DFT calculations, we get no magnetic moments on any atom. We did look into using a hybrid functional (B3LYP) since they are known to provide more accurate magnetic results, but preliminary calculations also revealed a nonmagnetic ground state. These hybrid calculations are very computationally expensive, so are not worth pursuing in this thesis. The spin splitting in S deficient pyrite may be so small that DFT may not be sensitive enough to detect it. In order to get a better understanding of the magnetic structure of pyrite, we turn to crystal field theory since it provides a simple model of the magnetic electrons in pyrite.

4.5   Crystal Field Theory View of Defect States

The DOS and band structures obtained through DFT provide the relative energies of each defect state and point to strong electron-nuclear coupling in the system, but leave us with an incomplete picture of the full nature of the sulfur defects, especially the magnetic ordering of the structure. Our experimental collaborators see a marked decrease in the crystal field splitting in the pyrite particles containing more grain boundaries, so we expect that our S deficient structure to also show a decrease the crystal field splitting. We seek to understand the effects a sulfur vacancy has on the crystal field splitting and thus, the magnetic properties. These properties require localized orbitals, so we must transform our DFT-generated delocalized states into more localized atomic orbitals.

4.5.1   Crystal Field Theory for Pyrite
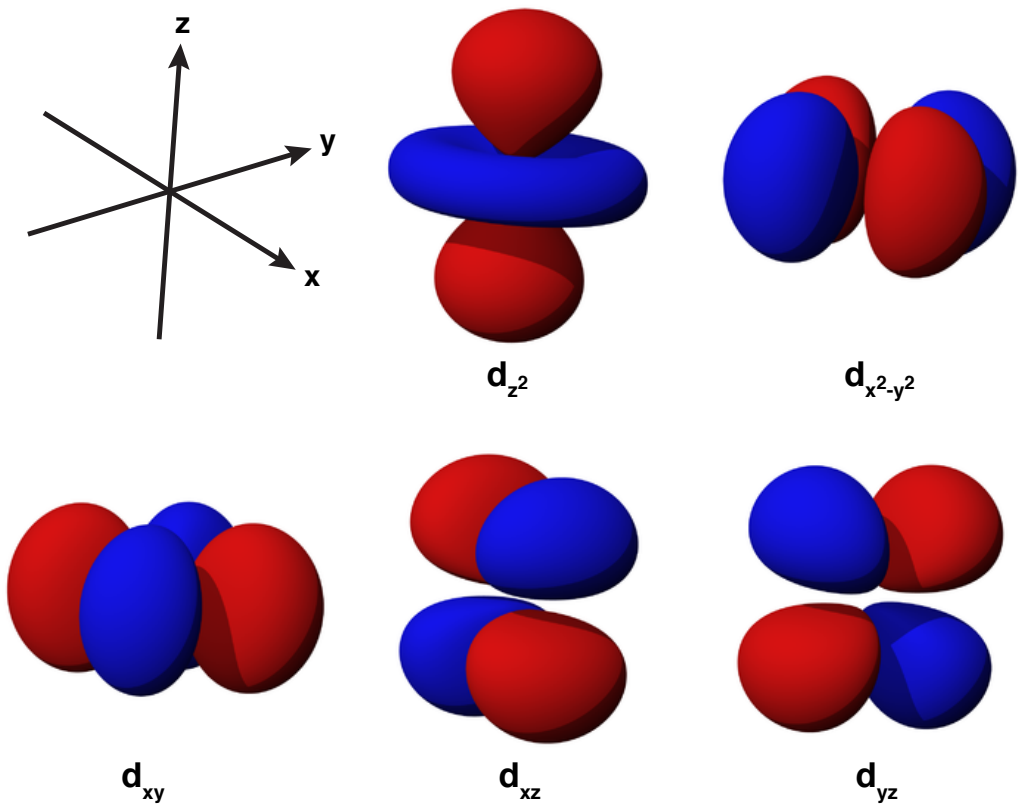
For a perfect octahedral complex, crystal field theory dictates that the d-orbitals, due to the electrostatic interactions between the electrons of the ligands and the lobes of the d-orbitals, break degeneracy and split into two different levels. The d_{xy}, d_{xz}, and d_{yz} orbitals, collectively referred to as t_{2g} orbitals, split to lower energy because the lobes of these orbitals, located off the bonding axes, interact little with the electrons of the ligands. The d_{z^2} and $d_{x^2-y^2}$ orbitals, collectively referred to as e_g orbitals, split to higher energy since the lobes of these orbitals are located on the bonding axes and do interact with the electrons of the ligands. Figure 4.10 shows the spatial arrangement of the lobes of each d-orbital, where the t_{2g} orbitals are listed below the e_g orbitals.

In pyrite, each iron has an oxidation state of 2+, so the d-orbitals in each iron are populated with 6 electrons. Pyrite is well known to exhibit low spin [47, 45, 99, 100], so the all t_{2g} are doubly occupied while the e_g orbitals remain unoccupied, resulting in a nonmagnetic structure. Pyrite does not actually share the same symmetry point group for pure octahedral complexes (point group O_h). It is part of the S_6 point group, which slightly distorts the octahedral coordination of the Fe atoms [47]. This causes the t_{2g} and e_g orbitals to split slightly, but the overall octahedral splitting remains largely unchanged. The energy splittings within the t_{2g} and e_g orbitals are small enough that we keep the octahedral nomenclature of the t_{2g} and e_g orbitals when discussing crystal field splitting in pyrite.

4.5.2   Wannier90 Methods
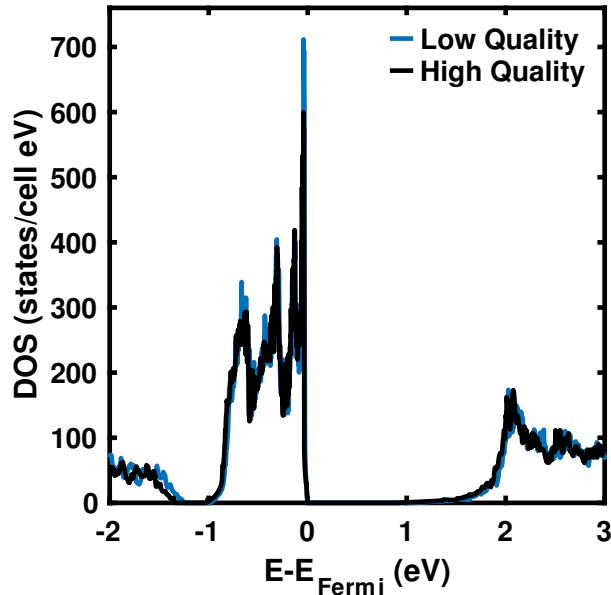
The DFT portion of all Wannier90 calculations were carried out with the same parameters as our regular DFT calculations, including the Hubbard U term, with exception to the choice of pseudo-potentials and energy cutoff. Due to the great computational cost of interfacing DFT with Wannier90 for our supercell, we chose to use softer pseudo-potentials with only 6 valence electrons and 8 valence electrons on each sulfur and iron atom, respectively. Because of the softer nature of these pseudo-potentials, we can decrease the basis set size by setting the plane wave energy

Figure 4.10: The five 3d-orbitals, where the red and blue lobes indicate spin up and spin down electron density, respectively. The three lower orbitals make up the t_{2g} orbitals and the two higher orbitals make up the e_g orbitals.
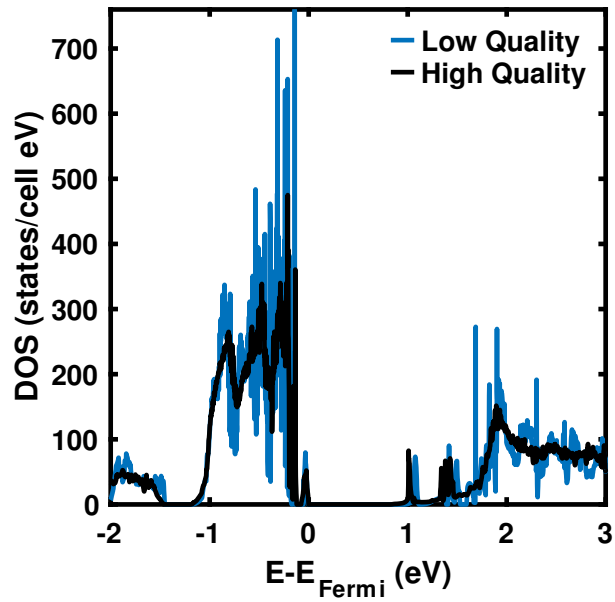
cutoff to 350 eV, which still ensures total energy convergence to within 10 meV per unit cell. We define these calculations as low quality and our normal DFT calculations with the harder pseudo-potentials and more valence electrons as high quality. Figures 4.11 and 4.12 show the comparison of the low quality and high quality calculated DOS for defect-free and S-deficient pyrite, respectively. For both S-deficient and defect-free structures, the low quality calculations exhibit a slightly larger band gap compared to the high quality calculations. We see a band gap shift from 0.92 eV to 1.09 eV for the defect-free structure and 0.82 eV to 0.96 eV for the S-deficient structure. The band gap shifts of 0.17 eV for the defect-free and 0.14 eV for the S-deficient supercells are relatively small and the low quality calculations in both cases capture all the major features of the high quality DOS, so we can use the low quality calculations to obtain qualitatively accurate results. We used a 3x3x3 Γ-centered Monkhorst-pack grid for all Wannier90 calculations.

Figure 4.11: DOS comparison of the low quality and high quality calculations for defect-free pyrite. The high quality calculation has a band gap of 0.92 eV while the low quality calculation has a band gap of 1.09 eV. Despite the relatively small band gap shift, the low quality DOS matches the main features of the high quality DOS quite well.

In order to transform the Bloch states calculated from DFT into the Maximally Localized Wannier Functions (MLWFs) using the Wannier90 program, we must first choose the trial functions

Figure 4.12: DOS comparison of the low quality and high quality calculations for S-vacant pyrite where the ions were allowed to relax. The band gap shifts from 0.82 eV to 0.96 eV between the high quality and low quality calculations. Despite the band gap shift, the low quality DOS contains all four defect states with the two unoccupied states slightly blue-shifted and captures all the main features of the high quality DOS with just a bit more noise.

in which to project the Bloch states onto as an initial guess for the MLWFs. Scaramucci et al. found that the most accurate crystal field splitting in Wannier90 originated from using only the d-orbital projections, since the inclusion of any additional orbitals resulted in the d-orbitals hybridizing with the additional orbitals and a lowering of the crystal field splitting [111]. The lowering of the splitting can be thought of as the contribution of the hybridization of the additional orbitals with the d-orbitals to the total splitting. We only want to calculate the total t_{2g}-e_g splitting for our calculations and characterize the d-orbital defect states, so we chose just the Fe d-orbitals as our trial functions. For our pyrite supercell containing 32 Fe atoms, we used a total of 160 d-orbital trial functions.

4.5.3   Determination of Outer and Frozen Energy Windows

The calculated MLWFs are not unique, so results depend heavily upon the choice of outer and inner energy windows. We want to minimize the total spread of the MLWFs to provide the most localized functions. Comparing the Wannier90-generated band structure to the DFT-generated band structure and visualizing the spatial spread of the resulting MLWFs also gives us a sense of how good the results are. Within the frozen energy window, the Wannier90-generated band structure should exactly match the DFT-generated band structure since the states are technically frozen and should yield the same energies.

Figures 4.13 and 4.14 show that the inner frozen energy window affects the sum of the MLWF spreads and crystal field splitting much more than the outer energy window. In Figure 4.13, we see that spread and t_{2g}-e_g splitting vary by under 4% over a large range of outer window values. A small change in the inner frozen window, shown in Figure 4.14, varies the spread and t_{2g}-e_g splitting by over 200%. Since the outer window has less impact on the final results, I chose to focus on optimizing the inner frozen window with a reasonable, but not completely optimized, outer energy window.

Our choice of outer and inner energy windows must include both valence and conduction bands since the crystal field splitting is dependent on the band gap and surround states. We want

Figure 4.13: Sensitivity of the total spread and t_{2g}-e_g splitting to the choice of the outer energy window. Panel a) varies the lower value of the outer window with the outer window maximum fixed at 18 eV, while panel b) varies the upper limit of the outer window with the minimum fixed at -9.5 eV. The total spread and crystal field splitting do not change significantly, so optimizing the outer window limits are not as crucial in determining the final results of the Wannier90 calculation.
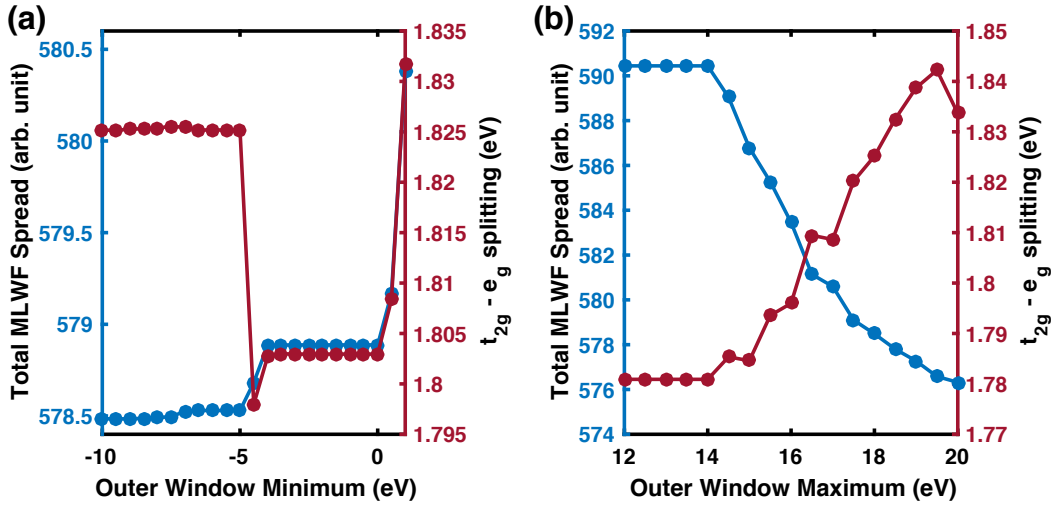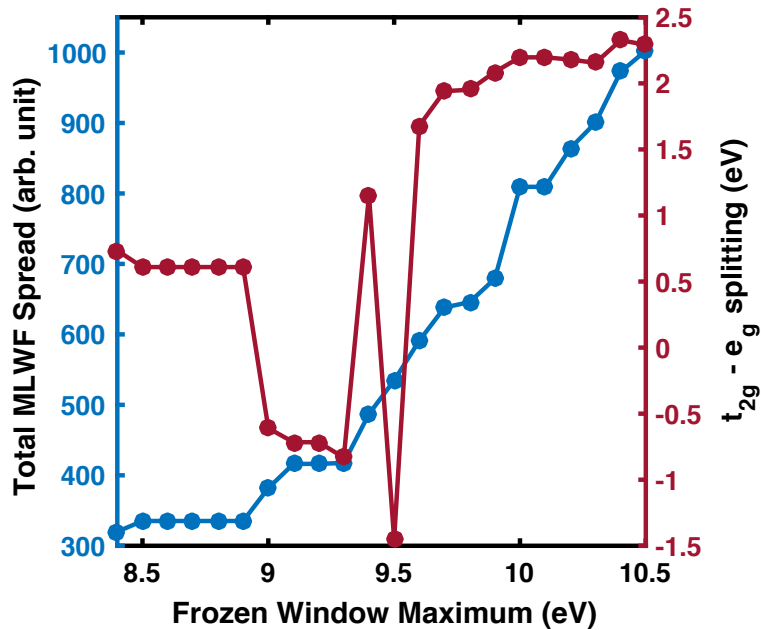

Figure 4.14: Sensitivity of the total spread and crystal field splitting to the choice of the inner frozen energy window. Here we fixed the frozen window minimum to 6.6 eV and varied the frozen window upper limit. Both spread and t_{2g}-e_g splitting are very sensitive to the choice of inner window and undergo large fluctuations of over 200% over a small range of the frozen window maxima. Optimizing the frozen window is crucial to obtaining the best results in the Wannier90 calculations.

the smallest frozen energy window that provides convergence because a smaller frozen window minimizes the overall MLWF spread. After testing many different energy window parameters, I found that a frozen inner window near 6.60-9.80 eV gives the smallest spreads while still converging. These values are absolute energies, so relative to the defect-free Fermi energy of 7.40 eV, the window spans -0.80-2.4 eV and includes both valence and conduction energy bands.

During the disentanglement and wannerization procedures, we converged the spread to within 1×10^{-10}, where the differences in spread had to stay below the specified convergence tolerance for at least eight successive iterations. Once the calculation finished, we determined the crystal field splitting by comparing the on-site energies, the diagonal elements of the Hamiltonian matrix in the MLWF basis, of each Fe d-orbital. The difference in on-site energies of the d-orbitals gave us the crystal field splitting of the supercell. For a perfectly octahedral complex, we expect only 2 different on-site energies: one for the t_{2g} orbitals and the other for the e_g orbitals. In a first approximation of the pyrite unit cell where we only look at the 6 surrounding S atoms, this holds true. If we expand the neighborhood of the Fe cation beyond the six S atoms, the symmetry lowers and the resulting electrostatic field lifts the degeneracies of the t_{2g} and e_g levels. Because of this we would expect to see two definite t_{2g} and e_g bands with a distribution of orbital energies in both bands.

4.5.4   Wannier90 Results

Using the Wannier90 program, we are able to transform the delocalized Bloch states generated through DFT into localized Wannier functions that are indexed by orbital number n and ion coordinate $\mathbf{R}$. We calculated the on-site energies of the Fe d-orbitals in defect-free and S deficient pyrite and find a large shift in crystal field splitting between the defect-free and sulfur deficient supercells. Figure 4.15 shows the histograms of the Fe d-orbital on-site energies for both defect-free and S deficient structures. The defect-free unit cell exhibits the typical crystal field splitting we expect from pyrite with a t_{2g}-e_g gap of 2.18 eV using the outer and inner energy windows 0-18 eV and 6.6-9.8 eV, respectively. The t_{2g} and e_g on-site energies each have a slight distribution that is

consistent with the differences in symmetry of pyrite and a pure octahedral structure.

Since many Wannier90 calculations using different energy windows yielded similar converged orbital spreads, our calculations are at most qualitative due to the low quality DFT calculations used to interface with Wannier90. We cannot pin down the exact value of the crystal field splitting, but define a range of crystal field splittings that encompasses all the calculations. All of our converged results for defect-free pyrite fell within the 1.9-2.2 eV range, so we are confident that the crystal field splitting of defect-free pyrite lies somewhere between 1.9 and 2.2 eV. This range is consistent with the experimental and calculated splittings in the literature [105, 107, 98, 108, 109, 110].

The Fe d-orbital on-site energy histogram of the relaxed S deficient structure shows the emergence of two midgap defect states and a broadening of the main t_{2g} and e_g histogram peaks. The t_{2g}-e_g splitting with an outer window of 0-18 eV and inner window set to 6.6-9.8 eV is 0.73 eV, 1.45 eV below the comparable defect-free structure. Over a range of energy windows and S vacancy positions within the supercell, the calculated crystal field splittings all fall within 0.65-0.95 eV. Comparing the defect free splitting of 1.9-2.2 eV to the S-vacant splitting of 0.65-0.95 eV, we get an average splitting difference of 1.25 eV with a minimum and maximum possible difference of 0.95 eV and 1.55 eV, respectively. We see a lowering of the t_{2g}-e_g gap by at least 0.95 eV, or a factor of 2, for S deficient pyrite compared to the defect-free structure.

To test the validity of our results, we compared the Wannier90 generated band structure with the DFT generated band structure. Within the inner energy window, the two band structures should be identical. Figures 4.16 and 4.17 show the comparison of the Wannier90 band structure with the DFT band structure of S deficient pyrite. There is good agreement between the two band structures, but they are not identical. This could be due to our exclusion of orbitals that normally contribute to the band structure around the band gap. We only use Fe d-orbitals for our Wannier90 calculations to calculate the total t_{2g}-e_g splitting, but DFT calculations show that sulfur p-orbitals contribute to the band structure, especially at the conduction band minimum. These are difficult calculations to perform, so the shown agreement between the band structures is sufficient for our qualitative purposes.

Figure 4.15: Histograms of Fe d-orbital on-site energies obtained through Wannier90 with an outer window of 0-18 eV and an inner window of 6.6-9.8 eV. Defect-free pyrite is shown in panel a) with a crystal field splitting of 2.18 eV. S deficient pyrite is shown in panel b) with a crystal field splitting of 0.73 eV due to the defect states within the octahedral splitting. In both figures, the t_{2g} orbitals have lower energy than the e_g orbitals, which we expect because of the octahedral coordination of the Fe atoms. Only six orbitals lie outside the normal splitting in panel b), confirming that the defect is spatially localized.
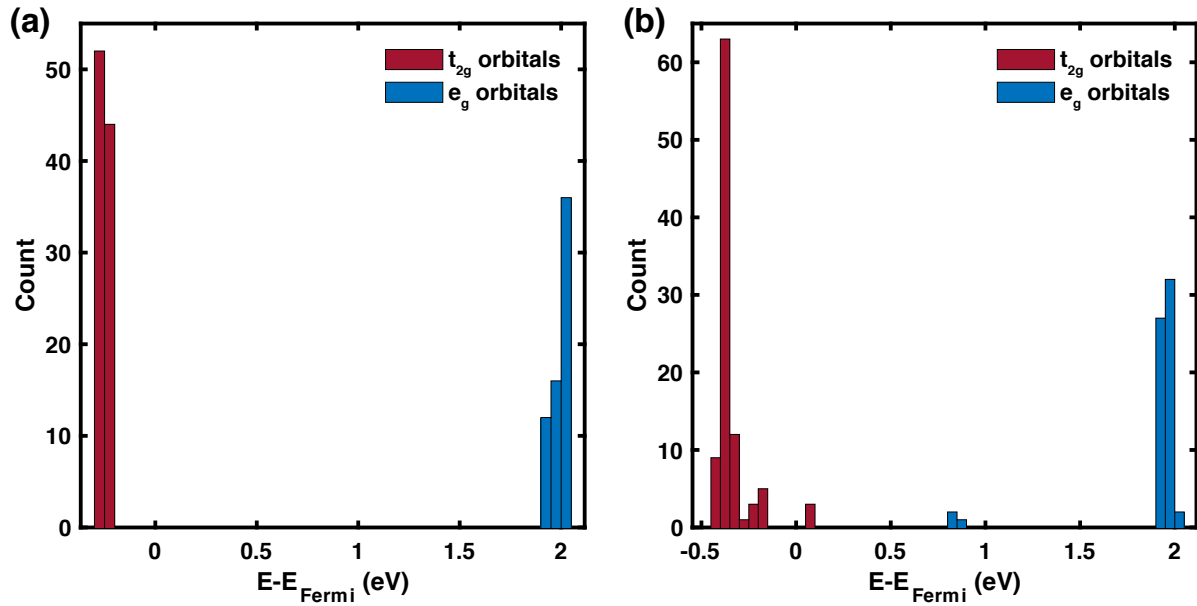
Figure 4.16: Band structure comparison of the DFT states and the Wannier90 states for S-vacant pyrite. There is decent, but not perfect, agreement between the Wannier90 and DFT calculations.
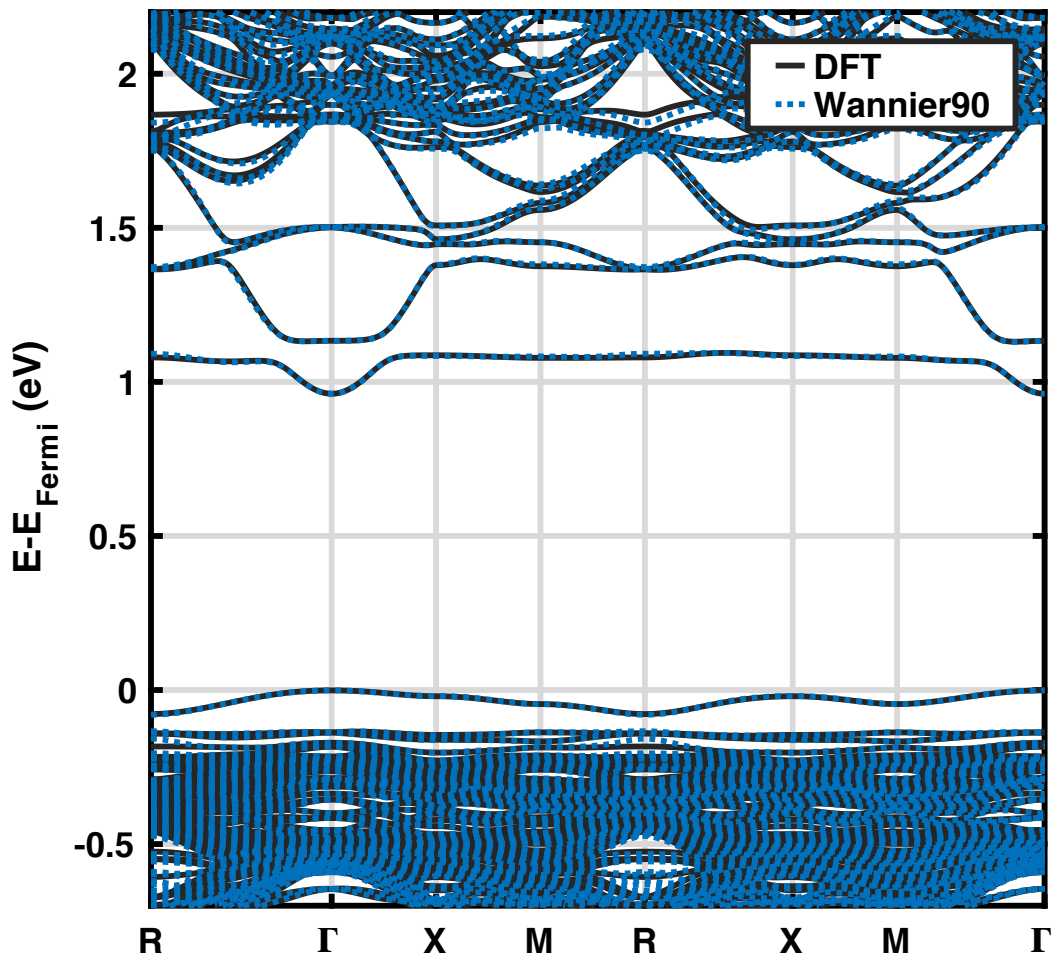
Figure 4.17: Band structure comparison of the DFT states and Wannier90 states for S-vacant pyrite. Panel a) shows the zoomed in valence band maximum while b) shows the zoomed in conduction band minimum. For the most part, there is good agreement between the Wannier90 states and DFT states. The major discrepancy occurs at the R point in panel a).
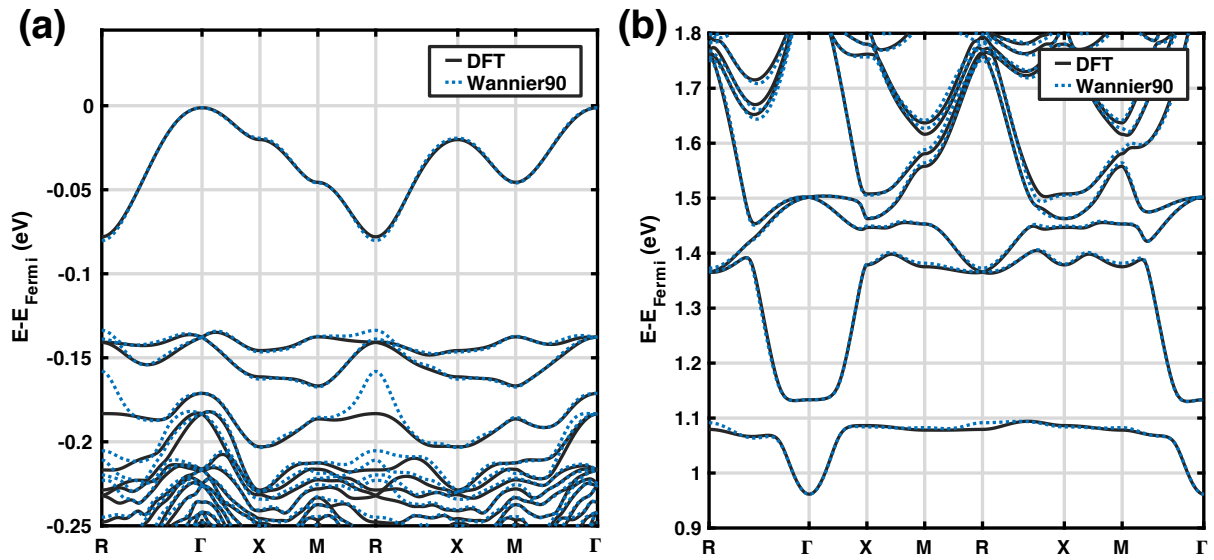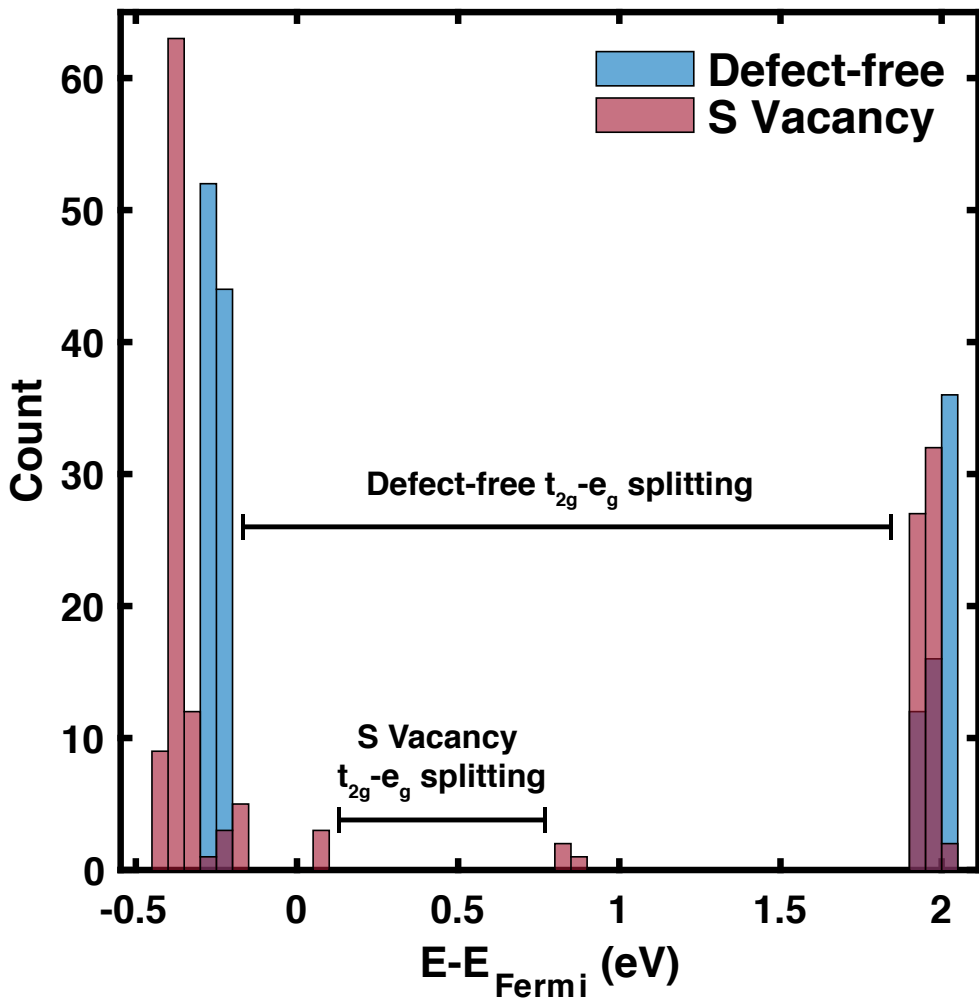
Figure 4.18 shows the direct comparison of the t_{2g}-e_g splittings for defect-free and S deficient pyrite. The majority of the d-orbitals of the S deficient structure have similar energies to the defect-free pyrite while only six total orbitals contribute to the midgap defect states. Our calculated decrease in the crystal field splitting is consistent with our collaborator's experiments. They notice a decrease in the first direct optical transition, which corresponds to the $t_{2g} - e_g$ gap, by roughly a factor of 2 for their large pyrite microparticles compared to their small pyrite nanoparticles. The larger particles contain more grain boundaries, and possibly more localized defects, than the smaller nanoparticles, which corresponds to our S defective and defect-free structures, respectively.

4.5.5   Defect State Visualization

Now that we have both adiabatic (DFT) and diabatic (Wannier90) representations of S deficient pyrite, we can fully visualize the defect states. In the adiabatic picture, these states consist of a linear combination of atomic orbitals. Figure 4.19 shows the charge density of the four adiabatic defect states and Figures 4.20 and 4.21 list the atom composition of each defect state. All four states are localized around the vacant sulfur atom since the change density contours in Figure 4.19 account for at least 90% of the electron density over the respective energy range.

The occupied valence band defect state labeled in blue is located at the edge of the massive conduction band edge. Normally at the Fermi energy, this band edge is shifted downward because the low midgap state is occupied, setting the Fermi energy at its energy. This valence band defect is composed of three energy bands and localized over the three Fe atoms connected to the under-coordinated S atom normally bonded to the now vacant S atom. The orbital composition of each of the three atoms is primarily t_{2g} orbitals with mostly equal contributions from the d_{xy}, d_{xz},and d_{yz} orbitals. Although the orbitals look similar to d_{z^2} orbitals in Figure 4.19, they are oriented off the bonding axes like t_{2g} orbitals and could be a linear combination of the three t_{2g} orbitals. The occupied low midgap state is located just below the Fermi energy, labeled in red, and consists of the same Fe atoms as the valence band defect with the addition of the under-coordinated S atom. The S atom contributes only p-orbital character to the defect state, while the Fe atoms are composed

Figure 4.18: Comparison of defect-free and S deficient Fe d-orbital on-site energies. Here we clearly see the collapse of the crystal field splitting, although only six orbitals contribute to the midgap defect states. The majority of the Fe d-orbitals remain in the defect-free splitting regime.

of equal amounts of t_{2g} and e_g orbitals. From the charge density contour, this state looks more t_{2g} due to the four-lobed nature of the Fe orbitals and the orientation off the bonding axes. The high midgap state is unoccupied, labeled in purple, and located at the upper edge of the band gap just before the rise of the normal conduction band in pyrite. This state is composed of the three under-coordinated irons and one under-coordinated sulfur left from the removal of the neutral sulfur atom. The S atom has mainly sp^3 character and the Fe atoms have mainly e_g character with the orbitals oriented along the bonding axes. The last defect state is located within the beginning of the conduction band and labeled green. The charge density of this state resembles e_g orbitals with the orbital orientation along the bonding axes.

In the diabatic representation, each orbital is localized to a single atom and the defect states are composed of multiple atomic orbitals. Since we only project the Bloch states onto Fe d-orbitals during the diabatization process, we obtain just the d-orbital contribution to the defect states. Figure 4.22 shows the charge density contours for the occupied t_{2g} and unoccupied e_g defect orbitals, where three atomic orbitals make up each defect state. These correspond loosely to the low midgap and high midgap defect states in the adiabatic picture, respectively. The occupied t_{2g} defect states are located slightly off their normal axes where the lobe pointing toward the S vacancy is abnormally large. These orbitals reside on the under-coordinated Fe atoms unlike the adiabatic representation where the lower midgap defect is located on the fully coordinated Fe atoms next to the under-coordinated S atom. The unoccupied e_g defect states also reside slightly off their normal axes and resemble d_{z^2} orbitals with the lobes pointing toward sulfur vacancy larger than than the ones pointing away from it. These orbitals, like the adiabatic representation, are located on the under-coordinated Fe atoms around the S vacancy.

Figure 4.23 shows the d-orbitals of the normally coordinated Fe atoms in the S vacant su-percell. These orbitals portray the typical d-orbitals we expect to see in a normal octahedrally coordinated ion with the three lower t_{2g} states that reside off the bonding axes and two higher energy e_g states oriented along the bonding axes. Since the d-orbitals of the normally coordinated Fe atoms in the defective structure are identical to those in the defect-free supercell, S deficient

Figure 4.19: Electron density visualization of each of the four defect states in the adiabatic representation. All states are localized to the atoms surrounding the S vacancy since the charge density contours contain at least 90% of the total charge density for each state, and the defect states are color-coded to match the DOS and band structure in Figures 4.9 and **??**, respectively. The occupied valence band and low midgap defect states are localized to the Fe atoms coordinated to under-coordinated S atom due to the vacancy. The unoccupied high midgap and conduction band defect states reside on the under-coordinated Fe atoms next to the S vacancy. Only the midgap states contain additional S atom character.
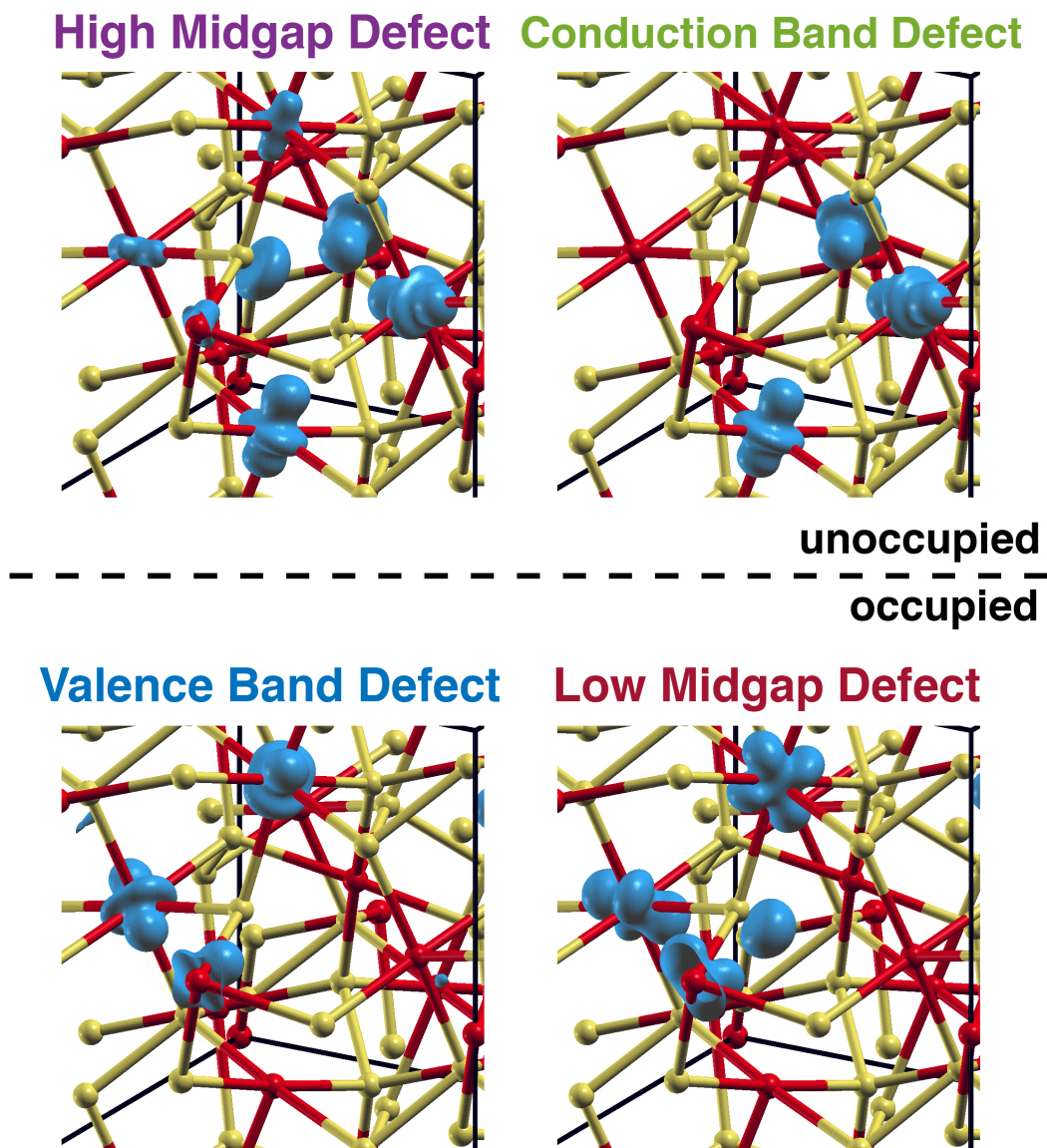
Figure 4.20: Atom and orbital contribution of the two occupied defect states in the adiabatic representation. The valence band defect is given as an average of the three energy bands that make up that state. The low midgap defect state is located just below the Fermi energy and consists of one energy band. The left panels show the atom contributions to the defect state where the 63 S atoms are listed first and labeled yellow and the 32 Fe atoms are listed second and labeled red. The right panels show the orbital composition of each atom that contributes most to the charge density of the defect state, which are labeled with * in the left panels. Only the t_{2g} orbitals of the three Fe atoms contribute significantly to the valence band defect state in S-vacant pyrite. The low midgap defect state is comprised mainly of three Fe atoms that have an even mix of t_{2g} and e_g d-orbitals and one S atom that has mainly p-orbital character. The labeling of these states is color-coded to match the DOS in Figure 4.9.
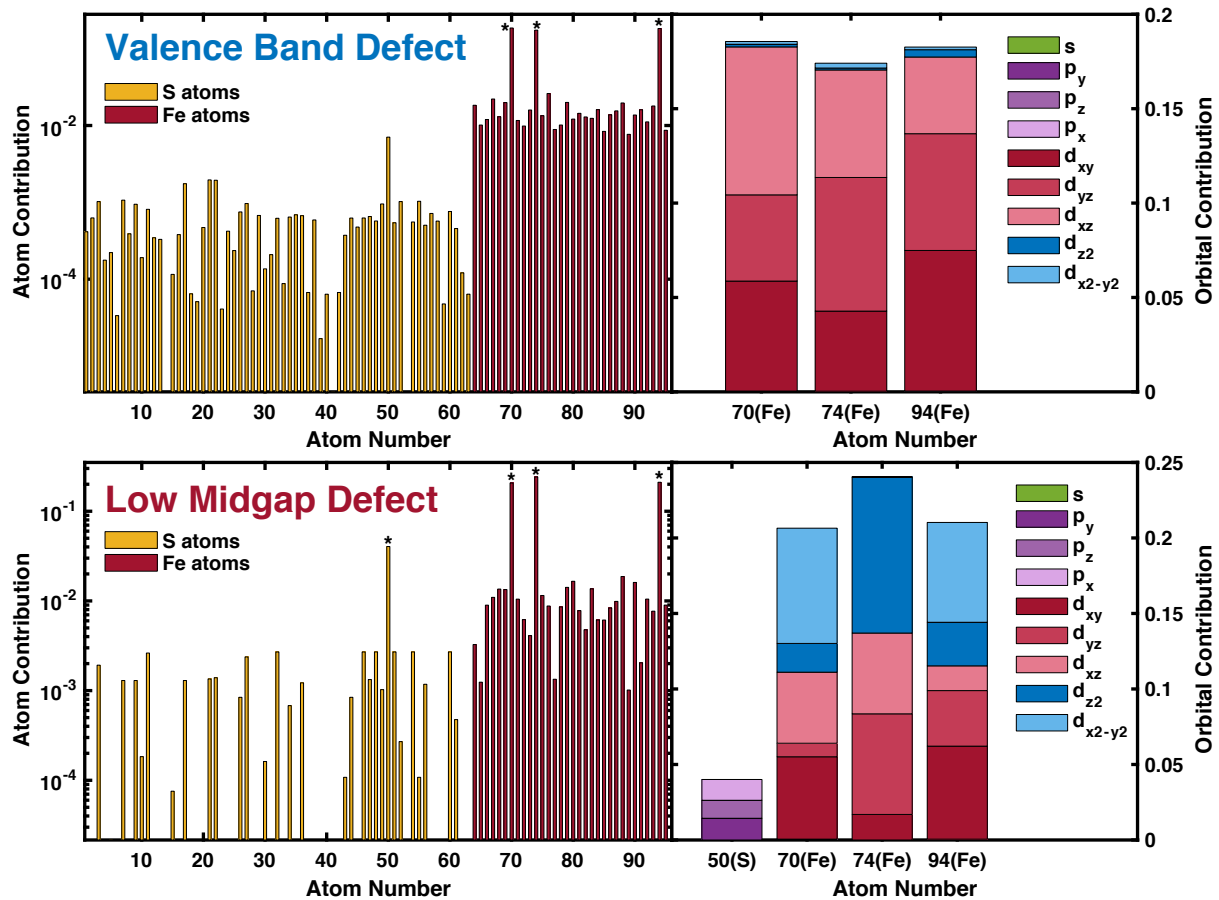
Figure 4.21: Atom and orbital contribution of the two unoccupied defect states in the adiabatic representation. The left panels show the atom contributions to the defect state where the 63 S atoms are listed first and labeled yellow and the 32 Fe atoms are listed second and labeled red. The right panels show the orbital composition of each atom that contributes a significant amount to the charge density of the particular energy band, which are labeled with * in the left panels. The high midgap state is localized to three Fe atoms and one S atom, where the S atom shows sp^3 orbital character and the Fe atoms have more e_g character than t_{2g}. The conduction band defect state consists mainly of three Fe atoms with the majority of the character being e_g d-orbitals. Each of the Fe and S atoms that contribute a significant amount to the total charge density are located next to the vacant S atom in the pyrite supercell and the labeling of these states is color-coded to match the DOS in Figure 4.9.
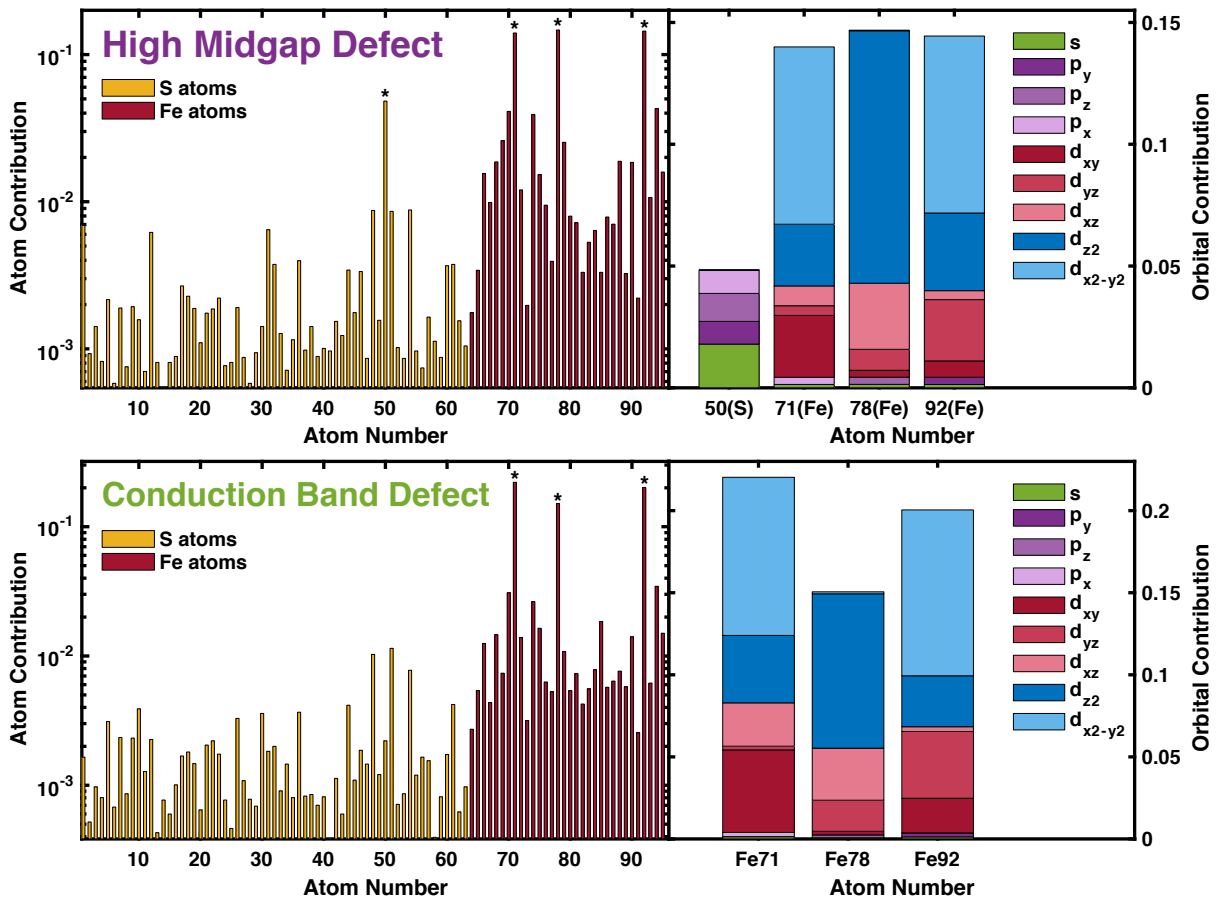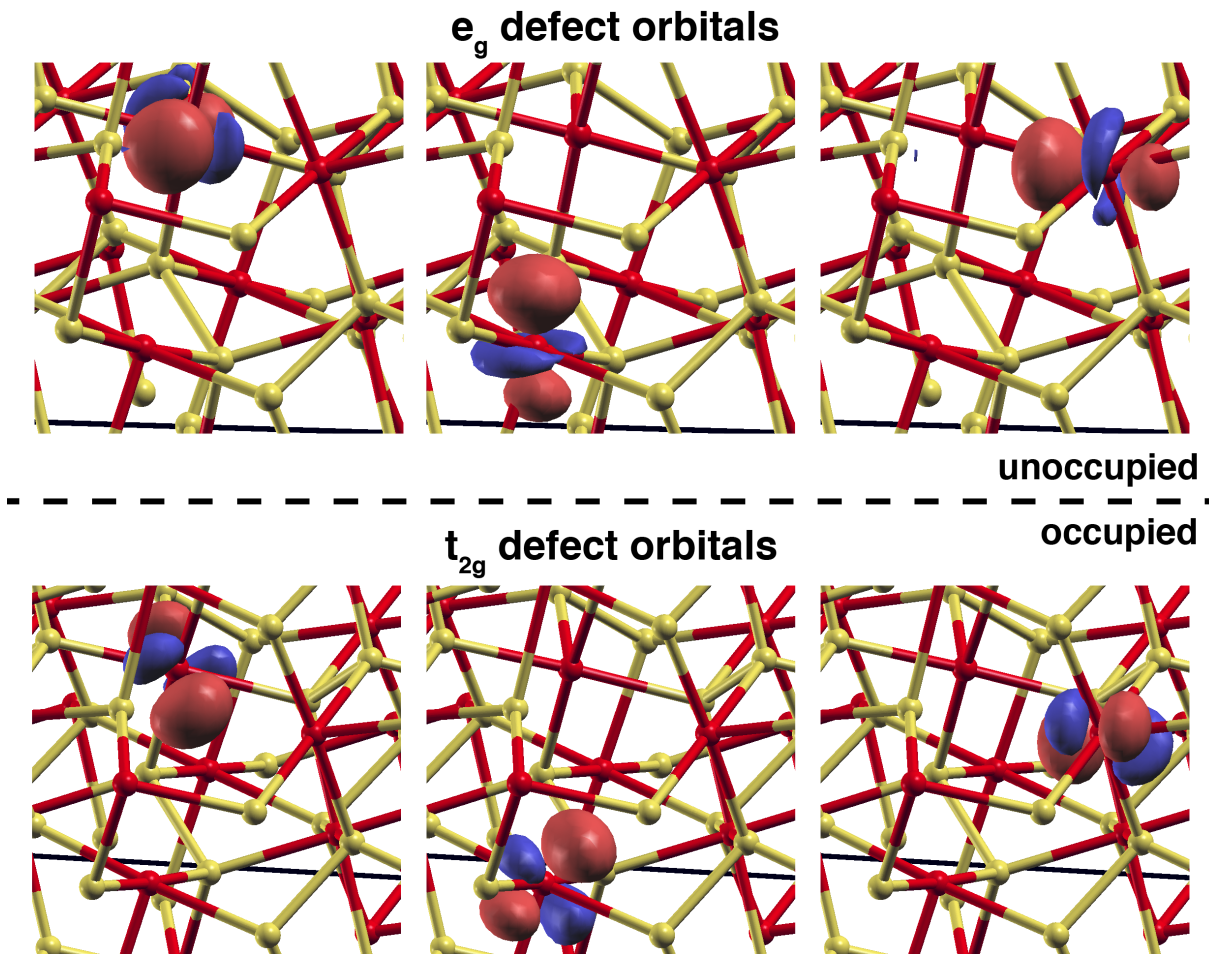
Figure 4.22: Electron density visualization of the six defect d-orbitals within the diabatic representation. The positive and negative lobes of each orbital are colored red and blue, respectively. The lower occupied orbitals have distorted t_{2g} character, while the upper unoccupied orbitals have distorted e_g character. Each defect orbital is located on an under-coordinated Fe atom next to the vacant sulfur, so the defect states are spatially localized within the structure.

pyrite consists mainly of bulk pyrite. Only the few atoms surrounding the vacancy are affected and contribute to the defect states seen in our calculations.
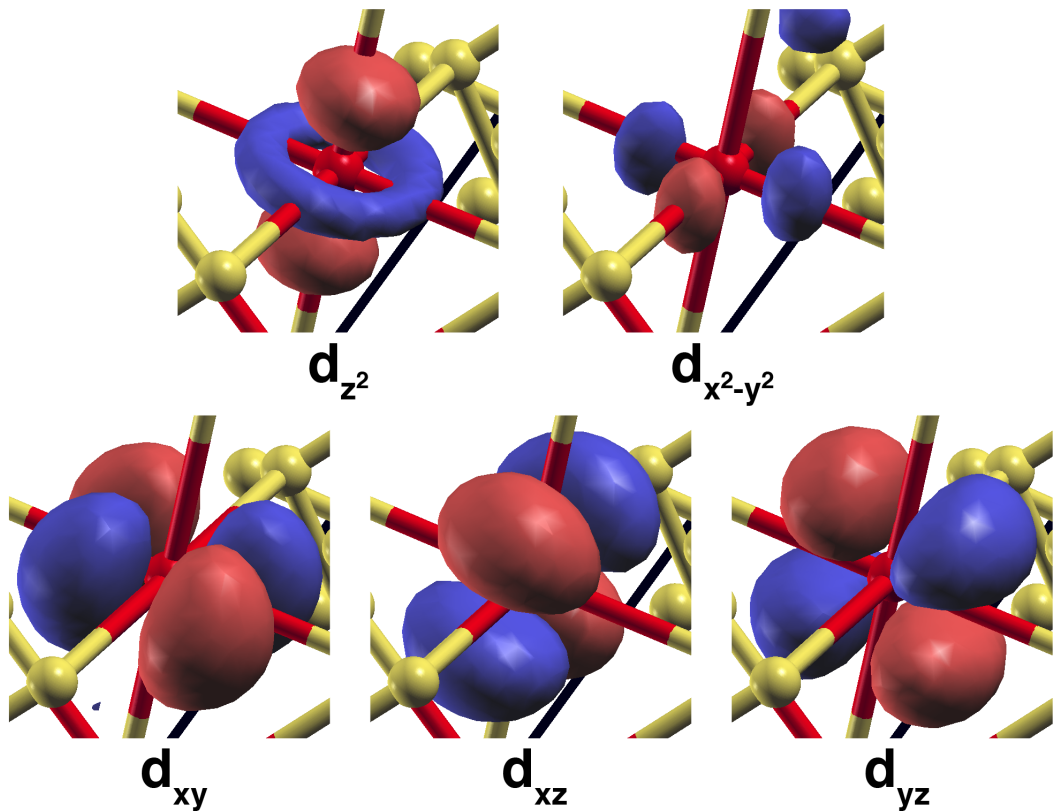
4.5.6 Possible Magnetism in Sulfur Deficient Pyrite

In all our Wannier90 calculations, we see no difference between the spin up and spin down calculations. Both yield the same splittings, orbitals, and band structures, so the calculated supercells are all nonmagnetic. However, the collapse of the crystal field splitting of the S deficient structure, shown in Figure 4.18, points to the possibility of a spin crossover near the defect. A spin crossover occurs when the energy splitting between the t_{2g} and e_g orbitals lowers enough to make the high spin state energetically favorable. For pyrite, the high spin state consists of one doubly occupied t_{2g} with the four other orbitals containing one electron each. This state exhibits magnetic ordering and may be what our collaborators see in their synthesized nanoparticles. There may also be a possibility of energy splitting between the spin up and spin down states resulting in magnetic ordering. The energy splitting between the spin up and spin down electrons may be so small that DFT and Wannier90 calculations are insensitive to it.

4.6 Conclusion

In this chapter, we showed the effect of S vacancies in pyrite under both the adiabatic and diabatic representations. Our DFT calculations predict that a sulfur vacancy causes a narrowing of pyrite's band gap with the introduction of midgap, valence band, and conduction band defect states. The sensitivity of the defect state energies to the nuclear coordinates points to strong electron-nuclear coupling in the material. In the diabatic representation, the crystal field splitting of pyrite decreases by a factor of two in the presence of the defect due to the emergence of midgap defect states. These states are akin to the midgap defect states of the adiabatic representation. In both representations, the midgap defect states are localized to the Fe atoms surrounding the S vacancy and lower their respective energy gap. The degeneracies of the Fe d-orbitals orbitals lift with a sulfur defect, which may cause a spin crossover and an emergent magnetic state. While we

Figure 4.23: Electron density visualization of the d-orbitals of a normally coordinated Fe atom within the S deficient pyrite supercell and under the diabatic representation. Positive and negative lobes of the d-orbitals are colored red and blue, respectively. These orbitals depict the typical d-orbitals we expect with the normal octahedral splitting of lower energy d_{xy}, d_{xz}, and d_{yz} (t_{2g}) orbitals and the higher energy d_{z^2} and $d_{x^2-y^2}$ (e_g) orbitals. The orbitals calculated from the defect-free supercell in the diabatic representation are nearly identical to those shown in this figure.

characterized a single sulfur defect in a pyrite supercell, we don't know of its interactions with other sulfur defect states. Experimentally, sulfur defects in pyrite may exist in clusters, for example at a grain boundary, instead of being evenly dispersed throughout the solid. Future research could probe these interactions and look at the mobility of the defect states to get a clearer picture of experimentally relevant pyrite.

Bibliography

[1] David Rickard and George W. Luther, III. Chemistry of Iron Sulfides. Chem. Rev., 107(2):514–562, February 2007.

[2] Thomas S. Duffy. Synchrotron facilities and the study of the Earth's deep interior. Rep. Prog. Phys., 68(8):1811–1859, 2005.

[3] Yingwei Fei, Charles T. Prewitt, Ho-kwang Mao, and Constance M. Bertka. Structure and Density of FeS at High Pressure and High Temperature and the Internal Structure of Mars. Science, 268(5219):1892–1894, June 1995.

[4] Yanyan Gong, Jingchun Tang, and Dongye Zhao. Application of iron sulfide particles for groundwater and soil remediation: A review. Water Res., 89:309–320, February 2016.

[5] Ronald R. Patterson, Scott Fendorf, and Mark Fendorf. Reduction of Hexavalent Chromium by Amorphous Iron Sulfide. Environ. Sci. Technol., 31(7):2039–2044, July 1997.

[6] George D. Cody, Nabil Z. Boctor, Timothy R. Filley, Robert M. Hazen, James H. Scott, Anurag Sharma, and Hatten S. Yoder, Jr. Primordial Carbonylated Iron-Sulfur Compounds and the Synthesis of Pyruvate. Science, 289(5483):1337–1340, August 2000.

[7] Gnter Wchtershuser. Iron-Sulfur World. In Wiley Encyclopedia of Chemical Biology, pages 1–8. American Cancer Society, 2008.

[8] Jun Zhang, Feng-Liang Liu, Tian-Ping Ying, Na-Na Li, Yang Xu, Lan-Po He, Xiao-Chen Hong, Yun-Jie Yu, Ming-Xiang Wang, Jian Shen, Wen-Ge Yang, and Shi-Yan Li. Observation of two superconducting domes under pressure in tetragonal FeS. npj Quantum Materials, 2(1):49, September 2017.

[9] Fabio Ricci and Eric Bousquet. Unveiling the Room-Temperature Magnetoelectricity of Troilite FeS. Phys. Rev. Lett., 116:227601, June 2016.

[10] S. J. Kuhn, M. K. Kidder, D. S. Parker, C. dela Cruz, M. A. McGuire, W. M. Chance, Li Li, L. Debeer-Schmitt, J. Ermentrout, K. C. Littrell, M. R. Eskildsen, and A. S. Sefat. Structure and property correlations in FeS. Physica C, 534:29–36, March 2017.

[11] Xiaofang Lai, Hui Zhang, Yingqi Wang, Xin Wang, Xian Zhang, Jianhua Lin, and Fuqiang Huang. Observation of Superconductivity in Tetragonal FeS. J. Am. Chem. Soc., 137(32):10148–10151, August 2015.

[12] Alec Kirkeminde, Maogang Gong, and Shenqiang Ren. The Renaissance of Iron Pyrite Photovoltaics: Progress, Challenges, and Perspectives. In Low-cost Nanomaterials, Green Energy and Technology, pages 137–166. Springer, London, 2014.

[13] Chet Steinhagen, Taylor B. Harvey, C. Jackson Stolle, Justin Harris, and Brian A. Korgel. Pyrite Nanocrystal Solar Cells: Promising, or Fool's Gold? J. Phys. Chem. Lett., 3(17):2352–2356, September 2012.

[14] Carolyn I. Pearce, Richard A. D. Pattrick, and David J. Vaughan. Electrical and Magnetic Properties of Sulfides. Rev. Mineral. Geochem., 61(1):127–180, January 2006.

[15] Anthony V. Powell, Paz Vaqueiro, Kevin S. Knight, Laurent C. Chapon, and Rodolfo D. Snchez. Structure and magnetism in synthetic pyrrhotite Fe_7S_8: A powder neutron-diffraction study. Phys. Rev. B, 70(1):014415, July 2004.

[16] A. Rohrbach, J. Hafner, and G. Kresse. Electronic correlation effects in transition-metal sulfides. J. Phys. Condens. Matter, 15(6):979–996, 2003.

[17] S. Wells, D. Alfe, L. Blanchard, J. Brodholt, M. Calleja, R. Catlow, D. Price, R. Tyler, and K. Wright. Ab-initio simulations of magnetic iron sulphides. Mol. Simul., 31(5):379–384, 2005.

[18] S. A. Kissin and S. D. Scott. Phase relations involving pyrrhotite below 350 degrees C. Economic Geology, 77(7):1739–1754, November 1982.

[19] Haipeng Wang and Ian Salveson. A review on the mineral chemistry of the non-stoichiometric iron sulphide, $fe_{1-x}s$ ($0 \leq x \leq 0.125$): polymorphs, phase relations and transitions, electronic and magnetic structures. Phase Transitions, 78(7-8):547–567, September 2005.

[20] R. C. Sharma and Y. A. Chang. Thermodynamics and phase relationships of transition metal-sulfur systems: Part III. Thermodynamic properties of the Fe-S liquid phase and the calculation of the Fe-S phase diagram. MTB, 10(1):103–108, March 1979.

[21] Hiromoto Nakazawa and Nobuo Morimoto. Pyrrhotite Phase Relations below 320°C. Proc. Jpn. Acad., 46(7):678–683, 1970.

[22] Olof Kruse. Mossbauer and X-ray study of the effects of vacancy concentration in synthetic hexagonal pyrrhotites. Am. Mineral., 75:755–763, 1990.

[23] Jack D. Dunitz and Harold A. Scheraga. Exercises in prognostication: Crystal structures and protein folding. PNAS, 101(40):14309–14311, October 2004.

[24] P. Martin, G. D. Price, and L. Vocadlo. An ab initio study of the relative stabilities and equations of state of FeS polymorphs. Mineralogical Mag, 65(2):181–191, April 2001.

[25] M. Birkholz, S. Fiechter, A. Hartmann, and H. Tributsch. Sulfur deficiency in iron pyrite (FeS_{2-x}) and its consequences for band-structure models. Phys. Rev. B, 43(14):11926–11936, May 1991.

[26] Jun Hu, Yanning Zhang, Matt Law, and Ruqian Wu. First-principles studies of the electronic properties of native and substitutional anionic defects in bulk iron pyrite. Phys. Rev. B, 85(8):085203, February 2012.

[27] Aravind Krishnamoorthy, F. William Herbert, Sidney Yip, Krystyn J. Van Vliet, and Bilge Yildiz. Electronic states of intrinsic surface and bulk vacancies in FeS_2. J. Phys. Condens. Matter, 25(4):045004, 2013.

[28] S. Guénon, J. G. Ramírez, Ali C. Basaran, J. Wampler, M. Thiemens, and Ivan K. Schuller. Search for New Superconductors: an Electro-Magnetic Phase Transition in an Iron Meteorite Inclusion at 117 K. J. Supercond. Nov. Magn., 30(2):297–304, February 2017.

[29] William M Skinner, H. Wayne Nesbitt, and Allen R Pratt. XPS identification of bulk hole defects and itinerant Fe 3d electrons in natural troilite (FeS). Geochim. Cosmochim. Acta, 68(10):2259–2263, 2004.

[30] Nathalie M. Pedoussaut and Cora Lind. Facile Synthesis of Troilite. Inorg. Chem., 47(2):392–394, January 2008.

[31] M. I. Oshtrakh, Z. Klencsr, E. V. Petrova, V. I. Grokhovsky, A. V. Chukin, A. K. Shtoltz, A. A. Maksimova, I. Felner, E. Kuzmann, Z. Homonnay, and V. A. Semionkin. Iron sulfide (troilite) inclusion extracted from Sikhote-Alin iron meteorite: Composition, structure and magnetic properties. Mater. Chem. Phys., 174:100–111, May 2016.

[32] J. C. Ward. The Structure and Properties of Some Iron Sulphides. Rev. Pure Appl. Chem., 20:175–206, 1970.

[33] Ssu Han Li, Yen-Hua Chen, Jey-Jau Lee, and Hwo-Shuenn Sheu. Phase transition of iron sulphide minerals under hydrothermal conditions and magnetic investigations. Phys. Chem. Miner., 45(1):27–38, January 2018.

[34] N. Morimoto, H. Nakazawa, K. Nishigucmi, and M. Tokonami. Pyrrhotites: Stoichiometric Compounds with Composition $Fe_{n-1}S_n$ (n≥8). Science, 168(3934):964–966, May 1970.

[35] N. Morimoto, Atsuo Gyobu, Hiromu Mukaiyama, and Eiji Izawa. Crystallography and stability of pyrrhotites. Economic Geology, 70(4):824–833, July 1975.

[36] Robert Heron Carpenter and Geroge A. Desborough. Range in solid solution and structure of naturally occurring troilite and pyrrhotite. Am. Mineral., 49:1350–1365, 1964.

[37] Masayasu Tokonami, Katsuhisa Nishiguchi, and Nobuo Morimoto. Crystal structure of a monoclinic pyrrhotite (Fe_7S_8). Am. Mineral., 57:1066–1080, 1972.

[38] David C. Liles and Johan P.R. de Villiers. Redetermination of the structure of 5c pyrrhotite at low temperature and at room temperature. Am. Mineral., 97:257–261, 2012.

[39] Johan P.R. de Villiers, David C. Liles, and Megan Becker. The crystal structure of a naturally occurring 5c pyrrhotite from Sudbury, its chemistry, and vacancy distribution. Am. Mineral., 94:1405–1410, 2009.

[40] Johan P.R. de Villiers and David C. Liles. The crystal-structure and vacancy distribution in 6c pyrrhotite. Am. Mineral., 95:148–152, 2010.

[41] Riley Murphy and Daniel R. Strongin. Surface reactivity of pyrite and related sulfides. Surf. Sci. Rep., 64(1):1–45, January 2009.

[42] A. Ennaoui, S. Fiechter, Ch. Pettenkofer, N. Alonso-Vante, K. Büker, M. Bronold, Ch. Höpfner, and H. Tributsch. Iron disulfide for solar energy conversion. Sol. Energ. Mat. Sol. C., 29(4):289–370, May 1993.

[43] K. Buker, N. Alonso-Vante, and H. Tributsch. Photovoltaic output limitation of n-FeS$_2$ (pyrite) schottky barriers: A temperature-dependent characterization. J. Appl. Phys, 72(12):5721–5728, December 1992.

[44] A. Ennaoui, S. Fiechter, W. Jaegermann, and H. Tributsch. Photoelectrochemistry of Highly Quantum Efficient Single-Crystalline n-FeS$_2$ (Pyrite). J. Electrochem. Soc., 133(1):97–106, January 1986.

[45] M. Bronold, Y. Tomm, and W. Jaegermann. Surface states on cubic d-band semiconductor pyrite (FeS$_2$). Surf. Sci., 314(3):L931–L936, August 1994.

[46] Moritz Limpinsel, Nima Farhi, Nicholas Berry, Jeffrey Lindemuth, Craig L. Perkins, Qiyin Lin, and Matt Law. An inversion layer at the surface of n-type iron pyrite. Energy & Environmental Science, 7(6):1974, 2014.

[47] F. Hulliger and E. Mooser. Semiconductivity in pyrite, marcasite and arsenopyrite phases. Journal of Physics and Chemistry of Solids, 26(2):429–433, February 1965.

[48] John B. Goodenough. Energy bands in TX$_2$ compounds with pyrite, marcasite, and arsenopyrite structures. J. Solid State Chem., 5(1):144–152, July 1972.

[49] Ruoshi Sun, M. K. Y. Chan, ShinYoung Kang, and G. Ceder. Intrinsic stoichiometry and oxygen-induced p-type conductivity of pyrite FeS$_2$. Phys. Rev. B, 84(3):035212, July 2011.

[50] Liping Yu, Stephan Lany, Robert Kykyneshi, Vorranutch Jieratum, Ram Ravichandran, Brian Pelatt, Emmeline Altschul, Heather A. S. Platt, John F. Wager, Douglas A. Keszler, and Alex Zunger. Iron Chalcogenide Photovoltaic Absorbers. Adv Energy Mater., 1(5):748–753, August 2011.

[51] S. Fiechter. Defect formation energies and homogeneity ranges of rock salt-, pyrite-, chalcopyrite- and molybdenite-type compound semiconductors. Sol. Energy Mater Sol. Cells, 83(4):459–477, July 2004.

[52] J. M. Guevremont, D. R. Strongin, and M. A. A. Schoonen. Photoemission of Adsorbed Xenon, X-ray Photoelectron Spectroscopy, and Temperature-Programmed Desorption Studies of H$_2$O on FeS$_2$(100). Langmuir, 14(6):1361–1366, March 1998.

[53] R. Schieck, A. Hartmann, S. Fiechter, R. Knenkamp, and H. Wetzel. Electrical properties of natural and synthetic pyrite (FeS$_2$) crystals. J. Mater. Res., 5(7):1567–1572, July 1990.

[54] J. Luck, A. Hartmann, and S. Fiechter. Stoichiometry and impurity concentration in synthetically grown iron pyrite crystals and their constituents. Z. Anal. Chem., 334(5):441–446, January 1989.

[55] G. Kresse and J. Hafner. Ab initio molecular dynamics for liquid metals. Phys. Rev. B, 47(1):558–561, January 1993.

[56] G. Kresse and J. Hafner. Ab initio molecular-dynamics simulation of the liquid-metal-amorphous-semiconductor transition in germanium. Phys. Rev. B, 49(20):14251–14269, May 1994.

[57] G. Kresse and J. Furthmüller. Efficiency of ab-initio total energy calculations for metals and semiconductors using a plane-wave basis set. Comput. Mater. Sci., 6(1):15–50, July 1996.

[58] G. Kresse and J. Furthmüller. Efficient iterative schemes for ab initio total-energy calculations using a plane-wave basis set. Phys. Rev. B, 54(16):11169–11186, October 1996.

[59] Arash A. Mostofi, Jonathan R. Yates, Giovanni Pizzi, Young-Su Lee, Ivo Souza, David Vanderbilt, and Nicola Marzari. An updated version of wannier90: A tool for obtaining maximally-localised Wannier functions. Comput. Phys. Commun., 185(8):2309–2310, August 2014.

[60] P. Hohenberg and W. Kohn. Inhomogeneous Electron Gas. Phys. Rev., 136(3B):B864–B871, November 1964.

[61] Tosio Kato. On the eigenfunctions of many-particle systems in quantum mechanics. Comm. Pure Appl. Math., 10(2):151–177, 1957.

[62] W. Kohn and L. J. Sham. Self-Consistent Equations Including Exchange and Correlation Effects. Phys. Rev., 140(4A):A1133–A1138, November 1965.

[63] T Koopmans. ber die Zuordnung von Wellenfunktionen und Eigenwerten zu den Einzelnen Elektronen Eines Atoms. Physica, 1(1):104–113, January 1934.

[64] John P. Perdew, Kieron Burke, and Matthias Ernzerhof. Generalized Gradient Approximation Made Simple. Phys. Rev. Lett., 77:3865–3868, October 1996.

[65] Stefan Kurth, John P. Perdew, and Peter Blaha. Molecular and solid-state tests of density functional approximations: LSD, GGAs, and meta-GGAs. Int. J. Quantum Chem., 75(4-5):889–909, October 1999.

[66] Ruoshi Sun, M. K. Y. Chan, and G. Ceder. First-principles electronic structure and relative stability of pyrite and marcasite: Implications for photovoltaic performance. Phys. Rev. B, 83(23):235311, June 2011.

[67] Y. N. Zhang, M. Law, and R. Q. Wu. Atomistic Modeling of Sulfur Vacancy Diffusion Near Iron Pyrite Surfaces. J. Phys. Chem. C, 119(44):24859–24864, November 2015.

[68] Heather J. Kulik. Perspective: Treating electron over-delocalization with the DFT+U method. J. Chem. Phys., 142(24):240901, June 2015.

[69] Jochen Autschbach and Monika Srebro. Delocalization Error and Functional Tuning in Kohn-Sham Calculations of Molecular Properties. Acc. Chem. Res., 47(8):2592–2602, August 2014.

[70] Paula Mori-Snchez, Aron J. Cohen, and Weitao Yang. Localization and Delocalization Errors in Density Functional Theory and Implications for Band-Gap Prediction. Phys. Rev. Lett., 100(14):146401, April 2008.

[71] Steven H. Simon. The Oxford Solid State Basics. Oxford University Press, New York, NY, 1 edition, 2013.

[72] S. L. Dudarev, G. A. Botton, S. Y. Savrasov, C. J. Humphreys, and A. P. Sutton. Electron-energy-loss spectra and the structural stability of nickel oxide: An LSDA+U study. Phys. Rev. B, 57(3):1505–1509, January 1998.

[73] J. M. Ziman. Principles of the Theory of Solids. Cambridge University Press, University Printing House, Cambridge, 2 edition, 1972.

[74] P. E. Blchl. Projector augmented-wave method. Phys. Rev. B, 50(24):17953–17979, December 1994.

[75] G. Kresse and D. Joubert. From ultrasoft pseudopotentials to the projector augmented-wave method. Phys. Rev. B, 59(3):1758–1775, January 1999.

[76] D. Hobbs and J. Hafner. Magnetism and magneto-structural effects in transition-metal sulphides. J. Phys.: Condens. Matter, 11(42):8197–8222, 1999.

[77] P. Raybaud, J. Hafner, G. Kresse, and H. Toulhoat. Ab initio density functional studies of transition-metal sulphides: II. Electronic structure. J. Phys.: Condens. Matter, 9(50):11107, 1997.

[78] Y. N. Zhang, J. Hu, M. Law, and R. Q. Wu. Effect of surface stoichiometry on the band gap of the pyrite FeS_2(100) surface. Phys. Rev. B, 85(8):085314, February 2012.

[79] Arne F. Andresen. Magnetic Phase Transitions in Stoichiometric FeS Studied by Means of Neutron Diffraction. Acta Chem. Scand., 14:919–926, 1960.

[80] Anton Kokalj. Computer graphics and graphical user interfaces as tools in simulations of matter at the atomic scale. Comput. Mater. Sci., 28(2):155–168, October 2003.

[81] L. Craco and J. L. B. Faria. Electronic localization and bad-metallicity in pure and electron-doped troilite: A local-density-approximation plus dynamical-mean-field-theory study of FeS for lithium-ion batteries. J. Appl. Phys., 119(8):085107, February 2016.

[82] A. V. Ushakov, A. O. Shorikov, V. I. Anisimov, N. V. Baranov, and S. V. Streltsov. Suppression of magnetism under pressure in FeS: A DFT+DMFT study. Phys. Rev. B, 95(20):205116, May 2017.

[83] Sajeev John, Costas Soukoulis, Morrel H. Cohen, and E. N. Economou. Theory of Electron Band Tails and the Urbach Optical-Absorption Edge. Phys. Rev. Lett., 57(14):1777–1780, October 1986.

[84] Franz Urbach. The Long-Wavelength Edge of Photographic Sensitivity and of the Electronic Absorption of Solids. Phys. Rev., 92(5):1324, December 1953.

[85] R. A. de Groot, F. M. Mueller, P. G. van Engen, and K. H. J. Buschow. New Class of Materials: Half-Metallic Ferromagnets. Phys. Rev. Lett., 50(25):2024–2027, June 1983.

[86] K. Schwarz. CrO_2 predicted as a half-metallic ferromagnet. J. Phys. F: Met. Phys., 16(9):L211–L215, 1986.

[87] C. M. Fang, G. A. de Wijs, and R. A. de Groot. Spin-polarization in half-metals (invited). J. Appl. Phys., 91(10):8340–8344, 2002.

[88] X. L. Wang. Proposal for a New Class of Materials: Spin Gapless Semiconductors. Phys. Rev. Lett., 100(15):156404, April 2008.

[89] Stefano Baroni, Stefano de Gironcoli, Andrea Dal Corso, and Paolo Giannozzi. Phonons and related crystal properties from density-functional perturbation theory. Rev. Mod. Phys., 73(2):515–562, July 2001.

[90] Atsushi Togo and Isao Tanaka. First principles phonon calculations in materials science. Scripta Mater., 108:1–5, November 2015.

[91] E. Kroumova, M. I. Aroyo, J. M. Perez-Mato, A. Kirov, C. Capillas, S. Ivantchev, and H. Wondratschek. Bilbao Crystallographic Server : Useful Databases and Tools for Phase-Transition Studies. Phase Transitions, 76(1-2):155–170, January 2003.

[92] Tams Rozgonyi and Andrs Stirling. DFT Study of Oxidation States on Pyrite Surface Sites. J. Phys. Chem. C, 119(14):7704–7710, April 2015.

[93] F. W. Herbert, A. Krishnamoorthy, K. J. Van Vliet, and B. Yildiz. Quantification of electronic band gap and surface states on $FeS_2(100)$. Surf. Sci., 618:53–61, December 2013.

[94] Miguel Cabn-Acevedo, Nicholas S. Kaiser, Caroline R. English, Dong Liang, Blaise J. Thompson, Hong-En Chen, Kyle J. Czech, John C. Wright, Robert J. Hamers, and Song Jin. Ionization of High-Density Deep Donor Defect States Explains the Low Photovoltage of Iron Pyrite Single Crystals. J. Am. Chem. Soc., 136(49):17163–17179, December 2014.

[95] Peter Bayliss. Crystal structure refinement of a weakly anisotropic pyrite. Am. Mineral., 62:1168–1172, 1977.

[96] I. N. Yakovkin and N. V. Petrova. Influence of the thickness and surface composition on the electronic structure of FeS_2 layers. Appl. Surf. Sci., 377:184–190, July 2016.

[97] P. Lazi, R. Armiento, F. W. Herbert, R. Chakraborty, R. Sun, M. K. Y. Chan, K. Hartman, T. Buonassisi, B. Yildiz, and G. Ceder. Low intensity conduction states in FeS_2: implications for absorption, open-circuit voltage and surface recombination. J. Phys.: Condens. Matter, 25(46):465801, November 2013.

[98] G. U. von Oertzen, R. T. Jones, and A. R. Gerson. Electronic and optical properties of Fe, Zn and Pb sulfides. Phys. Chem. Miner., 32(4):255–268, July 2005.

[99] Syhei Miyahara and Teruo Teranishi. Magnetic Properties of FeS_2 and CoS_2. J. Appl. Phys., 39(2):896–897, February 1968.

[100] Ernest H. Nickel. Structural stability of minerals with the pyrite, marcasite, arsenopyrite and lollingite structures. Can. Mineral., 9(3):311–321, June 1968.

[101] Hendrik J. Monkhorst and James D. Pack. Special points for Brillouin-zone integrations. Phys. Rev. B, 13(12):5188–5192, June 1976.

[102] Peter E. Blöchl, O. Jepsen, and O. K. Andersen. Improved tetrahedron method for Brillouin-zone integrations. Phys. Rev. B, 49(23):16223–16233, June 1994.

[103] Jun Hu, Yanning Zhang, Matt Law, and Ruqian Wu. Increasing the Band Gap of Iron Pyrite by Alloying with Oxygen. J. Am. Chem. Soc., 134(32):13216–13219, August 2012.

[104] Dipendra Banjara, Yuriy Malozovsky, LaShounda Franklin, and Diola Bagayoko. First-principles studies of electronic, transport and bulk properties of pyrite FeS_2. AIP Advances, 8(2):025212, February 2018.

[105] S. G. Choi, J. Hu, L. S. Abdallah, M. Limpinsel, Y. N. Zhang, S. Zollner, R. Q. Wu, and M. Law. Pseudodielectric function and critical-point energies of iron pyrite. Phys. Rev. B, 86(11):115207, September 2012.

[106] Brian Kolb and Alexie M. Kolpak. Ultrafast band-gap oscillations in iron pyrite. Phys. Rev. B, 88(23):235208, December 2013.

[107] S. Lauer, A. X. Trautwein, and F. E. Harris. Electronic-structure calculations, photoelectron spectra, optical spectra, and mössbauer parameters for the pyrites MS_2 (M = Fe, Co, Ni, Cu, Zn). Phys. Rev. B, 29(12):6774–6783, June 1984.

[108] V. N. Antonov, L. P. Germash, A. P. Shpak, and A. N. Yaresko. Electronic structure, optical and X-ray emission spectra in FeS_2. Phys. Status Solidi B, 246(2):411–416, 2009.

[109] L. Vadkhiya and B. L. Ahuja. Electronic and optical properties of iron pyrite. J. Alloys Compd., 509(6):3042–3047, February 2011.

[110] A. Schlegel and P. Wachter. Optical properties, phonons and electronic structure of iron pyrite (FeS_2). J. Phys. C: Solid State Phys., 9(17):3363, September 1976.

[111] A. Scaramucci, J. Ammann, N. A. Spaldin, and C. Ederer. Separating different contributions to the crystal-field parameters using Wannier functions. J. Phys.: Condens. Matter, 27(17):175503, 2015.